
Doctoral Dissertations


Student Theses and Dissertations

Fall 2019

Development and characterization of nanostructured steels and high entropy alloys for nuclear applications

Andrew Kalevi Hoffman

Follow this and additional works at: https://scholarsmine.mst.edu/doctoral_dissertations

 Part of the [Materials Science and Engineering Commons](#), and the [Nuclear Engineering Commons](#)
Department: Mining and Nuclear Engineering

Recommended Citation

Hoffman, Andrew Kalevi, "Development and characterization of nanostructured steels and high entropy alloys for nuclear applications" (2019). *Doctoral Dissertations*. 2833.
https://scholarsmine.mst.edu/doctoral_dissertations/2833

This thesis is brought to you by Scholars' Mine, a service of the Missouri S&T Library and Learning Resources. This work is protected by U. S. Copyright Law. Unauthorized use including reproduction for redistribution requires the permission of the copyright holder. For more information, please contact scholarsmine@mst.edu.

DEVELOPMENT AND CHARACTERIZATION OF NANOSTRUCTURED STEELS
AND HIGH ENTROPY ALLOYS FOR NUCLEAR APPLICATIONS

by

ANDREW KALEVI HOFFMAN

A DISSERTATION

Presented to the Faculty of the Graduate School of the
MISSOURI UNIVERSITY OF SCIENCE AND TECHNOLOGY

In Partial Fulfillment of the Requirements for the Degree

DOCTOR OF PHILOSOPHY

in

NUCLEAR ENGINEERING

2019

Approved by:

Dr. Haiming Wen, Advisor

Dr. Ayodeji Alajo

Dr. Joseph Graham

Dr. Carlos Castano

Dr. Ronald O'Malley

© 2019

ANDREW KALEVI HOFFMAN

All Rights Reserved

PUBLICATION DISSERTATION OPTION

This dissertation consists of the following four articles, formatted in the style used by the Missouri University of Science and Technology:

Paper I: Pages 14-23 were published in Materials Letters on 15 May 2019.

Paper II: Pages 24-40 have been submitted to Scripta Materialia.

Paper III: Pages 41-68 are intended for submission to Acta Materialia.

Paper IV: Pages 69-90 have been accepted to JOM on 11 October 2019.

ABSTRACT

Nuclear reactor materials are subjected to a harsh environment including high temperatures and radiation fluences. In order to extend the lifetime of current light water reactors (LWRs) and realize the development of advanced Gen IV nuclear reactors new materials must be developed which can withstand such an environment. This thesis involves two approaches to solving this materials problem: advanced manufacturing of current commercial alloys using severe plastic deformation (SPD) and the development of new advanced high entropy alloys (HEAs).

Because SPD is effective at achieving grain refinement, this technique was used to obtain material having a high volume fraction of grain boundaries which act as effective radiation induced defect sinks. This work aims to study the pre-irradiation microstructure and irradiation tolerance of nanostructured 304 produced using SPD.

HEAs have been theorized to have retarded diffusion which prevents large voids and dislocation loops from forming in addition to their good phase stability. Most HEA compositions, however, contain Co which activates under irradiation and can cause concerns over waste management. This work studies two compositions of Co-free HEAs and evaluates their performance under ion irradiation.

ACKNOWLEDGMENTS

This research was financially supported by the U.S. Department of Energy, Office of Nuclear Energy through the NEET-NSUF (Nuclear Energy Enabling Technology - Nuclear Science User Facility) program (award number DE-NE0008524), and through the NSUF-RTE program (award number 17-865).

First and foremost, I am deeply appreciative to my PhD advisor Dr. Haiming Wen. He has given me the advice, encouragement, opportunities, funding, and tools that most graduate students could never dream of. Because of him I am the researcher I am today. Thank to Dr. Ayodeji Alajo, Dr. Joseph Graham, Dr. Carlos Castano, and Dr. Ronald O'Malley for serving as members on my committee. I am grateful to Dr. Y. Wu who trained and taught me on both transmission electron microscopy and atom probe tomography. Thanks to other staff Dr. J. Burns, Dr. C. Weisner, Dr. W. Chen, Dr. M. Buchely and Dr. E. Bohannon. I am also deeply grateful for my previous research advisors Dr. Khalid Chouffani, and Dr. Lawrence Rees for preparing me to excel in my PhD work. Thank you to all my associates, especially: M. Arivu, Dr. J. Duan, H. Pommerenke, M. Luebbe, V. Athavale, I. Robin, R. Carnahan, and M. Wilding. I also would like to thank our collaborators at Idaho National Laboratory and the University of Wisconsin-Madison Dr. L. He, Dr. X. Liu, Dr. Y. Zhang, Dr. L. He, and Dr. K. Sridharan. I am forever thankful to my parents for their emotional and financial support throughout my studies. To all those who ever mentored, taught, or inspired me: though your names can't all fit on paper in this work, I am forever thankful.

TABLE OF CONTENTS

	Page
PUBLICATION DISSERTATION OPTION	iii
ABSTRACT	iv
ACKNOWLEDGMENTS	v
LIST OF ILLUSTRATIONS	ix
LIST OF TABLES	xiii
NOMENCLATURE	xiv
 SECTION	
1. INTRODUCTION	1
1.1. RADIATION DAMAGE IN NUCLEAR STRUCTURAL MATERIALS	1
1.2. MOTIVATION/ADVANCED MATERIALS FOR NUCLEAR APPLICATIONS	7
1.3. MANUFACTURING NANOSTRUCTURED STEELS THROUGH SEVERE PLASTIC DEFORMATION	11
 PAPER	
■ HIGH-PRESSURE TORSION ASSISTED SEGREGATION AND PRECIPITATION IN A FE-18CR-8NI AUSTENITIC STAINLESS STEEL	14
ABSTRACT	14
1. INTRODUCTION	15
2. EXPERIMENTAL	16
3. RESULTS AND DISCUSSION	16
4. CONCLUSIONS	18

ACKNOWLEDGEMENTS	19
REFERENCES	22
■ ENHANCED RESISTANCE TO IRRADIATION-INDUCED SEGREGATION AND PRECIPITATION IN A NANOCRYSTALLINE FE-18CR-8NI STEEL	24
ABSTRACT	24
REFERENCES	38
■ ENHANCING RESISTANCE TO IRRADIATION INDUCED FERRITIC TRANSFORMATION THROUGH NANO-STRUCTURING OF AUSTENITIC STEELS	41
ABSTRACT	41
1. INTRODUCTION	42
2. EXPERIMENTAL	44
3. RESULTS	45
3.1. EFFECT OF GRAIN SIZE ON IRRADIATION INDUCED PHASE CHANGE	45
3.2. CHEMICAL SEGREGATION BEHAVIOR	46
3.3. IRRADIATION INDUCED DEFECT STRUCTURES	47
3.4. RADIATION INDUCED SEGREGATION	49
4. MODELING AND DISCUSSION	50
4.1. THERMAL EFFECTS OF PHASE TRANSFORMATION	50
4.2. $\gamma \rightarrow \alpha$ TRANSFORMATION MECHANISM	51
4.3. GRAIN SIZE EFFECTS ON DEFORMATION INDUCED TRANSFORMATION	53
4.4. GRAIN SIZE EFFECTS ON RADIATION INDUCED SEGREGATION AND PRECIPITATION	55

5. CONCLUSIONS	56
ACKNOWLEDGMENTS	57
REFERENCES	63
■ EFFECTS OF AL AND TI ADDITIONS ON THE IRRADIATION BEHAVIOR OF AN FE-MN-NI-CR MULTI-PRINCIPLE ELEMENT ALLOY	69
ABSTRACT	69
1. INTRODUCTION	70
2. EXPERIMENTAL	72
3. RESULTS AND DISCUSSION	74
4. CONCLUSIONS	80
ACKNOWLEDGEMENTS	81
REFERENCES	88
SECTION	
2. CONCLUSIONS AND FUTURE WORK	91
2.1. CONCLUSIONS	91
2.2. FUTURE WORK	92
BIBLIOGRAPHY	94
VITA	98

LIST OF ILLUSTRATIONS

SECTION	Page
Figure 1.1. Depiction of neutron radiation damage mechanism [1].	1
Figure 1.2. Images of dislocation loops in irradiation 300 series stainless steel [2].	2
Figure 1.3. Image of voids formed in neutron irradiated 304 stainless steel [4].	3
Figure 1.4. Schematic of mechanisms responsible for radiation induced segregation [5].	4
Figure 1.5. Atom maps showing Ni-Si cluster formation in irradiated high purity 304 [9].	5
Figure 1.6. Schematic of contributing mechanism to intergranular stress corrosion cracking in 304 steel used in the reactor environments [15].	6
Figure 1.7. Schematic of a pressurized water reactor showing the various materials used [3].	7
Figure 1.8. Stress strain curves comparing neutron irradiated coarse grained and ultrafine grained ferritic steel. The ultrafine grained steel shows increased resistance to radiation induced embrittlement [19].	8
Figure 1.9. In-situ images of a radiation induced defect cluster being absorbed by and annihilating at a grain boundary in nanocrystalline Ni [18].	9
Figure 1.10. Images of voids in increasingly complex Ni alloys, showing the most complex high entropy alloy to have the greatest resistance to irradiation induced void swelling [25].	10
Figure 1.11. Schematic of a) high pressure torsion and b) equal channel angular pressing [40].	13

PAPER I

Figure 1. a) TEM bright-field image showing general microstructure of SS304 after HPT with inset selected-area electron diffraction pattern showing pure austenitic structure; b) XRD patterns of SS304 before HPT [coarse-grained (CG)] as well as after HPT at several different temperatures. After HPT at 200 and 300 °C, no body-centered cubic (BCC) or body-centered tetragonal (BCT) phase is present.20

Figure 2. a) APT reconstruction with Ni atoms displayed and isoconcentration surfaces of 11 at.% Ni and 0.9 at.% Cu superimposed. b) proximity histogram concentration profile of the middle Ni-Si-Mn enriched precipitate in a); c) proximity histogram concentration profile showing Cu concentration of the Cu-rich nanoprecipitate indicated in a).....21

Figure 3 a) and b) 1-D concentration profiles of grain boundaries in figure 2a. c) APT reconstruction showing P (red) and Si atoms (blue), a grain boundary and a cylinder region of interest across it; d) 1-D concentration profile across the grain boundary indicated in c) showing segregation of Si and P along the grain boundary.....22

PAPER II

Figure 1. a) APT reconstruction of HPT304 showing Ni atoms (blue) and Ni segregation along one GB, b) 1-D profile across ROI shown in a) indicating Ni enrichment but no Cr depletion after HPT, c) APT reconstruction of HPT304 annealed at 500°C for 24 hours showing Ti atoms (blue); several GBs can be seen, d) and e) 1-D concentration profiles across the ROI shown in c) indicating Cr enrichment but no Ni depletion. Mo, Si, Ti, and C were all also enriched at the GB.35

Figure 2. APT reconstruction of irradiated HPT304 showing Si atoms (grey) and 4 at.% Si isosurface to highlight grain boundaries; mostly only one UFG was observed; b) and c) 1-D concentration profiles across the ROI are in a) showing typical RIS behavior with enrichment in Ni, Si, Ti, and Co and depletion in Fe, Cr, and Mo; d) Another APT reconstruction of irradiated HPT304 showing Si atoms (grey) and 2 at.% Si isosurface to highlight grain boundaries; primarily, only NC grains were observed; e) and f) 1-D concentration profiles across the ROI shown in d); RIS was reduced in the NC grains, as compared to those in the UFG.36

Figure 3. a), b), and c) APT reconstructions of irradiated HPT304 showing Si atoms (grey) and 5 at.% Cu isosurfaces (green) showing precipitation of Cu clusters. UFG in a) shows significant intragranular Cu precipitation while NC grains in b) and c) show little to no Cu precipitation. d) Proxigram based on all 5 at.% Cu isosurfaces in a). e) Proxigram based on all 5 at.% Cu isosurfaces in the boxed region of c).	37
Figure 4. a) APT reconstruction of irradiated HPT 304 with Si atoms (grey) and 4 at.% Si isosurfaces to highlight GBs; b) and c) 1-D concentration profiles across ROI, in a) showing enrichment of Cr and Mo and no enrichment of Co.	38
 PAPER III 	
Figure 1. a-c) Low angle XRD and gonio scans showing the ion irradiated thin film region and non-irradiated bulk of the CG, ECAP, and HPT 304. A significant amount of α -ferrite is seen after irradiation in all samples as seen from the α -110 reflection. d) XRD of CG, ECAP, and HPT 304 after annealing at 500 °C for 24 hrs.	58
Figure 2. PED misorientation maps (left) and phase maps (right) showing γ -austenite (red) and α -ferrite (green) for a) HPT, b) ECAP, and c) CG 304 ion irradiated at 500 °C.	59
Figure 3. a) EBSD phase map showing austenite (blue) and ferrite (red). EDS chemical maps of the map in a) are shown for b) Cr and c) Ni. Not all ferritic regions are depleted in Ni and enriched in Cr.....	60
Figure 4. a) STEM BF and b)-d) associated EDS chemical maps of ion irradiated CG 304 showing Ni-Si enriched, Cu, and Cr enriched $M_{23}C_6$ precipitates.....	61
Figure 5. Micrographs of different grain sized 304 after ion irradiation. a) TEM BF of CG 304 showing large faulted loops. b) STEM BF of ECAP 304 showing many small faulted loops. c) STEM BF of HPT 304 showing many “black spot” defects indicating formation of defect clusters.	62
Figure 6. a) TEM DF and d) TEM BF of irradiated CG 304 showing the formation of large dislocation networks. b) TEM BF of irradiated and e) unirradiated ECAP 304 showing dislocation cells/tangles and little change in dislocation structures after irradiation. c) STEM DF of irradiated HPT 304 showing irradiation induced grain growth, but many defect free grains. f) TEM BF of HPT 304 annealed at 500 °C for 24 hrs showing no grain growth, and limited recovery.	62

Figure 7. Phase fraction vs temperature of 304 steel composition in this study.....63

PAPER IV

Figure 1. 3.7 MeV Fe²⁺ induced damage and implantation profiles in Fe₃₀Ni₃₀Mn₃₀Cr₁₀. *Ed* is atom displacement energy.82

Figure 2. a) SEM secondary electron image and b)-g) corresponding EDS maps of (Fe₃₀Ni₃₀Mn₃₀Cr₁₀)₉₄Ti₂Al₄ after cold rolling and annealing, showing the Ni, Ti, and Al enriched γ' phase. h) TEM bright field of γ' precipitates.83

Figure 3. a) TEM bright field and b) selected area electron diffraction (SAED) pattern showing the structure of γ' phase in the (Fe₃₀Ni₃₀Mn₃₀Cr₁₀)₉₄Ti₂Al₄ HEA to be L1₂ (ordered FCC).83

Figure 4. TEM results of Fe₃₀Ni₃₀Mn₃₀Cr₁₀ ion irradiated up to 120 dpa. a) and b) bright field of dislocation loops in the 300 °C irradiated sample. c) bright field and d) rel-rod image with SAED pattern (inset) of the 500 °C irradiated sample.84

Figure 5. TEM results of (Fe₃₀Ni₃₀Mn₃₀Cr₁₀)₉₄Ti₂Al₄ ion irradiated up to 120 dpa. a) bright field and b) rel-rod image with SAED pattern (inset) of the 300 °C irradiated sample. Beam conditions for a) and b) were $g=222$ with a 112 zone axis. c) bright field and d) rel-rod image with SAED pattern (inset) of the 500 °C irradiated sample.85

Figure 6. Loop size distribution for Fe₃₀Ni₃₀Mn₃₀Cr₁₀ ion irradiated at a) 300 °C and b) 500 °C and (Fe₃₀Ni₃₀Mn₃₀Cr₁₀)₉₄Ti₂Al₄ ion irradiated at c) 300 °C and d) 500 °C.86

Figure 7. STEM bright field image of a faulted dislocation loop and associated EDS point scans showing an enrichment of Ti.87

Figure 8. STEM dark-field image of 300 °C irradiated (Fe₃₀Ni₃₀Mn₃₀Cr₁₀)₉₄Ti₂Al₄ (left) and TEM bright-field image of 500 °C irradiated (Fe₃₀Ni₃₀Mn₃₀Cr₁₀)₉₄Ti₂Al₄ (right) showing the morphology of γ' precipitates in the irradiated and unirradiated regions.88

LIST OF TABLES

	Page
PAPER I	
Table 1. Elemental composition of SS304.....	19
PAPER II	
Table 1. Bulk composition of SS304	34
Table 2. Summary of grain boundary segregation in annealed and irradiated HPT304.....	34
PAPER IV	
Table 1. Composition of matrix and γ' precipitates in $(\text{Fe}_{30}\text{Ni}_{30}\text{Mn}_{30}\text{Cr}_{10})_{94}\text{Ti}_2\text{Al}_4$ MPEA.....	81
Table 2. Summary of dislocation loop size and number density in $\text{Fe}_{30}\text{Ni}_{30}\text{Mn}_{30}\text{Cr}_{10}$ and $(\text{Fe}_{30}\text{Ni}_{30}\text{Mn}_{30}\text{Cr}_{10})_{94}\text{Ti}_2\text{Al}_4$ MPEAs ion irradiated nominally to 100 dpa.....	82
Table 3. Summary of irradiation induced hardening from nanoindentation.....	82

NOMENCLATURE

Symbol	Description
PKA	Primary Knock-on Atom
RIS	Radiation Induced Segregation
IKE	Inverse-Kirkendall Effect
SCC	Stress Corrosion Cracking
HEA	High Entropy Alloy
SPS	Spark Plasma Sintering
HIP	Hot Isostatic Pressing
CG	Coarse Grained
SPD	Sever Plastic Deformation
ECAP	Equal Channel Angular Pressing
HPT	High Pressure Torsion
PKA	Primary Knock-on Atom

1. INTRODUCTION

1.1. RADIATION DAMAGE IN NUCLEAR STRUCTURAL MATERIALS

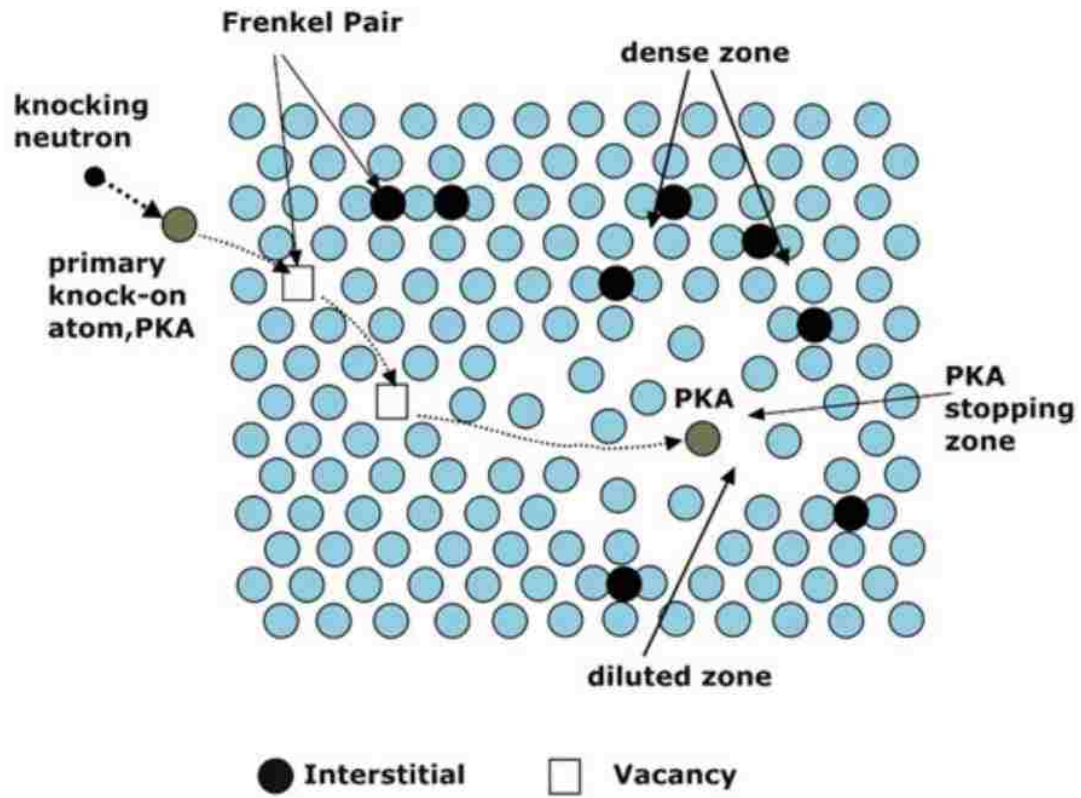


Figure 1.1. Depiction of neutron radiation damage mechanism [1].

One of the difficult aspects of materials design in a reactor environment comes from damage caused by neutron irradiation. This damage occurs from the interaction of energetic neutrons with atoms within the lattice as shown in Figure 1.1. As a neutron collides with an atom, it transfers its kinetic energy creating what is known as a primary knock-on atom (PKA). The neutron will continue to collide with atoms creating there

PKAs until it has lost energy such that it can no longer displace an atom from the lattice. The PKA will carry energy with it and also collide with surrounding atoms displacing them from the lattice. This cascade of collisions will form many point defects in the form of vacancies in the original lattice positions of displaced atoms and interstitials formed by the displaced atoms. While many of these interstitials and vacancies will recombine, many of these defects will remain and accumulate [1].

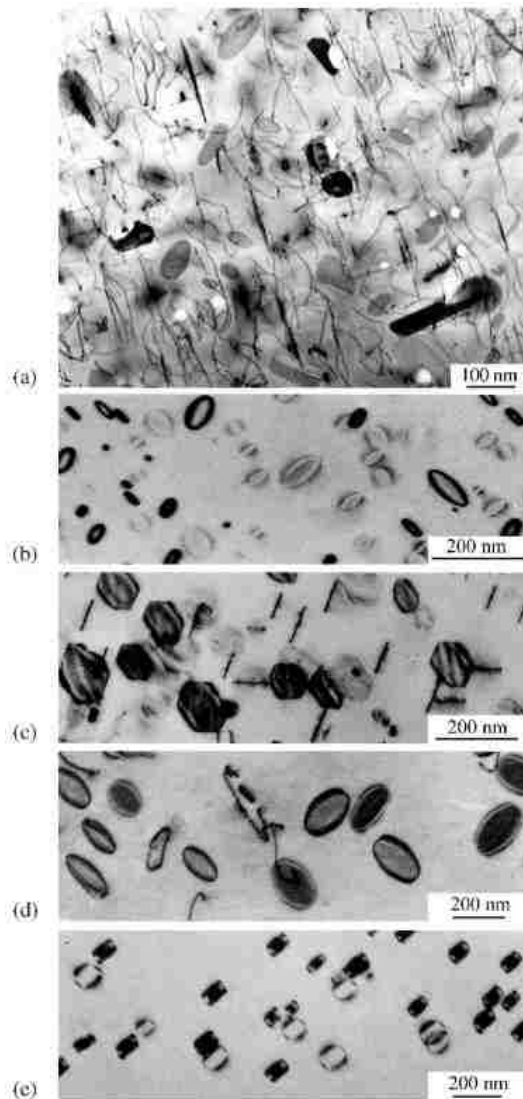


Figure 1.2. Images of dislocation loops in irradiation 300 series stainless steel [2].

These radiation induced defects can accumulate over time and create larger defect structures. Interstitials and vacancies will initially form defect clusters which are often referred to as “black-spot” defects due to their appearance in electron microscope images. Eventually larger dislocation loops will be formed as can be seen in Figure 1.2. These loops can then prevent other dislocations from moving freely throughout matrix. As dislocation movement is the mechanism for plastic deformation, this dislocation pinning from irradiation induced dislocation loops will reduce ductility of the material and is partially responsible for irradiation induced embrittlement [2,3].

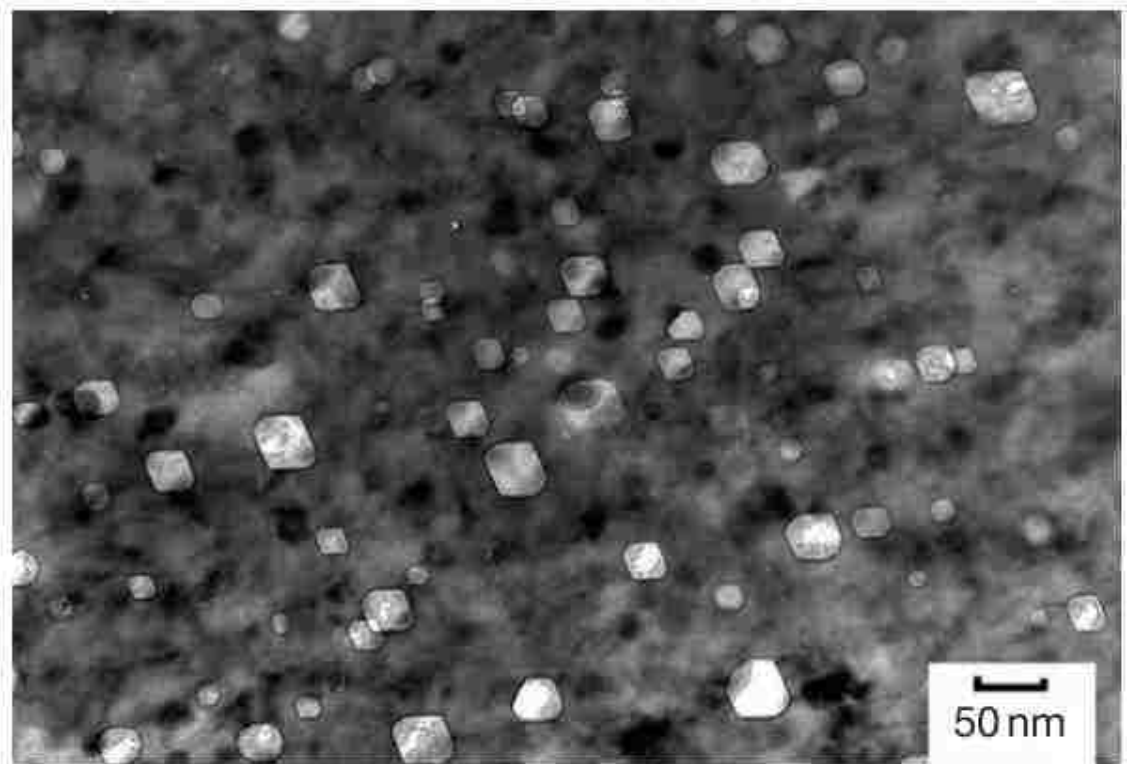


Figure 1.3. Image of voids formed in neutron irradiated 304 stainless steel [4].

Vacancy combination over time will also create larger voids within the materials. These voids will contribute to embrittlement, but also cause significant swelling within the material. This issue is exacerbated when elements which transmute and release alpha particles after neutron absorption. These alpha particles will remain as He gas within the material, and travel towards voids and grain boundaries. As the pressure from these He gas atoms builds, it stabilizes voids and the material will develop gas bubbles. These bubbles can often be formed along grain boundaries and will increase the chance of intergranular failure[2]. Gas bubbles are of concern in materials with high Ni content as Ni will transmute when neutron irradiated. Because austenitic stainless steels are alloyed with Cr and Ni, they and Ni superalloys are particularly susceptible to He gas bubble swelling and embrittlement [4].

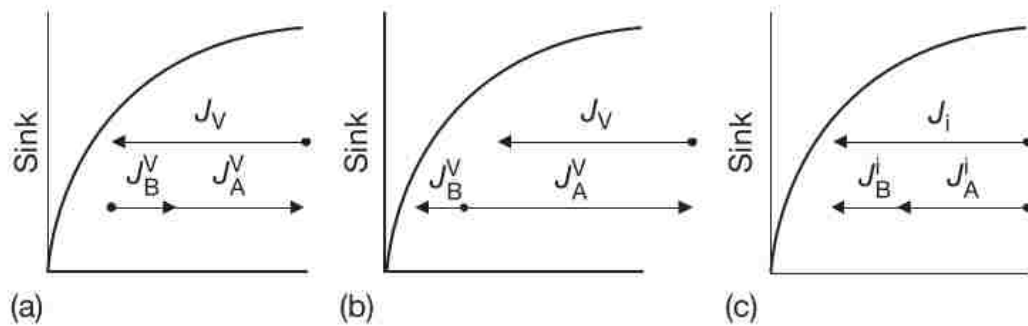


Figure 1.4. Schematic of mechanisms responsible for radiation induced segregation [5].

These defects can also contribute to other effects within the material. Radiation induced segregation (RIS) is caused by a phenomenon known as the inverse-Kirkendall effect (IKE). This unique, kinetically driven segregation is caused by the matrix being supersaturated with irradiation induced vacancies and interstitials. Figure 1.4 shows the

three mechanisms by which this segregation occurs. The mechanism which is thought to be primarily responsible for RIS is depicted in Figure 1.4a. As vacancies travel towards defect sinks (such as grain boundaries or dislocations), atoms will diffuse against this vacancy flux as they will “trade places” within the matrix. A fast diffusing atom will therefore travel faster away from sinks, leaving the slow diffusing atoms behind. This will cause depletion of fast diffusing atoms and enrichment of slow diffusing atoms at defect sinks. The other mechanisms are solute drag (shown in Figure 1.4b) and interstitial diffusion (shown in Figure 1.4c). Solute drag occurs when vacancies will “drag” atoms (usually oversized) with them towards defect sinks. Interstitial diffusion will cause an enrichment of fast diffusing interstitial atoms at defect sinks and depletion of slow diffusing interstitial atoms [5–7]. Particularly in austenitic steels, Ni and Si tend to enrich and Cr will deplete at grain boundaries [8].

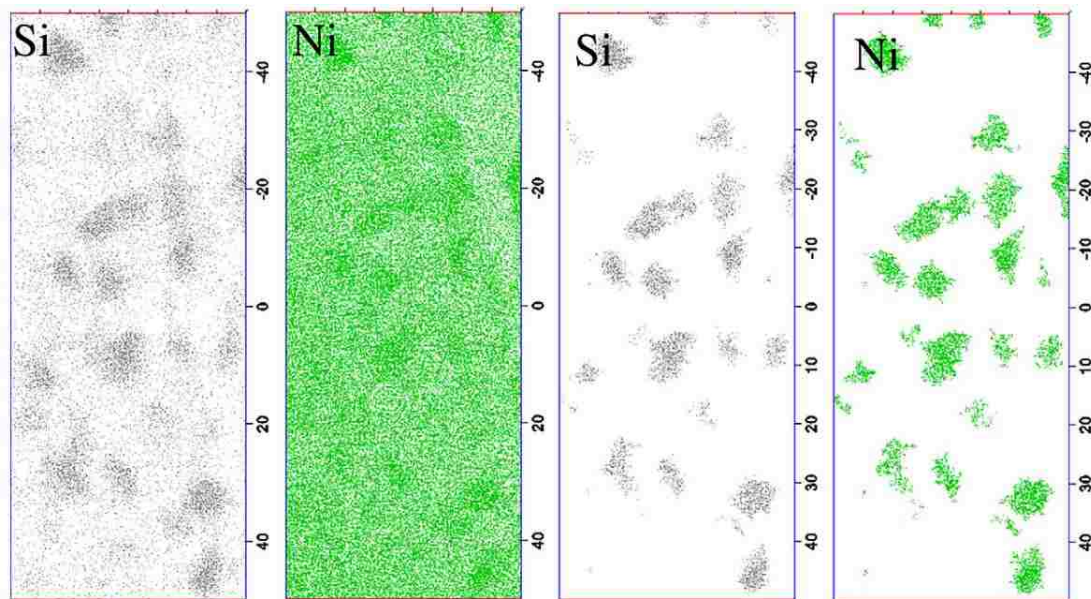


Figure 1.5. Atom maps showing Ni-Si cluster formation in irradiated high purity 304 [9].

This RIS can also contribute to phase instabilities within the material. Because RIS is a kinetically and not thermodynamically driven phenomenon, there can be many secondary phases which nucleate under only irradiation conditions. Austenitic steels, for example, will often form Ni enriched silicide phases such as the Ni-Ti-Si G-phase of Ni_3Si γ' [9–12]. This can lead to depletion of Ni, and cause instability of the austenite phase [13]. Precipitation can also cause embrittlement as well. For example, pressure vessels often have issues with embrittlement from Cu precipitation [14].

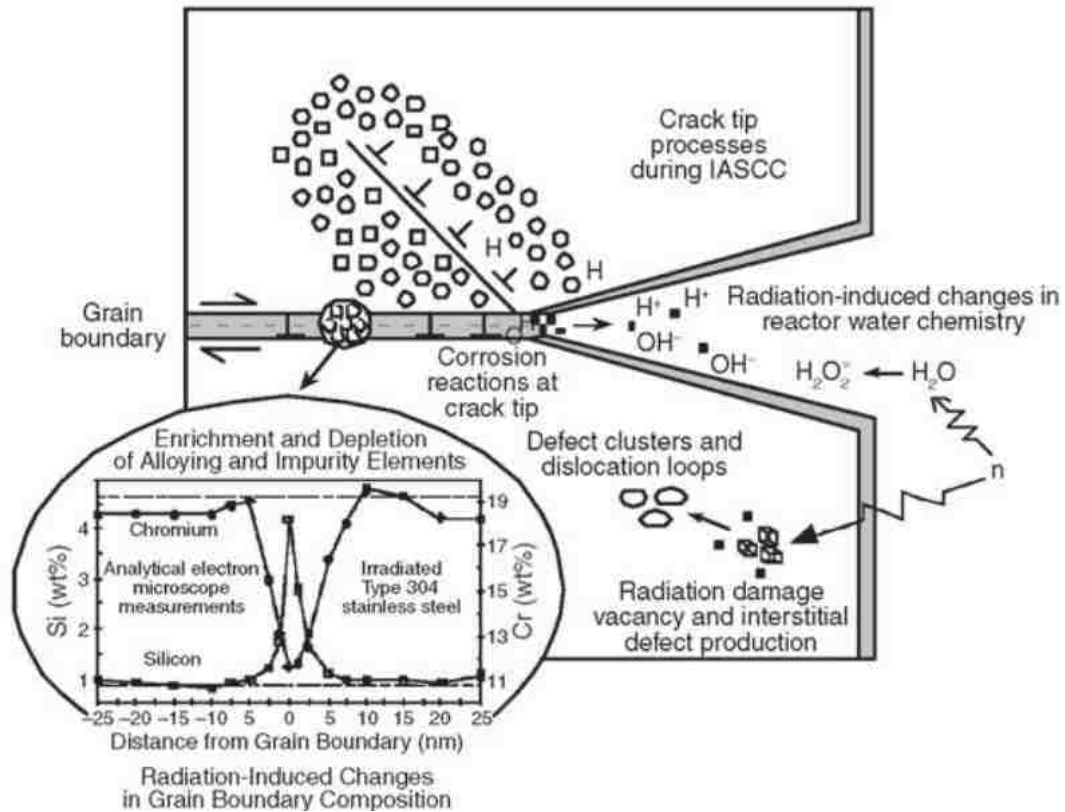


Figure 1.6. Schematic of contributing mechanism to intergranular stress corrosion cracking in 304 steel used in the reactor environments [15].

Irradiation will also contribute significantly to stress corrosion cracking (SCC) of irradiated steels. This is a compound effect which has many factors which contribute to it. Radiation induced embrittlement will cause the material to form cracks more easily. Radiation induced segregation will deplete Cr from grain boundaries which will allow for intergranular corrosion. He gas bubbles along grain boundaries can assist with intergranular failure when small intergranular cracks form [15].

1.2. MOTIVATION/ADVANCED MATERIALS FOR NUCLEAR APPLICATIONS

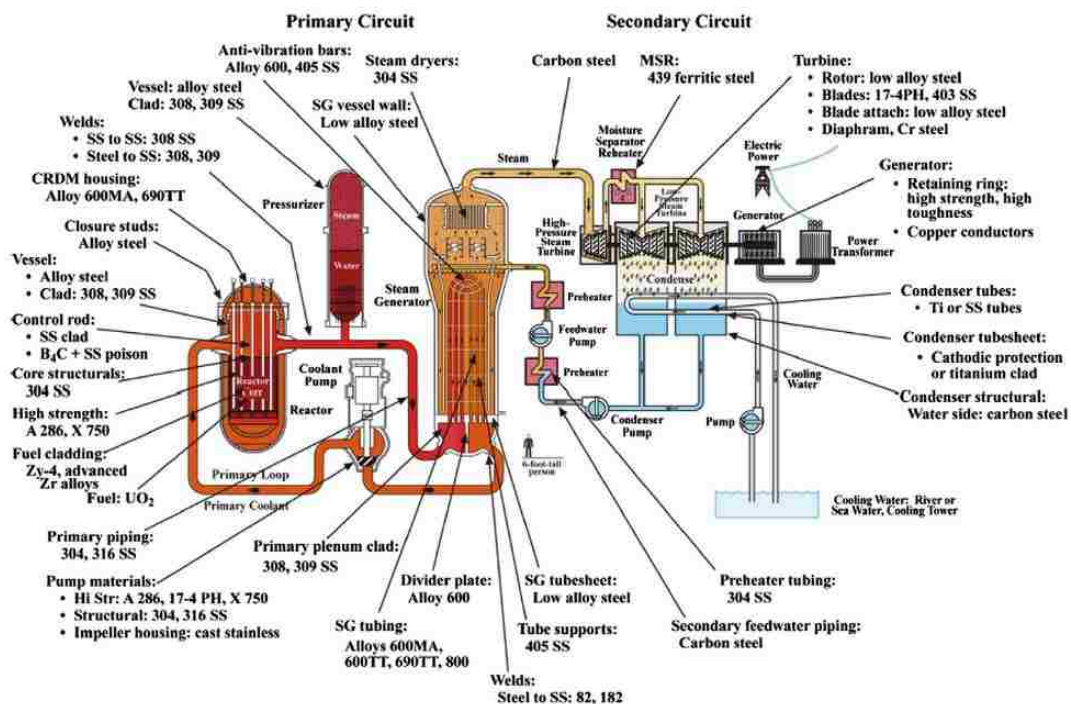


Figure 1.7. Schematic of a pressurized water reactor showing the various materials used [3].

In a nuclear reactor environment, materials are subject to high temperatures, radiation fluences, and coolants which are often corrosive. Currently, many of the

structural materials used in reactors are Ni super alloys or austenitic steels primarily due to their corrosion resistance at high temperatures [3]. Austenitic steels are also candidates for fuel cladding in sodium cooled fast reactors. These steels and Ni superalloys still suffer from the effects of radiation, and new materials need to be developed in order to extend the lifetime of light water reactor components as well as realize the development of advanced reactors in which the neutron fluences and energies are much higher than current light water reactors [16,17].

There are two approaches to developing new radiation resistant materials: advanced manufacturing of current commercial alloys and the creation of advanced alloys. This thesis explores research on both approaches through evaluating nanostructuring of current commercial steels using severe plastic deformation and the development of radiation resistant high entropy alloys (HEAs).

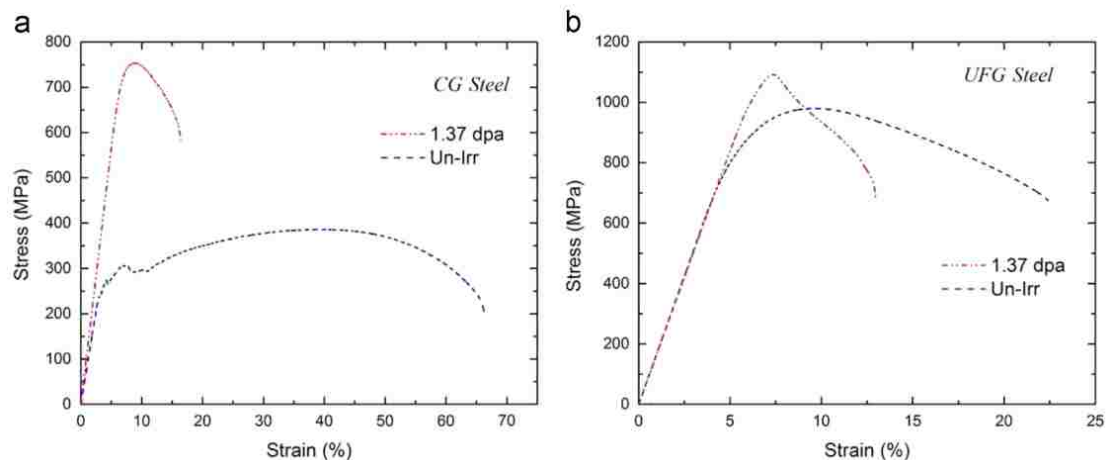


Figure 1.8. Stress strain curves comparing neutron irradiated coarse grained and ultrafine grained ferritic steel. The ultrafine grained steel shows increased resistance to radiation induced embrittlement [19].

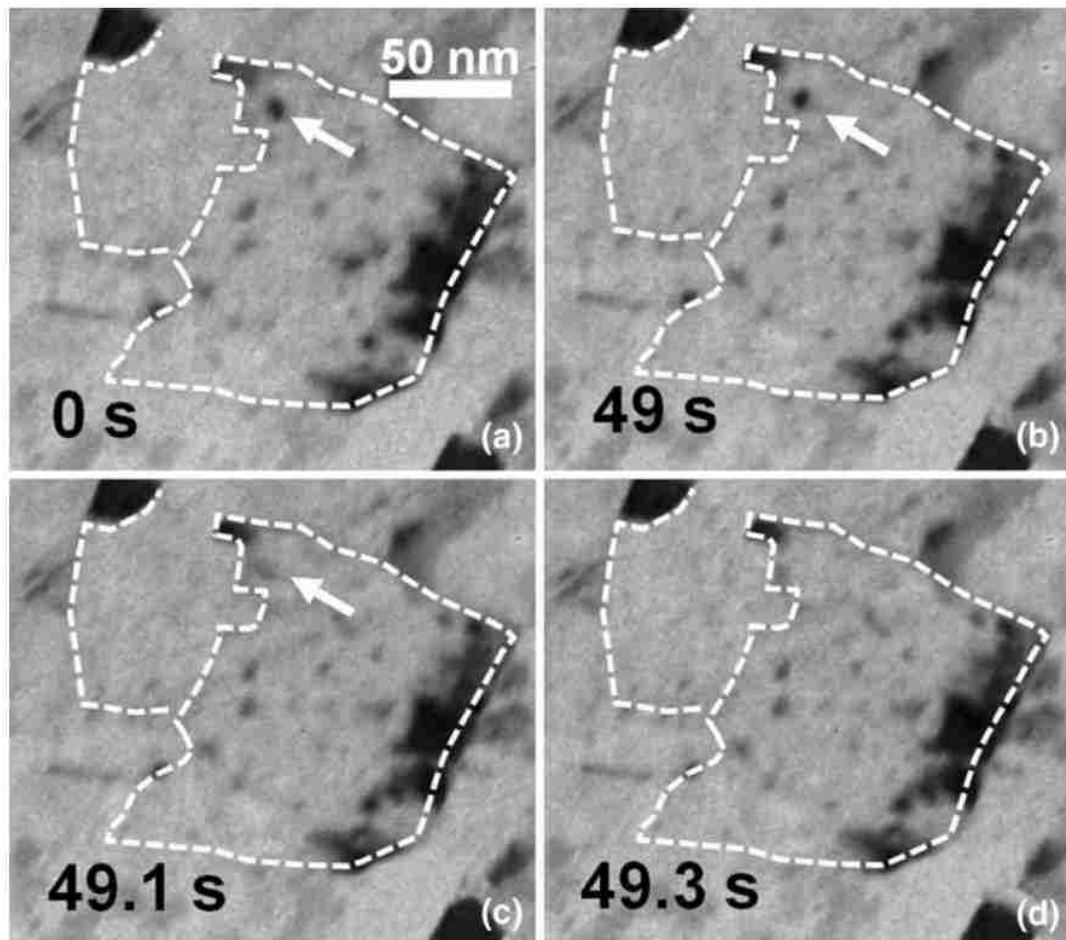


Figure 1.9. In-situ images of a radiation induced defect cluster being absorbed by and annihilating at a grain boundary in nanocrystalline Ni [18].

Nanostructured materials utilize interfaces as defect sinks and introduce a high density of nanosized features in order to create these interfaces [20]. These can be phase interfaces as is the case of oxide dispersion strengthened steels [21] or MAX phase ceramics [22] or they can be grain boundaries which have also been shown to be effective radiation induced defects sinks as seen in Figure 1.8 [18]. Nanograined materials rely on grain refinement in order to increase the volume fraction of grain boundaries by reducing the grain size. This has been shown to be effective at reducing the radiation induced

embrittlement [19] and even RIS [23,24]. However, this is still a new class of materials, and more work needs to be done in order to determine the effectiveness of nanostructured steels to replace conventional steels in nuclear reactors.

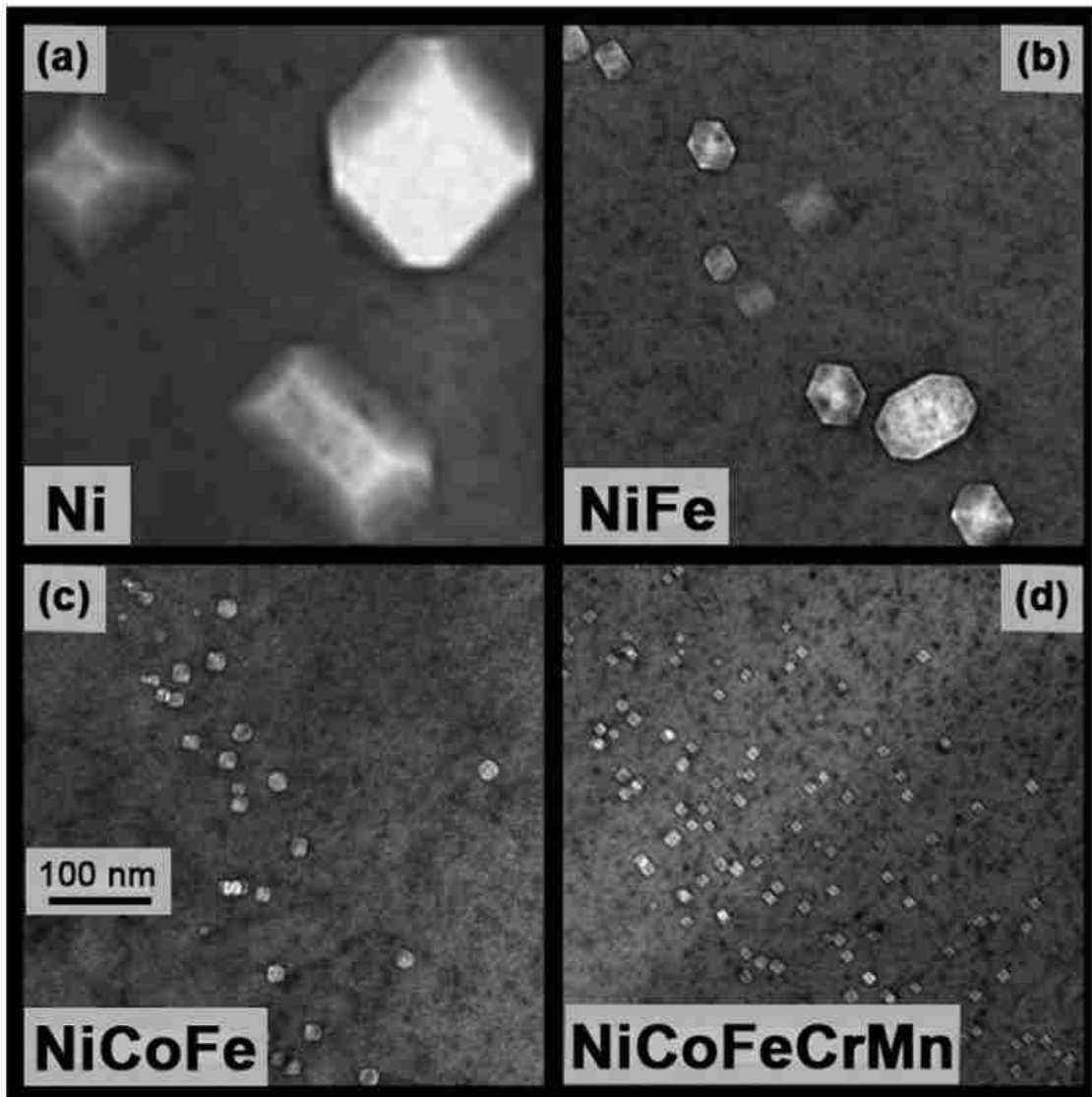


Figure 1.10. Images of voids in increasingly complex Ni alloys, showing the most complex high entropy alloy to have the greatest resistance to irradiation induced void swelling [25].

HEAs are a new class of multicomponent alloys that have exceptional phase stability due to their high entropy of mixing from which they gained their name. In addition to good phase stability, HEAs have shown promise in having high strength and even good corrosion resistance [26–29]. These properties come from not only their high mixing entropy, but the high interatomic strain due to the difference in size of the atoms in solid solution, sluggish diffusion, and what is described as the “cocktail effect” which describes the unique interactions of different species with each other [26]. HEAs have generated interest for the use in nuclear applications due to their sluggish diffusion preventing defects from agglomerating and forming larger structures. As is seen in Figure 1.10, HEAs form significantly smaller voids and dislocation loops that conventional alloys [30–33]. While HEAs do show significant promise as radiation resistant materials, many of the HEA compositions contain Co. Co does not make for a good material in nuclear reactor environments as it has only one natural isotope (Co-59) which will activate to during neutron irradiation. Thus, materials with Co will be highly radioactive after service causing waste concerns. Therefore more work is needed on evaluating Co-free HEAs and their properties under irradiation as only limited study has been conducted on these alloys [31].

1.3. MANUFACTURING NANOSTRUCTURED STEELS THROUGH SEVERE PLASTIC DEFORMATION

When producing nanostructured materials, there are two possible approaches: bottom up and top down. The bottom up approach involves the consolidation of nanosized particles (often metal powders). Some examples of consolidation techniques are spark plasma sintering (SPS) [34] and hot isostatic pressing (HIP) [35]. These

techniques are designed to allow for the fusing of particles without supplying the thermal energy required for grain growth. SPS, for example, utilizes current and pressure in order to allow for densification at lower temperatures and shorter times effectively reducing grain growth [34,36].

In contrast, a top down approach involves techniques where conventional coarse grained (CG) materials undergo severe plastic strain. Increase in strain results in the formation of new dislocations, and over time these dislocations accumulate. These dislocations will form structures such as dislocation cells or walls (which can also be low angle grain boundaries). As more dislocations accumulate at the cell boundaries, the cell will be rotated until eventually it forms a new high angle grain boundary. There are many severe plastic deformation (SPD) techniques such as cryomilling [37] and cryoforging [38], but the two SPD techniques which account for most studies are equal channel angular pressing (ECAP) and high pressure torsion (HPT) [39].

HPT is a technique in which high torsional strain is applied to a sample by a rotating anvil under high pressure. ECAP is a technique in which samples are extruded through a bent die (typically 90 or 120-degrees) which two equal diameter channels. As samples are extruded, radial shear occurs across the bend in the channel. If samples are extruded in the same orientation, only a limited number of slip planes will be activated which inhibits effective grain refinement. Therefore, in this work samples are rotated 90 degrees clockwise in between each pass which is also known as the B_c route [41].

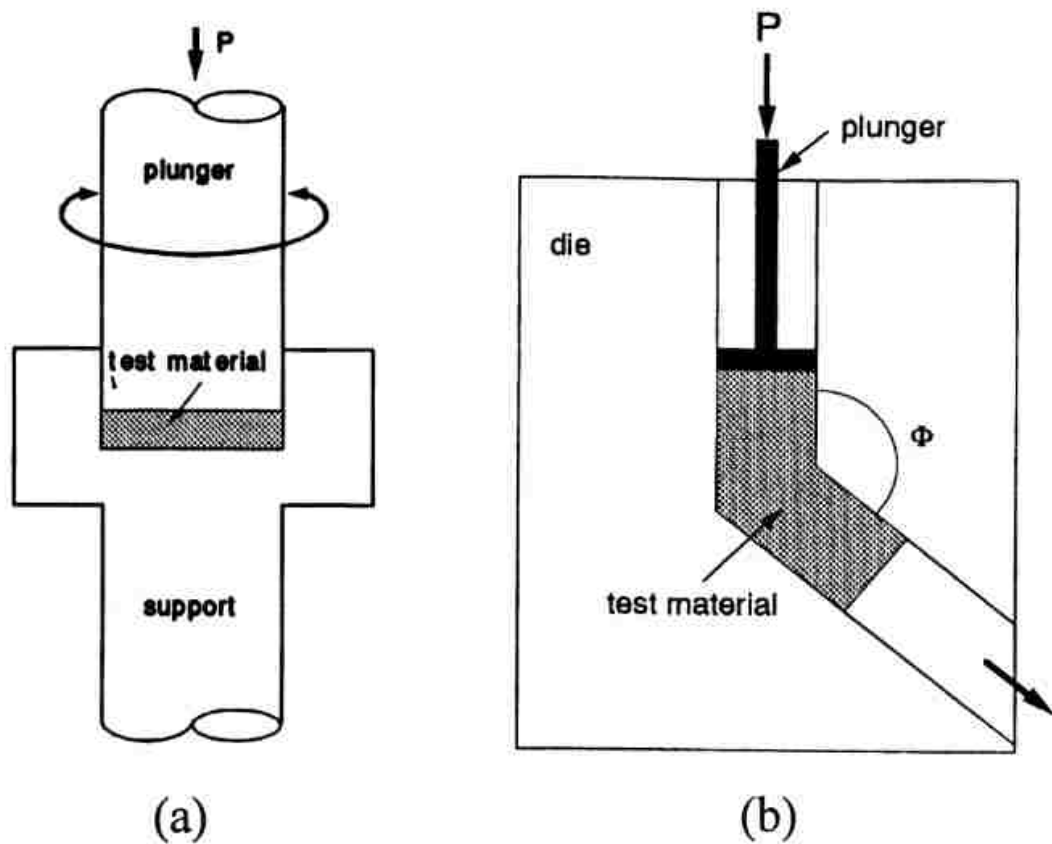


Figure 1.11. Schematic of a) high pressure torsion and b) equal channel angular pressing [40].

When comparing HPT and ECAP, HPT is capable of much higher strains, and thus is a more effective grain refinement technique. HPT suffers, however, from the size of samples produced as samples by nature must be thin discs. ECAP, on the other hand, has the potential to be scaled up to industrial scale using a rolling method sometimes referred to as ECAP-conform [42]. In this study, HPT is used to understand the basic science of nanocrystalline steel while ECAP is used to study the feasibility of industrial production of ultrafine grained reactor structural steels.

PAPER**■ HIGH-PRESSURE TORSION ASSISTED SEGREGATION AND PRECIPITATION IN A FE-18CR-8NI AUSTENITIC STAINLESS STEEL**

Andrew Hoffman¹, Haiming Wen^{1,2,*}, Rinat Islamgaliev³, Ruslan Valiev³

¹Department of Mining and Nuclear Engineering, Missouri University of Science and Technology, Rolla, MO 65409, USA

²Department of Materials Science and Engineering, Missouri University of Science and Technology, Rolla, MO 65409, USA

³Institute of Physics of Advanced Materials, Ufa State Aviation Technical University, Ufa 450008, Russia

*Corresponding author: wenha@mst.edu; Tel.: +1-573-341-6167

ABSTRACT

During irradiation or high-temperature aging, stainless steel can develop precipitates, significantly affecting mechanical properties. In this study atom probe tomography (APT) was used to study grain boundary segregation and secondary phases in a purely austenitic SS304 (a Fe-18Cr-8Ni steel) processed by high-pressure torsion (HPT) at 300 °C. Ni, Mn, Si enriched phase was observed at grain boundaries, and Cu nanoprecipitates were observed along and near phase/grain boundaries. Precipitation is facilitated by deformation assisted segregation along grain boundaries with a mechanism similar to vacancy diffusion in irradiated steels.

Keywords: Nanocrystalline Materials, Segregation, Atom Probe Tomography, Severe Plastic Deformation, Diffusion, High Pressure Torsion

1. INTRODUCTION

SS304 is an Fe-Cr-Ni austenitic steel used in many industrial applications due to its good mechanical properties and corrosion resistance. When aged for extremely long times at elevated temperatures secondary phases can form including g-phase (a Ni silicide) [1]. Under irradiation conditions, it is also common to see Ni-Si clusters, which are assumed to be g-phase at early stages of formation [2]. Cu precipitation is common in irradiated reactor pressure vessel steels [3], but has rarely been studied in austenitic steels because they are designed to have little or no Cu.

In addition to precipitation, radiation induced segregation (RIS) is also observed in steels. This RIS behavior is a result of vacancy flux through the inverse-Kirkendall effect [4]. Because severe plastic deformation (SPD) produces a large number of vacancies [5,6], it is suggested that a similar mechanism can occur in SPD processed steels. Simulations have shown that plastic deformation at high temperatures can enhance solute segregation, primarily due to vacancy super-saturation [7]. This is supported by experimental data showing that SPD can enhance secondary phase formation [8] and cause GB segregation [9,10]. In this study APT was used to identify grain boundary segregation, early stages of g-phase precipitates along GBs and Cu rich precipitates along and near GBs in SS304 subjected to HPT at 300 ° C.

2. EXPERIMENTAL

SS304 commercial bar stock (composition shown in Table 1) was normalized at 1050 °C for one hour followed by water quenching. HPT discs were processed at 300 °C under 6 GPa of pressure for 10 rotations at 0.2 rotations per minute with a final thickness of ~1.3mm. X-ray diffraction (XRD) was performed before and after HPT using a Phillips X'PERT MPD with a Cu source. MAUD software was used to perform XRD analysis using Rietveld Refinement. A Technai F20 transmission electron microscope (TEM) was used to determine average grain size, and TEM samples were prepared using a standard focused ion beam (FIB) lift-out technique. APT tips were prepared using FIB lift-out on a Quanta 3D FEG scanning electron microscope (SEM)/FIB. The APT tips were examined using a CAMECA LEAP 4000X HR atom probe. APT was performed in voltage mode at 55 K with a target pulse fraction of 0.2 and a detection rate of 0.7%. Reconstruction and data analyses were carried out using the CAMECA IVAS software.

3. RESULTS AND DISCUSSION

Figure 1a shows an TEM image of the microstructure of SS304 after HPT processing at 300 °C. Average grain size from 315 grains was 89 ± 25 nm. A high dislocation density is evident from TEM and the estimated dislocation density from XRD is a magnitude of 10^3 higher after HPT. Figure 1b displays the XRD results of SS304 samples before and after HPT at 20, 200, and 300 °C. After HPT at both 200 and 300 °C no peak corresponding ferrite/martensite is present. Before HPT, a small amount of BCC

was detected by XRD (likely formed during quenching). After HPT at 20 °C, a significant amount of BCC phase is present due to the deformation induced martensite transformation (DIMIT) [11]. At 200 and 300 °C, the temperature is high enough to suppress this transformation, and no BCC peak is found which agrees with previous HPT experiments on SS304 [11]. It can be concluded from both XRD and TEM that the microstructure is comprised of austenite, and not duplex austenite-martensite/ferrite.

Figure 2 shows the results from one APT analysis volume where two secondary phases are distinct. The larger precipitates are enriched in Ni, Mn, and Si. Smaller Cu enriched nanoprecipitates are also observed which formed along and near the interfaces between the matrix and the Ni-Mn-Si phase and along and near one GB. A proximity histogram concentration profile (proxigram) of a Ni-Mn-Si enriched precipitate based on a 11 at.% Ni isoconcentration surface is displayed in Figure 2b, indicating that the Ni, Mn, and Si contents in the precipitate are approximately twice those in the matrix. These Ni-Mn-Si enriched precipitates have ~14 at.% Ni, and ~1.5 at.% Mn/Si. While these precipitates are not fully developed, their compositions match that of early-stage g-phase. Cu precipitates have Cu concentration varying from ~60 to ~1 at.%. An example proxigram of one Cu-rich precipitates is displayed in Figure 2c. It is inferred that the Cu-rich precipitates will eventually form pure Cu. The lower Cu content observed from APT is likely due to two reasons: there is trajectory aberration in APT [12] due to a difference in the evaporation field between the precipitate and matrix causing matrix atoms to be detected within the small precipitates and these precipitates are in the early stages of nucleation/growth so the Cu content is expected to be lower than that in fully developed

precipitates. While some of the Cu precipitates are as large as 10 nm, the average volume equivalent diameter was 4.1 ± 2.6 nm.

Solute segregation along GBs is also identified. Figure 3 a and b are 1-d concentration profiles across two GBs from Figure 2a, showing segregation of Ni, Mn, Si, and P along the GBs. The two GBs have different characteristics in that one is enriched in P, and the other is not. The P enriched GB also has Cu precipitates along it. It is assumed the differences in segregation are due to GB character which is known [2]. Figure 3c shows another APT analysis volume in which one GB was identified, and both P and Si are enriched at the GB (as seen in figure 3d), providing further evidence of GB segregation during deformation.

Because of the inter-precipitate distance (it matches with TEM grain size), segregation behavior, and the plate like shape, it is suggested that the g-phase has precipitated along GBs due to (especially) Ni and Si segregation. GB segregation may also partially account for Cu precipitation. Cu is predicted to be depleted at GBs but pile up adjacent to the GBs [13]. When this pileup occurs, the Cu concentration will be too high for Cu to remain in solid solution and it will precipitate out along and near the GBs. Similar formation of Cu precipitates along GBs assisted by RIS has also been observed in irradiated SS304 [2].

4. CONCLUSIONS

APT was conducted on SS304 subjected to HPT at 300 °C. Nanoscale precipitates were identified as Ni-Mn-Si enriched g-phase and Cu enriched precipitates. G-phase

precipitates formed along GBs due to enrichment of Ni and Si along GBs. Cu precipitates are primarily formed along and near grain and phase boundaries; the formation is suggested to be caused by Cu pileup near the GBs, increasing the concentration of Cu beyond its solubility in the matrix. This precipitation behavior in the severely plastic deformed 304 is unusual for a SS304 that has not been high-temperature aged or irradiated. It is suggested that the cause of this precipitation behavior is a combination of an increase in nucleation sites (GBs and dislocations), and an increase in point defects that enhances diffusion and facilitates kinetically driven segregation at GBs, similar to RIS.

ACKNOWLEDGEMENTS

This research is financially supported by U.S. Department of Energy, Office of Nuclear Energy through the NEET-NSUF (Nuclear Energy Enabling Technology - Nuclear Science User Facility) program (award number DE-NE0008524). R. Islamgaliev is grateful to the Russian Ministry of Education for the project No. 16.2061.2017/4.6. R. Valiev acknowledges St. Petersburg State University for Call 3 project (id 26130576). APT work was performed at the Center for Advanced Energy Studies (CAES), and Dr. Yaqiao Wu is thanked for his assistance. Partial support for Andrew Hoffman came from the Nuclear Regulatory Commission Graduate Fellowship Program.

Table 1. Elemental composition of SS304

Element	Fe	Cr	Ni	Mn	Cu	Si	Mo	Ti	C
wt.%	Bal.	17.33	8.97	1.13	0.64	0.37	0.29	0.28	0.014

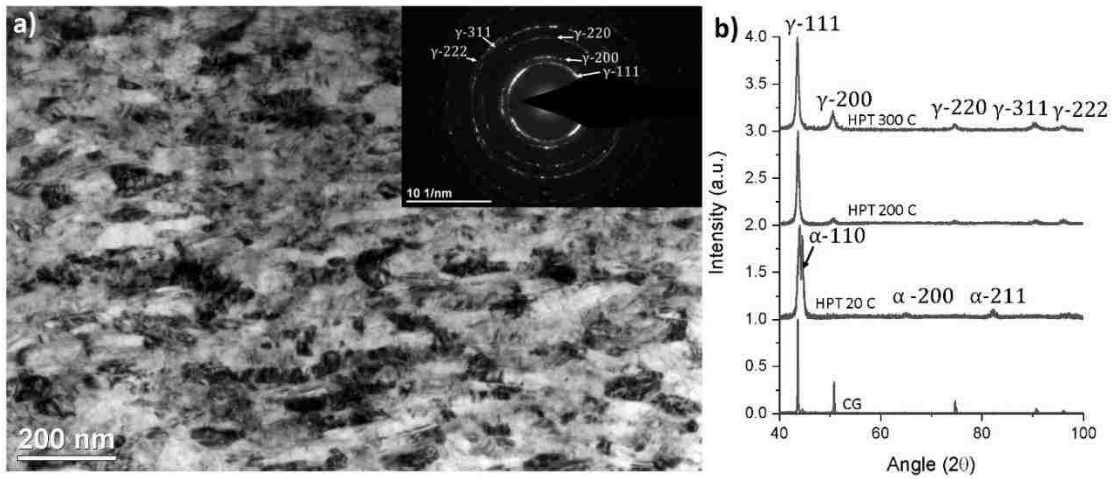


Figure 1. a) TEM bright-field image showing general microstructure of SS304 after HPT with inset selected-area electron diffraction pattern showing pure austenitic structure; b) XRD patterns of SS304 before HPT [coarse-grained (CG)] as well as after HPT at several different temperatures. After HPT at 200 and 300 °C, no body-centered cubic (BCC) or body-centered tetragonal (BCT) phase is present.

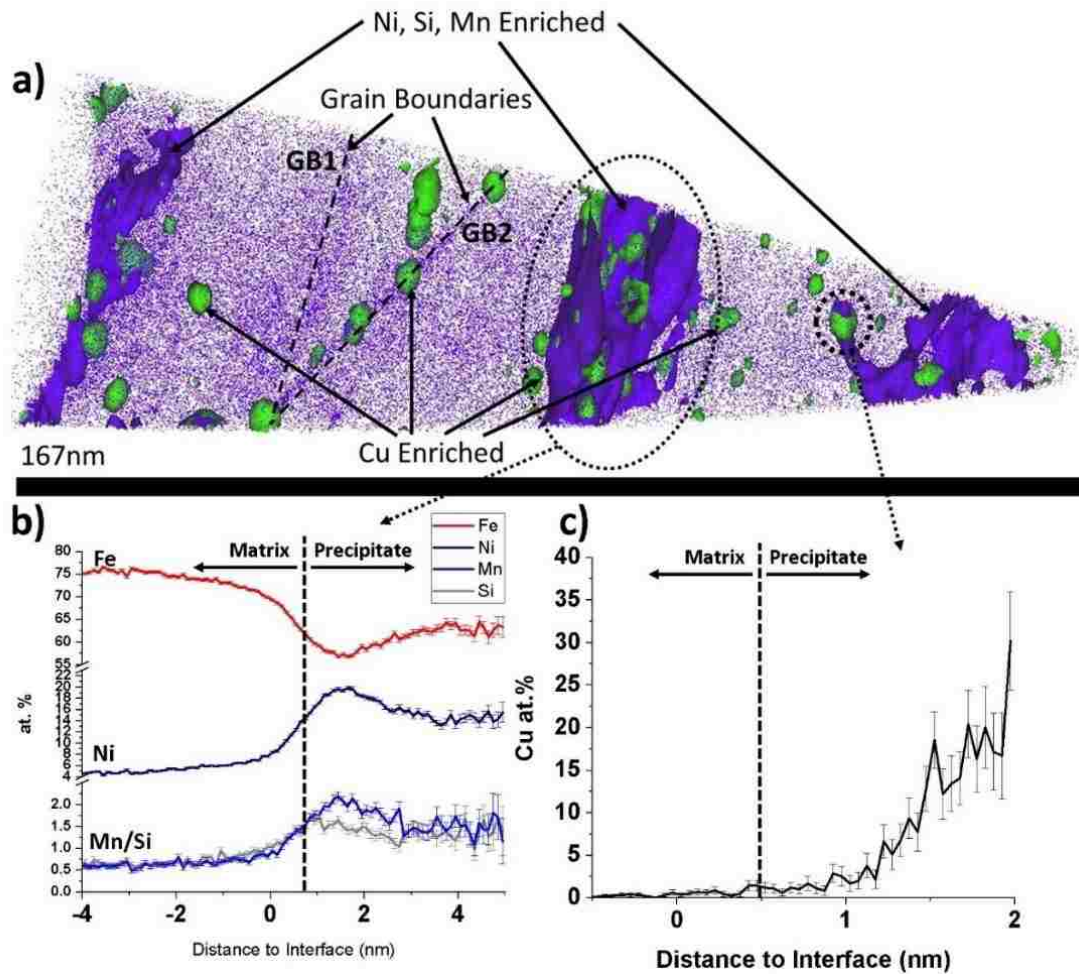


Figure 2. a) APT reconstruction with Ni atoms displayed and isoconcentration surfaces of 11 at.% Ni and 0.9 at.% Cu superimposed. b) proximity histogram concentration profile of the middle Ni-Si-Mn enriched precipitate in a); c) proximity histogram concentration profile showing Cu concentration of the Cu-rich nanoprecipitate indicated in a).

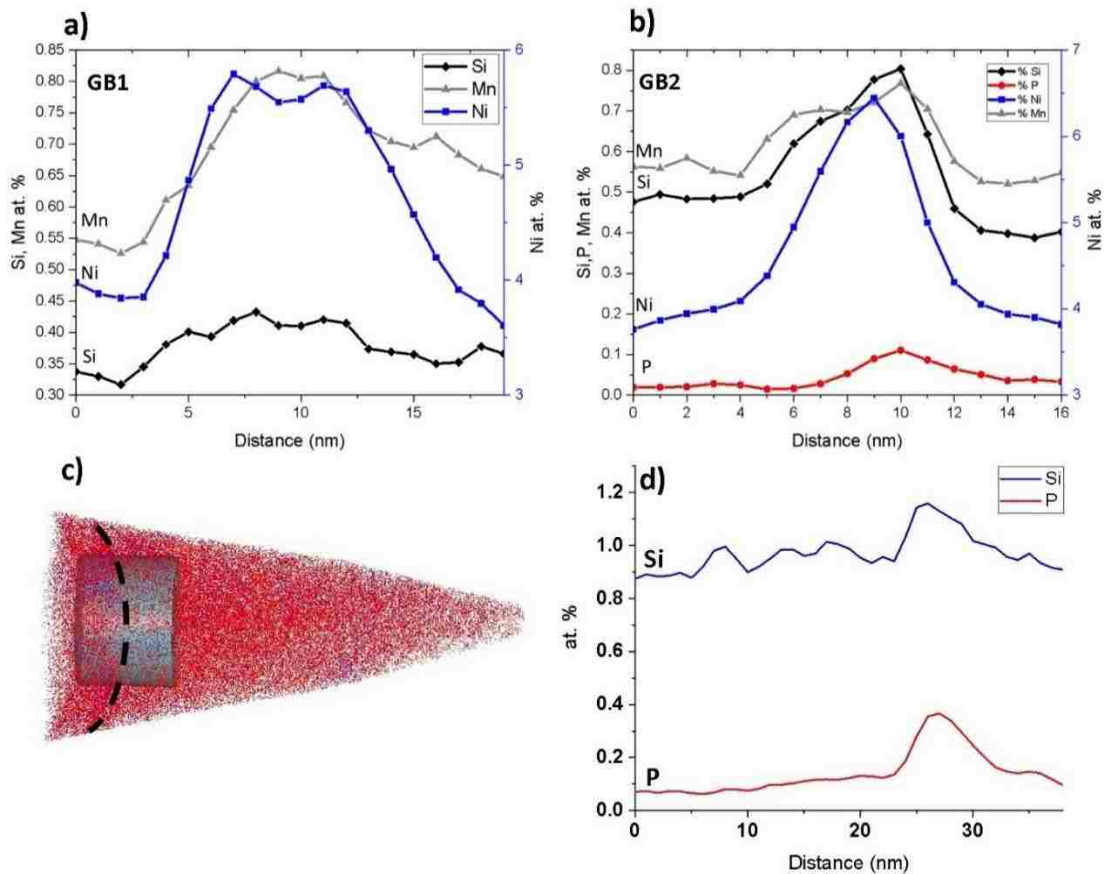


Figure 3 a) and b) 1-D concentration profiles of grain boundaries in figure 2a. c) APT reconstruction showing P (red) and Si atoms (blue), a grain boundary and a cylinder region of interest across it; d) 1-D concentration profile across the grain boundary indicated in c) showing segregation of Si and P along the grain boundary.

REFERENCES

- [1] T. Takeuchi, Y. Kakubo, Y. Matsukawa, Y. Nozawa, T. Toyama, Y. Nagai, Y. Nishiyama, J. Katsuyama, Y. Yamaguchi, K. Onizawa, M. Suzuki, Effects of thermal aging on microstructure and hardness of stainless steel weld-overlay claddings of nuclear reactor pressure vessels, *J. Nucl. Mater.* 452 (2014) 235–240. doi:10.1016/j.jnucmat.2014.04.003.
- [2] Z. Jiao, G.S. Was, Novel features of radiation-induced segregation and radiation-induced precipitation in austenitic stainless steels, *Acta Mater.* 59 (2011) 1220–1238. doi:10.1016/j.actamat.2010.10.055.

- [3] K. Lindgren, M. Boåsen, K. Stiller, P. Efsing, M. Thuvander, Evolution of precipitation in reactor pressure vessel steel welds under neutron irradiation, *J. Nucl. Mater.* 488 (2017) 222–230. doi:10.1016/j.jnucmat.2017.03.019.
- [4] T.R. Allen, On the mechanism of radiation-induced segregation in austenitic Fe – Cr – Ni alloys, *J. Nucl. Mater.* (1998) 44–58. doi:10.1016/S0022-3115(98)00010-5.
- [5] W. Lechner, W. Puff, B. Mingler, M.J. Zehetbauer, R. Würschum, Microstructure and vacancy-type defects in high-pressure torsion deformed Al-Cu-Mg-Mn alloy, *Scr. Mater.* 61 (2009) 383–386. doi:10.1016/j.scriptamat.2009.04.027.
- [6] D. Setman, E. Schafner, E. Korznikova, M.J. Zehetbauer, The presence and nature of vacancy type defects in nanometals deformed by severe plastic deformation, *Mater. Sci. Eng. A.* 493 (2008) 116–122. doi:10.1016/j.msea.2007.06.093.
- [7] S.H. Song, X.M. Chen, L.Q. Weng, Solute diffusion during high-temperature plastic deformation in alloys, *Mater. Sci. Eng. A.* 528 (2011) 7196–7199. doi:10.1016/j.msea.2011.06.015.
- [8] K. Oh-Ishi, K. Edalati, H.S. Kim, K. Hono, Z. Horita, High-pressure torsion for enhanced atomic diffusion and promoting solid-state reactions in the aluminum-copper system, *Acta Mater.* 61 (2013) 3482–3489. doi:10.1016/j.actamat.2013.02.042.
- [9] G. Sha, K. Tugcu, X.Z. Liao, P.W. Trimby, M.Y. Murashkin, R.Z. Valiev, S.P. Ringer, Strength, grain refinement and solute nanostructures of an Al-Mg-Si alloy (AA6060) processed by high-pressure torsion, *Acta Mater.* 63 (2014) 169–179. doi:10.1016/j.actamat.2013.10.022.
- [10] M.M. Abramova, N.A. Enikeev, R.Z. Valiev, A. Etienne, B. Radiguet, Y. Ivanisenko, X. Sauvage, Grain boundary segregation induced strengthening of an ultrafine-grained austenitic stainless steel, *Mater. Lett.* 136 (2014) 349–352. doi:10.1016/j.matlet.2014.07.188.
- [11] Y. Mine, D. Haraguchi, Z. Horita, K. Takashima, High-pressure torsion of metastable austenitic stainless steel at moderate temperatures, *Philos. Mag. Lett.* 95 (2015) 269–276. doi:10.1080/09500839.2015.1051602.
- [12] E.A. Marquis, F. Vurpillot, Chromatic aberrations in the field evaporation behavior of small precipitates, *Microsc. Microanal.* 14 (2008) 561–570. doi:10.1017/S1431927608080793.
- [13] K.C. Russell, Phase stability under irradiation, *Prog. Mater. Sci.* 28 (1984) 229–434. doi:10.1016/0079-6425(84)90001-X.

■ **ENHANCED RESISTANCE TO IRRADIATION-INDUCED SEGREGATION AND PRECIPITATION IN A NANOCRYSTALLINE FE-18CR-8NI STEEL**

Andrew Hoffman¹, Haiming Wen^{1,2,*}, Maalavan Arivu², Rinat Islamgaliev³, Ruslan Valiev³, Li He⁴, Kumar Sridharan⁴, Yaqio Wu^{5,6}

¹Department of Mining and Nuclear Engineering, Missouri University of Science and Technology, Rolla, MO 65409, USA

²Department of Materials Science and Engineering, Missouri University of Science and Technology, Rolla, MO 65409, USA

³Institute of Physics of Advanced Materials, Ufa State Aviation Technical University, Ufa 450008, Russia

⁴Department of Engineering Physics, University of Wisconsin, Madison, WI 53706

⁵Micron School of Materials Science and Engineering, Boise State University, Boise, ID 83725

⁶Center for Advanced Energy Studies, Idaho Falls, ID 83401

*Corresponding author: wenha@mst.edu; Tel.: +1-573-341-6167

ABSTRACT

Nanocrystalline SS304 (Fe-18Cr-8Ni) austenitic steel was produced using high-pressure torsion at 300°C, and atom probe tomography (APT) was used to study grain boundary (GB) segregation and precipitation after annealing and self-ion irradiation at 500°C. The degree of radiation-induced segregation was significantly reduced with decreasing grain size, owing to reduced irradiation-induced defects. Precipitation was also significantly reduced with a decrease in grain size. After irradiation, some nanocrystalline GBs showed segregation behavior similar to annealed samples, indicating that with sufficiently small grain size, thermodynamic effects can dominate kinetic

effects of irradiation. Nanostructuring may therefore enhance phase stability and reduce corrosion during irradiation.

Keywords: Nanocrystalline Materials, Radiation Induced Segregation, Atom Probe Tomography, Severe Plastic Deformation, Diffusion, High Pressure Torsion

Grade 304 austenitic stainless steel (SS304) is commonly used as a structural material in light-water reactors. In high temperature conditions, it is common for 300 series steels to develop Cr enriched $M_{23}C_6$ carbides on or near GBs, which can then lead to Cr depletion in the grain interiors. Additionally, under irradiation conditions, irradiation-induced defect flux towards GBs leads to Cr depletion at GBs [1–3]. While its high Cr content enhances corrosion resistance, the depletion of Cr allows corrosion to occur along the GBs and this eventually contributes to stress corrosion cracking (SCC) [4]. It is therefore important to find ways to improve resistance to this irradiation-induced depletion at GBs in austenitic steels. One approach of interest is to increase the volume fraction of defect sinks (i.e., phase boundaries and GBs) through the nanostructuring of commercial steels, including both oxide dispersion strengthened steels and grain-refined steels [5]. Recent developments in manufacturing nanostructured steels include using severe plastic deformation (SPD) techniques, such as equal-channel angular pressing (ECAP) and high-pressure torsion (HPT) [6–8]. These ultrafine-grained (UFG, $100\text{nm} < \text{grain size} < 1\mu\text{m}$) and nanocrystalline (NC, grain size $< 100\text{nm}$) materials have already been proven to be effective in reducing radiation-induced damage [9–11].

In the case of Fe-Cr-Ni austenitic steels, it is well known that, during irradiation, Ni and Si will be enriched at GBs [3,12]. The enrichment of Ni and Si at GBs can lead to the formation of g-phase [13] and the depletion of Ni in the matrix, reducing austenite stability, which can cause the formation of ferrite [14]. Radiation induced segregation (RIS) is, in large part, caused by the inverse-Kirkendall effect (IKE), which is when the matrix is super saturated with vacancies and there is a continuous flux of vacancies towards defect sinks (GBs) [15]. As vacancies diffuse towards the GBs, fast diffusing atoms (in the case of austenitic steels, Fe and Cr) will travel opposite to the flow of vacancies causing the GBs to be depleted of these elements and enriched in slow diffusing atoms (Ni and Si). It is therefore anticipated that reducing the supersaturation of vacancies in the matrix through nanostructuring should reduce RIS. The reduced vacancy concentration also has the effect of reducing homogeneous nucleation of precipitates within grains, because vacancies are important for homogenous nucleation. While RIS can occur in nanostructured steels [16], a previous study has shown that RIS and intragranular cluster formation in NC 316 stainless steel is significantly reduced compared to its coarse-grained counterpart [17]. This field, however, requires additional work in exploring the effects of varying grain sizes and evaluating the corresponding compositions on GB segregation behavior.

Since there can be competing effects during elevated-temperature irradiation between thermodynamics and the defect flux driven kinetics, it is important to understand the differences in GB segregation behavior under various conditions. In our previous study, we showed that SPD performed at moderate temperatures (300°C) caused Ni and Si segregation at the GBs in SS304, which facilitated the early-stage precipitation of g-

phase along the GBs [18]. This study is consistent with earlier work that showed GB segregation during elevated-temperature SPD and no segregation after low-temperature SPD [19]. Other studies performed on HPT of SS304 at room temperature, resulting in a purely ferritic microstructure, indicated precipitation of g-phase after short-term annealing [20,21]. In this work, we compared the segregation behavior in a NC austenitic SS304 (manufactured using HPT at 300°C) after annealing at 500°C for 24 hours to that after self-ion irradiation up to 50 displacements per atom (dpa) at 500°C. It was shown that the NC material had enhanced resistance to RIS and precipitation and that some GBs even exhibited thermodynamically dominant segregation behavior comparable to that in the annealed sample.

SS304 samples were prepared from commercial bar stock with a composition shown in Table 1. Bar stock was normalized at 1050 °C for 1 hour and water quenched. HPT discs were processed at 300 °C under 6 GPa of pressure for 10 rotations at 0.2 rotations per minute with a final thickness of ~1.3 mm. Some HPT discs were annealed in an argon atmosphere in a vacuum tube furnace at 500°C for 24 hrs. Irradiation was performed on as-processed HPT discs using 3.7 MeV Fe²⁺ ions at 500°C with a maximum calculated dose of 50 dpa using SRIM software. APT tips were prepared using focused ion beam (FIB) lift-out on a Quanta 3D FEG scanning electron microscope (SEM)/FIB. FIB lift outs were milled so that the top of the APT tips came from the region ~800-900nm from the surface, which corresponded to a dose of 45-50 dpa. APT experiments were performed using a CAMECA LEAP 4000X HR atom probe. APT was performed in laser mode at 55K, with a laser energy of 40pJ, and a target evaporation rate of 0.007. Reconstruction and data analyses were carried out using the CAMECA IVAS

software. Figure 1a displays an APT reconstruction of SS304 after HPT (hereafter called HPT304) showing Ni atoms (purple), and the associated 1-D concentration profile across a GB in Figure 1b indicates Ni enrichment at the GBs, which was previously reported [18]. Notably, the previous study showed that the sample was fully austenitic after HPT. Figure 1c displays an APT reconstruction of HPT304 after annealing at 500°C for 24hrs showing Ti atoms (blue) and several GBs denoted by the Ti segregation. In Figure 1d, the 1-D concentration profiles across the GB (shown in Figure 1c) indicate that Ni was no longer enriched at the GBs after annealing and, instead, Cr was enriched. Moreover, Mo, Ti and C were also enriched at the GBs after annealing. Cr and Mo are known to enrich at the GBs in austenitic steels during heat treatments [22]. P and Si were also found to be enriched at the GBs after HPT and after annealing of the HPT sample. While 24 hours is not likely to be sufficient time for the system to come to full equilibrium, it is clear that thermodynamic segregation behavior is significantly different from that observed after SPD. Also, in the previous APT study of HPT304 [18], Cu precipitates were found along and near grain/phase boundaries and the early stages of Ni-Mn-Si g-phase were found along GBs. After annealing Cu and g-phase precipitates were not found; it is believed that these precipitates had gone back into solid solution during annealing. While the average grain size observed after HPT was 85nm, transmission electron microscopy (TEM) revealed irradiation induced grain growth within the material (see supplemental Figure S2). This was expected, based on previous results on irradiated NC materials [16,23]. While NC grains remained after irradiation, there were also grains in the UFG size regime with grain sizes up to 300nm. Figures 2a and 2d show two different APT reconstructions of HPT304 after irradiation at 500°C to 45-50 dpa, with Si atoms (grey),

and Si isoconcentration surfaces that highlight GB locations. Figure 2a shows primarily one large ultrafine grain in the reconstruction volume, as compared to that in Figure 2d where many nanocrystalline grains are depicted. While both regions exhibit the anticipated RIS, which is depletion of Fe and Cr, and enrichment of Ni, Si and Co, there were two distinct differences. First, the amount of depletion of Cr and enrichment of Ni and Si was much smaller in the NC grains. Second, Mo was depleted (~ -0.1 at.%) at some GBs in the UFG region, whereas no Mo depletion was observed in the NC grain regions. At the GBs in the UFG region, the depletion of Fe and Cr was -11.6 ± 6.0 Δ at.% and -7.3 ± 1.6 Δ at.%, respectively, and the enrichment of Ni, Si and Co was $+13.8 \pm 3.0$ Δ at.%, $+3.7 \pm 1.8$ Δ at.% and 0.2 ± 0.1 Δ at.%, respectively. In the NC region, the depletion of Fe and Cr at GBs was approximately -4.3 ± 1.4 Δ at.% and -3.9 ± 1.4 Δ at.%, respectively, and the enrichment of Ni, Si and Co was approximately $+5.3 \pm 1.8$ Δ at.%, $+2.2 \pm 0.6$ Δ at.% and 0.1 ± 0.04 Δ at.%, respectively.

Figure 3a shows another APT reconstruction volume from the NC regions in the irradiated HPT304, and Figures 3b and 3c display 1-D concentration profiles along the cylinder (Figure 3a) across one of the several GBs. The GB had Cr enrichment ($+1.5 \pm 0.9$ Δ at.%), as indicated in Figure 3b. The Cr-enriched GBs in this volume were also slightly enriched in Ni ($+2.0 \pm 1.0$ Δ at.%), but this Ni enrichment decreased significantly as compared to that in other NC regions. Si enrichment ($\sim +1.8$ Δ at.%) was also significantly less than that in other NC regions. It is seen in Figure 3c that these GBs were also enriched in Mo ($+0.4 \pm 0.1$ Δ at.%), with no enrichment of Co. No intragranular segregation was observed in any volume of the irradiated material, including the UFG

region, which is attributed to the lack of dislocations and dislocation loops in this material.

Precipitation was also observed in the irradiated HPT304 samples. Figure 4 displays three different APT reconstructions of irradiated HPT304, with Figure 4a showing the same reconstruction volume as that in Figure 2a where practically only one ultrafine grain was found. Within this larger grain, many Cu precipitates were observed, which had been anticipated, as Cu precipitates are common in irradiated ferritic reactor pressure vessel steels [24], observed as well in some austenitic steels with higher Cu content [25]. Within the smaller grains (Figures 4b and 4c), the number density of Cu precipitates was much lower, when any existed, and precipitate sizes were much smaller. A combined proximity histogram (proxigram) of all the Cu precipitates in Figure 4a is shown in Figure 4d. Figure 4e displays the combined proxigram of all the Cu precipitates in the boxed region of Figure 4c. The Cu concentration values indicate that, in both cases, precipitates were in the early stages of nucleation and growth. Notably, the larger precipitates in Figure 4c (bottom right) were due to the fact that they were in a ferritic grain with much lower Cu solubility.

Table 2 summarizes the segregation at GBs in the annealed and irradiated HPT304. For the irradiated condition, the NC regions have significantly reduced GB segregation, as compared to the UFG regions. Similar reduced RIS was also previously reported in NC SS316 ion irradiated at 350°C [10,17]. It is noted, however, that there have been limited studies of RIS in nanostructured steels, and it has been reported that RIS occurred with the same intensity in an ion irradiated NC SS316 at 350°C, as that in a neutron or proton irradiated CG SS316 [16]. This discrepancy between studies may be

due to the limited statistics of APT as very few GBs (often only one or two) can be observed in each reconstruction volume. With few statistics it is difficult to account for the effects of GB misorientation on segregation behavior [26]. While the statistics are also limited in this study, each region with unique RIS behavior include multiple GBs with supportive segregation characteristics. This study, therefore, confirms the enhanced resistance to RIS with decreasing grain size below 500nm even at temperatures up to 500°C. This reduced RIS includes a reduced depletion of Cr that should provide enhanced resistance to SCC, as well as limited enrichment of Ni and Si that can help suppress the formation of g-phase along the GBs and reduce depletion of Ni within the matrix enhancing the stability of the austenite phase. Herein we also report, for the first time, Cr enrichment at GBs in an irradiated austenitic steel. These Cr enriched NC GBs in irradiated HPT304 also had enrichment of Mo, with no Co enrichment, which matched the GB segregation behavior in the annealed HPT304 sample. This observation suggests that, if grain sizes are sufficiently small, the thermodynamic effects may dominate the kinetic effects, during elevated-temperature irradiation, in contrast with the fact that during irradiation of conventional coarse-grained metals the kinetic effects typically dominate, because of significant irradiation-induced defects.

In addition to RIS along GBs, it is common to see Ni and Si segregation in irradiated austenitic steels along dislocation loops, which can eventually form Ni₃Si precipitates [25,27–29]. These Ni and Si enriched precipitates were not observed in any previous studies of NC SS316 [10,16,17] or in this study of NC SS304. This is explained by the suppression of dislocation loop formation within the NC material, as was observed by Matsuoka et. al [30] where SS316 with grain sizes between 100-300nm had

significantly reduced irradiation-induced defects and associated hardening. In this study, Cu precipitates were observed in one large UFG (Figure 4a), which can be explained by the larger grain size allowing the development of defects that acted as nucleation sites for the Cu precipitates. Very few Cu precipitates were observed in NC grains (Figures 4b and 4c), whereas the number density of Cu precipitates was much higher in the UFG region. Thus, it is concluded that, even within the UFG/NC regime, decreased grain sizes can significantly reduce irradiation-induced precipitation, via reducing irradiation-induced defects. It is also important to distinguish between Cu precipitation during HPT and during irradiation. Although Cu precipitates were observed after HPT [18], they were near or at phase/grain boundaries, and it was assumed that the Cu precipitation during HPT was similar to that observed in irradiated coarse-grained 304 by Jiao and Was [25], which was attributed to the pile-up of Cu along the GBs due to RIS. In this study, because irradiation was performed at 500°C, the Cu precipitates that had formed after HPT likely went back into solid solution early in the irradiation, just as was observed in the annealed sample in this study. The precipitation observed after irradiation in this study was intragranular and was assumed to be associated with small defects that acted as nucleation sites within the grains. Notably, Cu precipitation is not commonly observed in austenitic steels due to low Cu content to avoid segregation and precipitation, however the commercial composition in this study contained 0.64 wt.% Cu which is similar to the content of the commercial purity 304 studied by Jiao and Was containing 0.42 wt.% Cu [25].

In summary, we studied the effects of annealing and irradiation at 500°C on segregation and precipitation in a NC SS304 manufactured using HPT at 300°C. After

annealing, Cr and Mo were enriched, and Fe was depleted at GBs. After irradiation, the GBs showed typical RIS, with enrichment of Ni, Si and Co, and depletion of Fe and Cr, however, enrichments and depletions were significantly less at the NC GBs, as compared to those at the UFG GBs. Some NC GBs showed Cr and Mo enrichment, which indicated that segregation along these GBs was driven by thermodynamic effects, rather than by the kinetic effects of irradiation. A high number density of Cu precipitates was observed in one UFG, whereas the majority of NC grains observed had little or no Cu precipitation. These results indicate that nanocrystalline samples have significant resistance to both radiation-induced segregation and precipitation, owing to the significantly reduced irradiation-induced defects. This property has advantages in reducing multiple irradiation-induced effects, including embrittlement due to precipitation, susceptibility to SCC due to Cr depletion, and austenite instability due to depletion of Ni from the matrix.

This research was financially supported by the U.S. Department of Energy, Office of Nuclear Energy through the NEET-NSUF (Nuclear Energy Enabling Technology - Nuclear Science User Facility) program (award number DE-NE0008524), and through the NSUF-RTE program (award number 17-865). Partial support for Andrew Hoffman came from the U.S. Nuclear Regulatory Commission Faculty Development Program (award number NRC 31310018M0044). RZV gratefully acknowledge the financial support from Saint Petersburg State University in the framework of Call 3 project (id 26130576). APT was conducted in the microstructural advanced characterization suite (MaCS) at the Center for Advanced Energy Studies (CAES).

Table 1. Bulk composition of SS304

Element	Wt. %
Fe	Bal
Cr	17.33
Ni	8.97
Mn	1.13
Cu	0.64
Si	0.37
Mo	0.29
Ti	0.28
P	0.033
N	0.04
C	0.014
S	< 0.002

Table 2. Summary of grain boundary segregation in annealed and irradiated HPT304

GB Description	# of GBs	Δat.% Fe	Δat.% Cr	Δat.% Ni	Δat.% Si	Δat.% Mo	Δat.% Co
Annealed	6	-3.5 \pm 2.4	+1.5 \pm 1.0	-	+0.6 \pm 0.4	1.2 \pm 0.7	-
Irradiated UFG	3	- 11.6 \pm 6.0	-7.3 \pm 1.6	+13.8 \pm 3.0	+3.7 \pm 1.8	-0.2 $>$	+0.2 \pm 0.1
Irradiated NC	18	-4.3 \pm 1.4	-3.9 \pm 1.4	+5.3 \pm 1.8	+2.2 \pm 0.6	-	+0.1 \pm 0.04
Irradiated NC Cr enriched	4	-6.6 \pm 2.6	1.5 \pm 0.9	+2.0 \pm 1.0	+2.0 \pm 0.3	+0.4 \pm 0.1	-

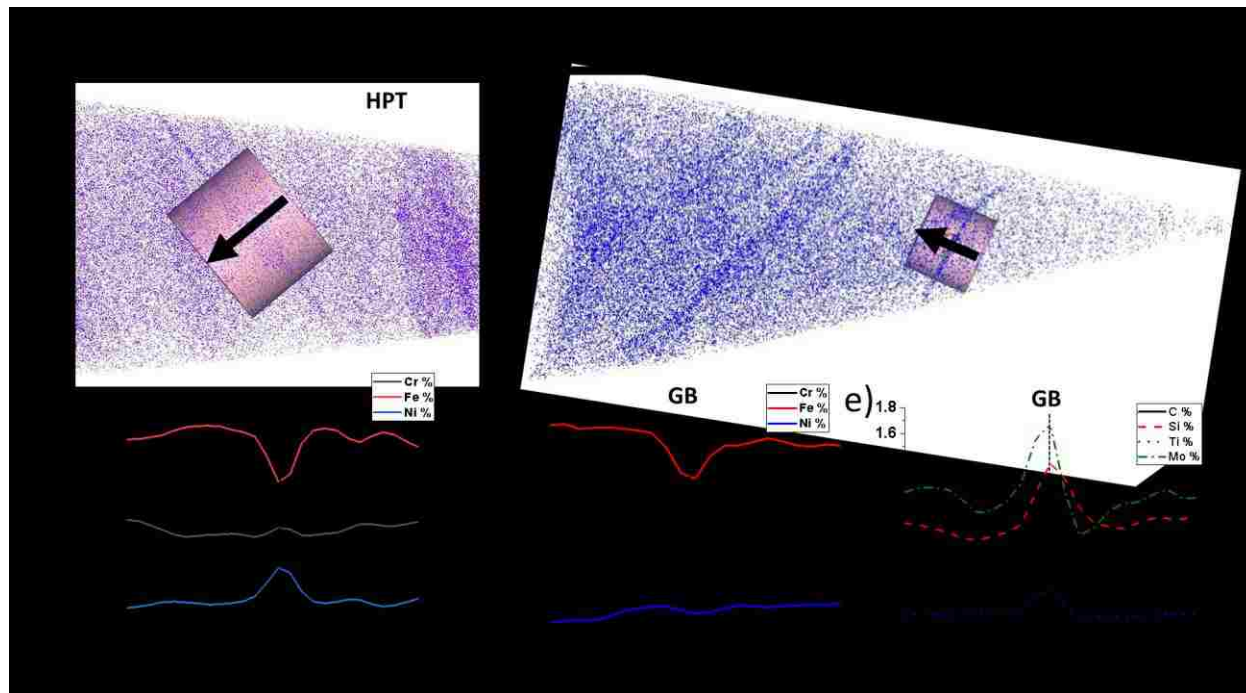


Figure 1. a) APT reconstruction of HPT304 showing Ni atoms (blue) and Ni segregation along one GB, b) 1-D profile across ROI shown in a) indicating Ni enrichment but no Cr depletion after HPT, c) APT reconstruction of HPT304 annealed at 500°C for 24 hours showing Ti atoms (blue); several GBs can be seen, d) and e) 1-D concentration profiles across the ROI shown in c) indicating Cr enrichment but no Ni depletion. Mo, Si, Ti, and C were all also enriched at the GB.

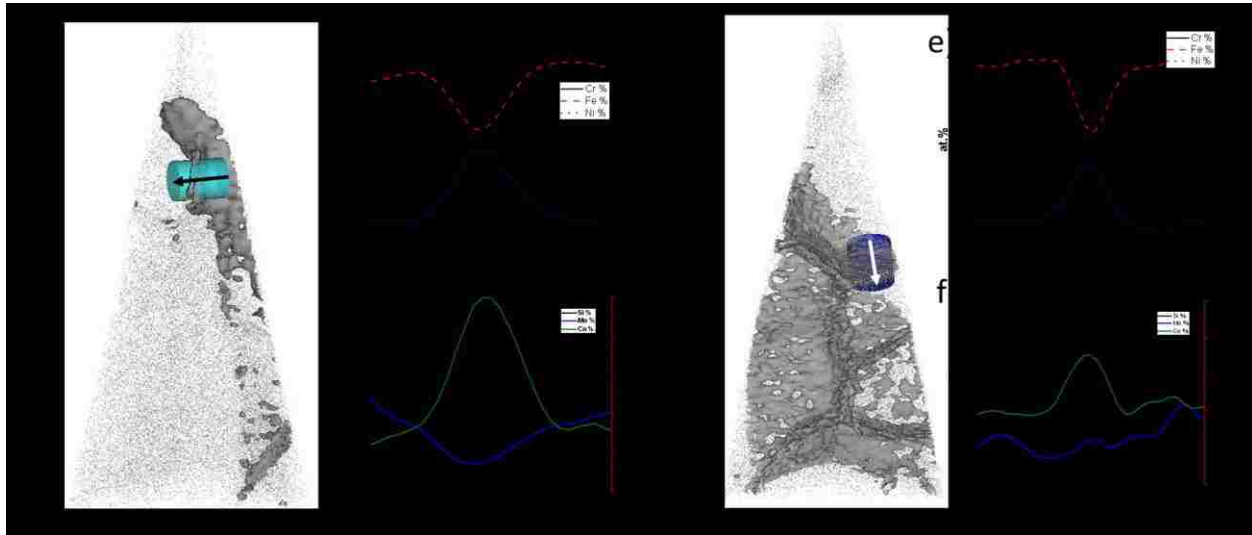


Figure 2. APT reconstruction of irradiated HPT304 showing Si atoms (grey) and 4 at.% Si isosurface to highlight grain boundaries; mostly only one UFG was observed; b) and c) 1-D concentration profiles across the ROI are in a) showing typical RIS behavior with enrichment in Ni, Si, Ti, and Co and depletion in Fe, Cr, and Mo; d) Another APT reconstruction of irradiated HPT304 showing Si atoms (grey) and 2 at.% Si isosurface to highlight grain boundaries; primarily, only NC grains were observed; e) and f) 1-D concentration profiles across the ROI shown in d); RIS was reduced in the NC grains, as compared to those in the UFG.

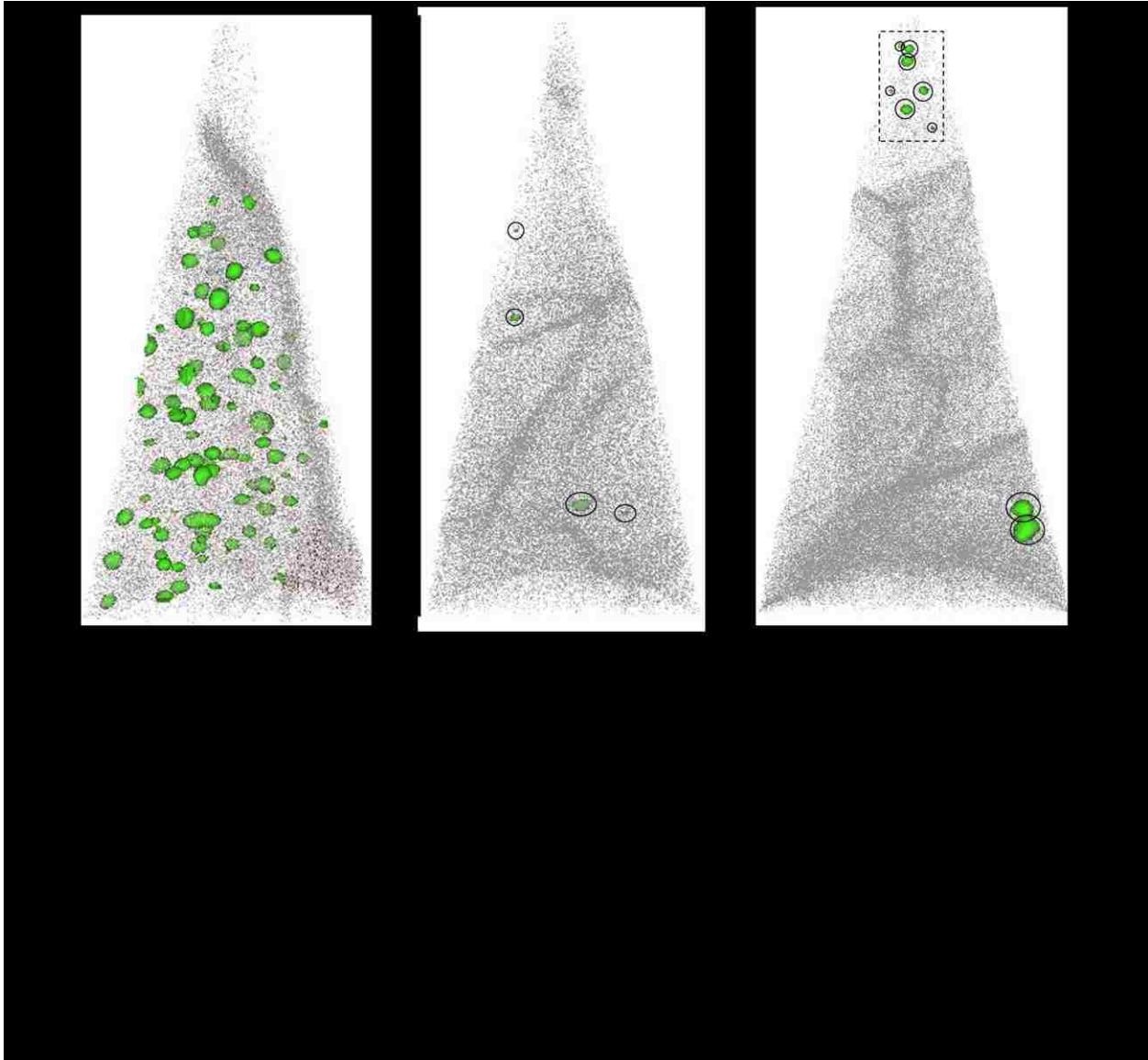


Figure 3. a), b), and c) APT reconstructions of irradiated HPT304 showing Si atoms (grey) and 5 at.% Cu isosurfaces (green) showing precipitation of Cu clusters. UFG in a) shows significant intragranular Cu precipitation while NC grains in b) and c) show little to no Cu precipitation. d) Proxigram based on all 5 at.% Cu isosurfaces in a). e) Proxigram based on all 5 at.% Cu isosurfaces in the boxed region of c).

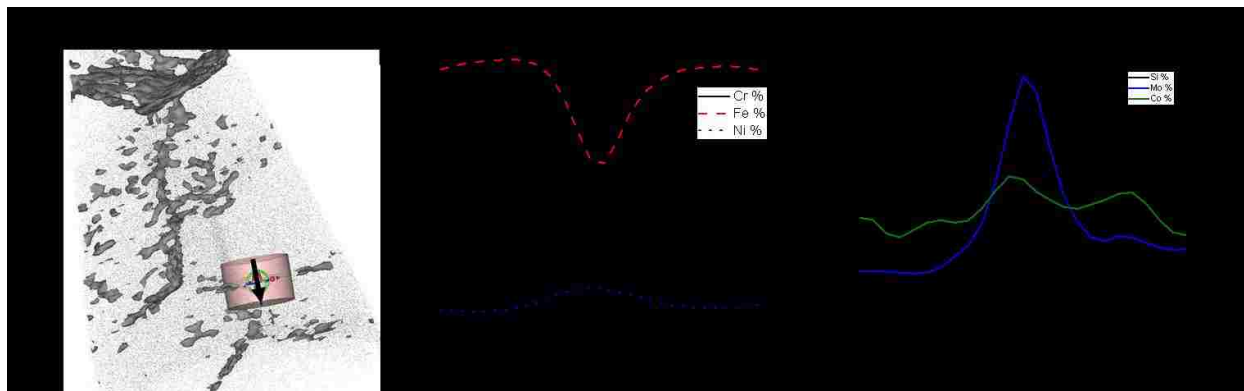


Figure 4. a) APT reconstruction of irradiated HPT 304 with Si atoms (grey) and 4 at.% Si isosurfaces to highlight GBs; b) and c) 1-D concentration profiles across ROI, in a) showing enrichment of Cr and Mo and no enrichment of Co.

REFERENCES

- [1] A.J. Ardell, P. Bellon, *Curr. Opin. Solid State Mater. Sci.* 20 (2016) 115–139.
- [2] T.R. Allen, *J. Nucl. Mater.* (1998) 44–58.
- [3] M. Nastar, F. Soisson, *Radiation-Induced Segregation*, Elsevier Inc., 2012.
- [4] G.S. Was, P.L. Andresen, *Corrosion* 63 (2007) 19–45.
- [5] S.J. Zinkle, *Advanced Irradiation-Resistant Materials for Generation IV Nuclear Reactors*, Elsevier Ltd, 2016.
- [6] A.P. Zhilyaev, T.G. Langdon, *Prog. Mater. Sci.* 53 (2008) 893–979.
- [7] M. Furukawa, Z. Horita, M. Nemoto, T.G. Langdon, *J. Mater. Sci.* 36 (2001) 2835–2843.
- [8] R.Z. Valiev, R. Islamgaliev, I.V. Alexandrov, *Prog. Mater. Sci.* 45 (2000) 103–189.
- [9] C. Sun, S. Zheng, C.C. Wei, Y. Wu, L. Shao, Y. Yang, K.T. Hartwig, S.A. Maloy, S.J. Zinkle, T.R. Allen, H. Wang, X. Zhang, *Sci. Rep.* 5 (2015) 1–7.
- [10] P.B.R. Rajan, I. Monnet, E. Hug, a Etienne, N. Enikeev, C. Keller, X. Sauvage, R. Valiev, B. Radiguet, *IOP Conf. Ser. Mater. Sci. Eng.* 63 (2014) 012121.

- [11] E. Hug, R. Prasath Babu, I. Monnet, A. Etienne, F. Moisy, V. Pralong, N. Enikeev, M. Abramova, X. Sauvage, B. Radiguet, *Appl. Surf. Sci.* 392 (2017) 1026–1035.
- [12] T. Toyama, Y. Nozawa, W. Van Renterghem, Y. Matsukawa, M. Hatakeyama, Y. Nagai, A. Al Mazouzi, S. Van Dyck, *J. Nucl. Mater.* 425 (2012) 71–75.
- [13] E.A. Kenik, T. Inazumi, G.E.C. Bell, *J. Nucl. Mater.* 183 (1991) 145–153.
- [14] D.L. Porter, *J. Nucl. Mater.* 79 (1979) 406–411.
- [15] T.R. Allen, G.S. Was, *Acta Mater.* 46 (1998) 3679–3691.
- [16] B. Radiguet, A. Etienne, P. Pareige, X. Sauvage, R. Valiev, *J. Mater. Sci.* 43 (2008) 7338–7343.
- [17] A. Etienne, B. Radiguet, N.J. Cunningham, G.R. Odette, R. Valiev, P. Pareige, *Ultramicroscopy* 111 (2011) 659–663.
- [18] A. Hoffman, H. Wen, R. Islamgaliev, R. Valiev, *Mater. Lett.* 243 (2019) 116–119.
- [19] M.M. Abramova, N.A. Enikeev, R.Z. Valiev, A. Etienne, B. Radiguet, Y. Ivanisenko, X. Sauvage, *Mater. Lett.* 136 (2014) 349–352.
- [20] I. Shuro, H.H. Kuo, T. Sasaki, K. Hono, Y. Todaka, M. Umemoto, *Mater. Sci. Eng. A* 552 (2012) 194–198.
- [21] I. Shuro, H.H. Kuo, Y. Todaka, M. Umemoto, *J. Mater. Sci.* 47 (2012) 8128–8133.
- [22] G. Was, T. Allen, E. Kenik, R. Dropek, J. Cole, in: *Eff. Radiat. Mater. 21st Int. Symp.*, 2008, pp. 540-540–13.
- [23] W. Mohamed, B. Miller, D. Porter, K. Murty, *Materials (Basel)*. 9 (2016) 1–23.
- [24] K. Lindgren, M. Boåsen, K. Stiller, P. Efsing, M. Thuvander, *J. Nucl. Mater.* 488 (2017) 222–230.
- [25] Z. Jiao, G.S. Was, *Acta Mater.* 59 (2011) 1220–1238.
- [26] J.J. Kai, F.R. Chen, T.S. Duh, *Mater. Trans.* 45 (2004) 40–50.
- [27] Z. Jiao, G.S. Was, *J. Nucl. Mater.* 449 (2014) 200–206.
- [28] L. Tan, J.T. Busby, *J. Nucl. Mater.* 443 (2013) 351–358.

- [29] Z. Jiao, J. Hesterberg, G.S. Was, *J. Nucl. Mater.* 500 (2018) 220–234.
- [30] H. Matsuoka, T. Yamasaki, Y.J. Zheng, T. Mitamura, M. Terasawa, T. Fukami, *Mater. Sci. Eng. A* 449–451 (2007) 790–793.

ENHANCING RESISTANCE TO IRRADIATION INDUCED FERRITIC TRANSFORMATION THROUGH NANO-STRUCTURING OF AUSTENITIC STEELS

Andrew Hoffman¹, Maalavan Arivu², Haiming Wen^{1,2,*}, Rinat Islamgaliev³, Ruslan Valiev³, Li He⁴, Kumar Sridharan⁴, Yongfeng Zhang⁴, Xin Wang⁵, Wei Xiong⁵, Xiang Liu⁶, Lingfeng He⁶

¹Department of Mining and Nuclear Engineering, Missouri University of Science and Technology, Rolla, MO 65409, USA

²Department of Materials Science and Engineering, Missouri University of Science and Technology, Rolla, MO 65409, USA

³Institute of Physics of Advanced Materials, Ufa State Aviation Technical University, Ufa 450008, Russia

⁴Department of Engineering Physics, University of Wisconsin, Madison, WI 53706

⁵Department of Mechanical Engineering and Materials Science, University of Pittsburgh, Pittsburgh, PA 15261, USA

⁶Idaho National Laboratory, Idaho Falls, ID 83415, USA

*Corresponding author: wenha@mst.edu; Tel.: +1-573-341-6167

ABSTRACT

Irradiation induced phase transformation of γ -austenite to α -ferrite has been observed in austenitic steels for the past several decades. This transformation can be detrimental to structural materials in a nuclear reactor environment as the increased fraction of the ferritic phase can cause increased corrosion, embrittlement, and lead to stress corrosion cracking. This transformation is caused by both strain induced martensite transformation as well as radiation induced segregation and precipitation. In this study, two radiation tolerant nanostructured 304 austenitic steels (one ultrafine grained and one

nanocrystalline) were manufactured using severe plastic deformation. These nanostructured 304 steels were compared to conventional coarse-grained 304 after self-ion irradiation at 500 °C up to a peak damage of 50 displacements per atom. Through grazing incidence x-ray diffraction, precession electron diffraction, and electron backscatter diffraction, phase fraction after irradiation was compared. Nanostructured 304 steels showed significant resistance to irradiation induced austenite to ferrite transformation. This resistance was shown to be due to both reduced defect structure formation as well as a reduction in radiation induced segregation and precipitation.

1. INTRODUCTION

In a nuclear reactor environment, structural materials are subjected to a variety of severe conditions including high temperatures and radiation fluences. Radiation damage results from neutrons colliding atoms introducing Frenkel pairs of vacancies and interstitials [1]. Over time these defects lead to the formation of dislocation loops and voids, precipitation, and grain boundary (GB) segregation [2]. These effects lead to embrittlement, swelling, and stress corrosion cracking (SCC) [3,4]. Phase instabilities are also a concern, and particularly for austenitic steels, the transformation of γ -austenite to α -ferrite in austenitic steels during irradiation has widely observed in a variety of grades including 304, 316, and 321 [5–7]. While the formation of ferrite in austenite during irradiation can contribute to an increase in volume/swelling [3], the formation of ferrite may contribute to a reduction in ductility [7], and (compared to austenite) ferrite has poor corrosion properties [8] which when combined can lead to additional SCC. It is therefore

important to develop austenitic steels which can resist this ferritic transformation in a radiation environment.

While the effects of radiation cannot be avoided all together, many new methods are being developed to enhance the radiation tolerance of nuclear structural materials. Among these are the development of new alloys such as high entropy alloys [9–12] and the development of nanostructured metals [13,14]. Nanostructured metals are designed to enhance radiation resistance through increased volume fraction of defect sinks. This can be achieved by the addition of nanoprecipitates or phase interfaces as is the case with oxide dispersion strengthened steels [15] or by increasing the volume fraction of grain boundaries (GB) through grain refinement [16]. In this study we focus on the latter, and study the enhanced irradiation tolerance by utilizing GB as radiation induced defect sinks [17,18]. This grain refinement was achieved by using two severe plastic deformation (SPD) techniques: equal channel angular pressing (ECAP) and high pressure torsion (HPT) [19–21]. While HPT can produce much higher strain (and thus is more effective for grain refinement), ECAP has the advantage of being commercially scalable [22]. In this study nanocrystalline (NC) 304 steel was produced using HPT and ultrafine grained (UFG) 304 steel was produced using ECAP.

Previous work on nanostructure steels has shown that they have good resistance to irradiation induced embrittlement and swelling [23–28]. In our previous study, we also showed that nanostructured 304 has good resistance to radiation induced segregation (RIS). This agrees with other limited studies showing a decrease in RIS with decreasing grain size [27,29]. No work, however, has been done on the investigation of enhancing austenite stability during irradiation of nanostructured austenitic steels. Boothby and

Williams did show that an increase in austenite stability during irradiation was associated with an increase in cold work of 12Cr-15Ni austenitic steels under neutron irradiation [30]. Gussev and collaborators, however, found the opposite effect in 304 steel where an increase in cold work is correlated with increased ferrite during irradiation of 304 steel at 320 °C, however this was for grain sizes of 20 microns or larger [31]. Hence, more work is needed in order to determine the effects of residual strain and grain size on the resistance of austenitic steels to the radiation induced ferritic transformation. This is the first study to report the austenite stability under irradiation of UFG and NC austenitic steel.

2. EXPERIMENTAL

Before SPD, commercial 304 barstock was homogenized at 1050 °C and water quenched. Refer to our previous study for composition. ECAP rods were processed using a 120 degree die at 450 °C for 6 passes using a B_c route. HPT discs were prepared using 6 GPa of pressure at 300°C and samples were rotated for 10 turns. Before irradiation, samples were mechanically polished up to a final step using 0.02µm colloidal silica solution. Ion irradiation was performed at the University of Wisconsin Ion Beam Laboratory. Samples were irradiated using a raster beam of 3.7 MeV Fe²⁺ ions up to a maximum damage of 50 displacements per atom (dpa). Grazing incidence x-ray diffraction (GIXRD) was performed using a Panalytical X'PERT materials research diffractometer (MRD). Electron backscatter diffraction (EBSD) and energy dispersive spectroscopy (EDS) was performed on a FEI HELIOS scanning electron microscope

(SEM) with an Oxford HKL EBSD detector. Transmission electron microscope (TEM) lamellas were prepared on using a focused ion beam (FIB) liftout using a FEI HELIOS SEM. Precession electron diffraction (PED) was performed using a TopSpin ASTAR system on a Technai F30 TEM. TEM was performed using a Technai F20 TEM.

3. RESULTS

3.1. EFFECT OF GRAIN SIZE ON IRRADIATION INDUCED PHASE CHANGE

Figure 1a-c show the grazing incidence XRD (irradiated region) and gonio scan (unirradiated bulk region) XRD results for the CG, ECAP, and HPT 304. In all the GIXRD scans, there is a significant α -110 peak which is not readily observed in the gonio XRD scans of the bulk sample. There is a small α -110 with very low intensity observed in the gonio scans which could be attributed to either contribution from the irradiated surface layer, or from thermal effects. Figure 1d shows XRD for CG, ECAP, and HPT 304 after annealing at 500 °C for 24 hrs. Annealing the CG and HPT 304 samples at 500 °C does induce the formation of α -110 peak, but no α -ferrite peaks are observed in the ECAP 304 sample after annealing. It should be noted that there was a small amount of α -ferrite seen in the CG 304 after homogenization and quenching [32], but the α -110 peak does increase after annealing at 500 °C.

In order to confirm the results obtained from XRD, phase analysis using PED was performed. Figure 2 shows PED maps of CG, ECAP, and HPT samples in which area fraction BCC was estimated to be 33%, 6.5%, and 2% respectively. While PED is a useful technique for the nanostructured materials, for the CG samples the statistics are not

good as the irradiated portion of TEM lamellas cannot cover many grains. The area fraction of BCC therefore may be overestimated from PED of the CG samples. EBSD (seen in Figure 3a) was therefore performed on the irradiated CG 304 specimen which showed 18% area fraction of BCC respectively which correlates well to those results obtained from XRD. It is noted that this EBSD does suffer from being a surface technique, and therefore the BCC fraction observed from EBSD likely is underestimated as the damage on the surface is ~15 dpa (see supplemental Figure 1).

3.2. CHEMICAL SEGREGATION BEHAVIOR

Figure. 3b and c show EDS maps of Ni and Cr in the EBSD scan shown in Figure 3a. While there is significant segregation observed for many of the α -ferrite regions which are enriched in Cr and depleted in Ni, not all α -ferrite grains exhibit this segregation behavior. This same behavior was observed from TEM and PED results as the α -ferrite grain from Figure 2a labeled “Cr-enriched, Ni-depleted” exhibited this same segregation behavior, however the ferritic grain on the left of Figure 2a showed matrix chemical composition. The Cr-enriched (Ni-depleted) ferritic grains also showed intragranular segregation. Figure 4a shows STEM bright field (BF) of the Cr-enriched ferritic grain shown in Figure 2a. Several intragranular precipitates can be seen from the chemical maps in Figure 4b-d including Ni enriched silicides, Cu precipitates, and $M_{23}C_6$ Cr enriched carbides. The Cu and Ni enriched precipitates appear to co-precipitate. It should be noted that these are actual precipitates rather than loops with Ni segregation as there is no loops structure that could be observed from TEM. The formation of these precipitates being initiated by segregation to loops, however, is a likely possibility as it is

a common phenomenon observed in 300 series austenitic steels. In contrast, within the ECAP and HPT 304 samples, no significant intragranular precipitation was observed. In our previous study, we did observe Cu precipitates within UFG in the HPT 304 sample, and limited Cu precipitation within the NC grains. Nevertheless, no intragranular segregation or precipitation of Ni, Cr, or C was observed. In both the ECAP and HPT 304 samples there was precipitation of Ni-Ti-Si g-phase, but this precipitation was intergranular, and precipitation within the ferritic grains was not observed, though many of the ferritic grains showed enrichment of Cr and depletion of Ni.

3.3. IRRADIATION INDUCED DEFECT STRUCTURES

In addition to differences in phase and chemical segregation, there were also clear differences in deformation behavior between CG, ECAP, and HPT 304. Figure 5 shows the formation of loops and defect cluster in CG, ECAP, and HPT 304. Within the CG 304, many larger loops with an average size of 33 ± 10 nm were found with an estimated loop density of $1.8 \times 10^{21} \text{ m}^{-3}$. When compared to ECAP 304, the average loop size is significantly decreased with an average size of 6 ± 3 nm, but the estimated loop density increases to $1.2 \times 10^{22} \text{ m}^{-3}$. This is indicative of reduced damage as these dislocation loops have not agglomerated and coarsened. In the HPT 304, no dislocation loops were observed, but as can be seen from Figure 5c there are many “black spot” features within some of the ultrafine grains indicative of the formation of defect clusters which have not yet formed loops. Within the small NC grains in HPT 304, however, these defect clusters are not observed.

Larger dislocation structures also differ significantly with grain size. Figure 6a shows TEM dark field (DF) of CG 304 which shows the formation of a large dislocation network after irradiation. This dislocation network can be seen more readily from TEM BF shown in Figure 6b in which the irradiated region with dislocation networks is visible as compared to the unirradiated region. The unirradiated region has many dislocations and dislocation tangles from quenching but no networks are readily observed. Figure 6c shows TEM BF of the irradiated region and Figure 6d shows TEM BF of the unirradiated region in ECAP 304. It is difficult to distinguish between the irradiated and unirradiated regions in the ECAP 304 sample, as the as ECAPed condition consists of a microstructure which has a high dislocation density and many dislocation tangles and cells which is typical in SPD materials especially in the early-mid stages of grain refinement. While the dislocation microstructure of the as ECAPed sample makes it difficult to compare to the irradiated region, it can be concluded that unlike what was observed in the CG 304 sample, the ECAP 304 sample does not form new large irradiation induced dislocation networks.

The microstructure of irradiated HPT 304 shows a few interesting features. As can be seen from Figure 6e there is significant irradiation induced grain growth as was previously reported in our study of segregation within the irradiated HPT 304 sample. This irradiation induced grain growth was also previously reported in other nanostructured metals under both ion irradiated austenitic steel and neutron irradiated Cu [33,34]. Figure 6f shows TEM BF of HPT 304 annealed at 500°C showing no grain growth, and even limited recovery due to thermal effects which can also be seen from Figure 6e in the unirradiated region. After irradiation, there are still many dislocations

observed in many of the grains as can be seen from the diffraction contrast in Figure 6e. The grains in the irradiated region have less observed strain as compared to the unirradiated grains, and some of the UFG within the irradiated region are defect free as can be seen from the misorientation map in Figure 2a. Therefore, this growth mechanism, while undesired, may contribute to the prevention of strain accumulation during irradiation.

3.4. RADIATION INDUCED SEGREGATION

In our previous study, we showed the behavior of grain size on the RIS within HPT 304. In this study, through APT, it was observed that when comparing RIS in ultrafine grains compared to NC grains the segregation behavior is significantly decreased with a decrease in grain size. The difference in segregation for Cr depletion and Ni and Si enrichment was 3.4 at.% Cr, 8.5 at.% Ni, and 1.5 at.% Si respectively. There were several NC grains in which the GBs were also observed to have Cr enrichment with minimal Ni enrichment. This Cr enrichment was accompanied with enrichment in Mo. Both Cr and Mo were observed to be enriched along GBs in HPT 304 after annealing at 500 °C for 24hrs. Co which was found to be enriched along other irradiated GBs was not found in the Cr enriched GBs. This, therefore, demonstrates that the observed Cr enriched GBs showed enrichment of other species typically associated with GB segregation after thermal annealing, and limited enrichment of species associated with RIS. It was concluded that small grain size can reduce the impact of the kinetically driven segregation, and, especially in the case of nanocrystalline materials, increase the impact of thermal annealing at irradiation temperatures.

4. MODELING AND DISCUSSION

4.1. THERMAL EFFECTS OF PHASE TRANSFORMATION

As can be seen from Figure 1d, there is a clear transformation of the CG and HPT 304 during annealing at 500 °C for 24hrs. While the Ni content in Fe-Cr-Ni alloys can stabilize the austenitic phase, the stability of austenite decreases with temperature. In order to more fully understand the temperature dependence of austenite stability of this 304 composition CALPHAD (CALculation of PHase Diagrams) was utilized. Figure 7 shows the phase fraction vs temperature for the 304 presently studied. The stability of austenite steadily decreases below 600 °C which agrees with the XRD results of CG and HPT 304 in Figure 1d. The ECAP 304 sample, however, shows good thermal stability under annealing which could be due to the high fraction of low angle grain boundaries when compared to the CG and HPT 304 samples. This thermal instability does not account for the ferritic transformation during irradiation. As can be seen from the comparison of gonio XRD scans and GIXRD, the amount of ferrite within the irradiated region in all three 304 samples is significantly higher than in the bulk.

Previous studies also show that the radiation induced austenite to ferrite transformation in austenitic steels is not simply irradiation assisted transformation towards equilibrium. Keefer et. al showed that proton irradiated 321 steel showed more ferrite transformation at 500 °C than was observed at 400 °C [35]. Porter and Wood observed a similar trend when neutron irradiated 304 and 316 at temperatures between 400 and 550 °C, and they found that fast neutron irradiation at 400 °C resulted in no observable ferrite [5,36]. This behavior appeared counterintuitive as the stability of

austenite steadily declines with a decrease in temperature. It was therefore concluded that rather than a radiation assisted thermal transformation, this is a kinetically driven irradiation induced transformation.

4.2. $\gamma \rightarrow \alpha$ TRANSFORMATION MECHANISM

Because the explanation of the austenite to ferrite transformation could not be explained by irradiation assisted thermal transformation, there can be two kinetically driven explanations: transformation driven by RIS which can cause depletion of Ni within the matrix (consequently decreasing austenite stability) and a deformation induced martensite transformation (DIMIT) caused by irradiation induced defect formation and strain. When Keefer and colleagues first observed this phenomenon, they attributed it to the increase in vacancies allowing for enhanced diffusion which drives the phase transformation [35]. Porter and Wood observed the formation of austenite rings surrounding voids in the material, and that ferritic grains tend to nucleate within faulted loop structures [5,36]. While Porter and Wood do claim that these effects are influenced by RIS, the cause is likely more complex than being explained simply by segregation and precipitation as is commonly cited in more recent studies which observe irradiation induce ferrite[6,7].

Because nucleation tends to occur within faulted loops, this is likely driven by a two step martensite transformation which includes transformation from $\gamma \rightarrow \epsilon \rightarrow \alpha'$ where ϵ -martensite is an HCP structure and is responsible for the dual phase TRIP mechanism [37]. While the α' -martensite produced through this mechanism is a body centered tetragonal (BCT) structure, in low carbon steels the lack of interstitials will cause α' -

martensite to relax into a BCC α -ferrite structure. This DIMT is highly dependent on stacking fault energy (SFE) as nucleation of ϵ -martensite tends to occur on stacking faults[38]. Maksimkin discusses this relation of SFE to martensite transformation as he observed the formation of ϵ -martensite and α -ferrite after Kr ion irradiation at 400 °C of 12Cr18Ni10Ti austenitic steel [39]. This can also be related to the observation that the addition of Si and/or Ti will increase the amount of ferrite transformation during irradiation as both Si and Ti are known to decrease the SFE in austenitic steels [40–43]. Mn is also known to decrease SFE [40], and Gussev et. al also showed that Si and Mn have the largest impact on the ferritic transformation during irradiation of austenitic steels [31].

It should be noted, however, that the G-phase which is an irradiation induced intermetallic precipitate is a Ni silicide with a possible composition of Ni-Mn-Si or Ni-Ti-Si [5,44,45]. Ni_3Si γ' is another common irradiation induced precipitate [46–49]. Therefore, addition of Si, Mn, and Ti also will contribute to the formation of Ni enriched precipitates which will deplete the matrix of Ni and contribute to austenite instability. The formation of these Ni enriched phases in austenitic steels is primarily caused by RIS through the inverse Kirkendall effect (IKE) which is driven primarily by diffusion of vacancies towards defect sinks (grain boundaries and dislocations) [50]. As vacancies diffuse towards defect sinks, fast diffusing atoms will travel preferentially in the opposite direction of this vacancy flux. In austenitic steels, Cr is undersized and is a fast diffuser while Ni and Si are oversized and slow diffusers. This causes Cr to deplete and Ni and Si to enrich along grain boundaries and dislocations in Fe-Cr-Ni austenitic steels [51,52]. This results in depletion of Ni from the matrix, and a decrease in austenite stability. It is

reasonable, consequently, that both deformation induced transformation and segregation and precipitation will contribute to the phase ferritic transformation during irradiation.

4.3. GRAIN SIZE EFFECTS ON DEFORMATION INDUCED TRANSFORMATION

Previous studies indicated that cold worked steels tend to be more resistant to irradiation induced ferrite transformation [5,30]. Nevertheless, it was not fully understood as to why the cold work increased the stability of austenite. The reduction of irradiation induced ferrite due to DIMT correlated to reduction of grain size can be compared to the resistance to DIMT during plastic deformation with a decrease in grain size. Yoo et. al showed that the critical stored energy required for deformation induced martensite transformation in Fe-Ni-Cr-Mn austenitic steels increases with a reduction in grain size [53]. This is confirmed by other studies which have shown that a decrease in grain size is associated with an increase in austenite stability during plastic deformation [8,54–56]. One major contributing factor to this is the increased GB volume fraction, as dislocation density will be decreased with a decrease in grain size because this increases the annihilation of dislocations at GBs [21,57–59]. This will, in turn, reduce the number of nucleation sites at which martensitic grains can nucleate.

Just as GB can act as sites for annihilation of dislocations accumulated during plastic deformation, GBs also act as sinks for irradiation induced defects [17]. This was observed to have two effects in the present study on ion irradiated 304. First, the size of loops is significantly decreased as the average loop size in ECAP 304 is ~6 nm as compared to CG 304 in which average loop size was ~33 nm making for a difference in loop size of ~27 nm. When compared to the HPT 304, no loops were observable and only

defect clusters formed. This can be directly correlated to lower dislocation density and annihilation of defects at GBs preventing the coarsening of dislocation loops in the nanostructured 304 samples. Similarly, the formation of large dislocation structures is significantly reduced in the nanostructured 304 steels. As is observed from Figure 6a and b, CG 304 forms very large dislocation networks during irradiation which cover the entire irradiated region. This not only increases strain, but also the number of martensite nucleation sites. In contrast, the ECAP 304 microstructure does contain dislocation cells and tangles, but the microstructure is predominantly defined by the pre-irradiation microstructure obtained from SPD. The HPT 304 microstructure is relatively free of large dislocation structures, and the irradiation induced grain growth mechanism reduces strain within the material as there are many relatively defect free ultrafine grains after irradiation.

The nano-structuring of 304 can consequently reduce the irradiation induced martensite transformation in two ways. First, the size of faulted dislocation loops is reduced in ECAP 304 as compared to CG 304 and in HPT 304 faulted loops do not form. Maksimkin notes that it is speculated that irradiation induced martensite formation is related to irradiation induced faulted frank loops [39]. Reducing the size or preventing the formation of such loops will therefore eliminate one mechanism of martensite nucleation. Second, the prevention of the formation of large dislocation networks as is observed in the CG 304 can help prevent the creation of martensite “embryos” which form from stacking faults and deformation twins [60].

4.4. GRAIN SIZE EFFECTS ON RADIATION INDUCED SEGREGATION AND PRECIPITATION

In our previous study, it was reported that within the UFG and NC grains in ion irradiated HPT 304, no segregation or precipitation of Ni or Ni silicides was observed. This is in good agreement with previous studies of irradiated nanostructured 300 series steels [27,29,34]. In contrast, CG 304 shows the precipitation of Ni_3Si as can be seen from Figure 4. This formation of Ni_3Si is understood to be initiated by RIS which causes enrichment of Ni and Si along dislocation loops [46–49]. Because no dislocation loops could be found in the irradiated HPT 304 there are no intragranular sites on which this RIS can occur which eliminates the mechanism of precipitate formation. In the irradiated ECAP 304, although small, dislocation loops were still observed. However, no intragranular Ni segregation or Ni enriched precipitation was observed. This can be reasonably attributed to the reduction in RIS due to grain size effects.

Our previous study of irradiated HPT 304 also showed that RIS is reduced with decreasing grain size. This also agrees with other studies on nanostructured austenitic steels showing that nanostructuring is effective in reducing RIS [27,29]. This reduction in RIS can be understood by annihilation of defects at GBs. As GB size is decreased, the distance defects must travel to sinks is reduced which causes both the total defect density to decrease while also reducing the vacancy flux towards GBs and dislocations which is thought to be the primary driving mechanism for RIS [52,61]. This can therefore explain the lack of segregation and precipitation of Ni silicide on dislocation loops in the irradiated ECAP 304. Additionally, with increased RIS along GBs, Ni will become depleted within the matrix reducing austenite stability. Therefore, a reduction in GB

segregation in the ECAP and HPT 304 helps to maintain a homogeneous Ni content and reduce ferrite transformation due to chemical segregation.

5. CONCLUSIONS

304 austenitic steel with varying grain size was manufactured using two SPD techniques: ECAP and HPT. The nanostructured steels were compared to CG 304 after self-ion irradiation at 500 °C to a max damage of 50 dpa. The phase stability of austenite was compared, and the results are summarized as follows.

(1) Both XRD and PED show that nanostructured 304 steels are more resistant to irradiation induced ferritic transformation when compared to CG 304.

(2) The irradiation induced ferritic transformation is caused by two mechanisms. The first is deformation induced martensite transformation which is a diffusionless transformation caused by irradiation induced strain, and results in BCC grains with matrix chemical composition. The second is irradiation induced segregation and precipitation of Ni and Ni enriched precipitates which causes the depletion of Ni within the matrix thus decreasing austenite stability.

(3) Nano-structuring results in a decrease in irradiation induced defects. The ECAP 304 showed reduced dislocation loop size as compared to CG 304. No loops were found in HPT 304, and only defect clusters were observed. CG 304 formed large dislocation networks after irradiation whereas ECAP 304 and HPT 304 did not form large irradiation induced defect structures.

(4) RIS is significantly reduced with a decrease in grain size due to a reduced vacancy flux towards defect sinks.

(5) The enhanced resistance to irradiation induced ferritic transformation in nanostructured 304 is due to a reduction in irradiation induced defects and RIS. Because of annihilation of defects at GBs in nanostructured steels, loop size is either decreased or loops are prevented from forming altogether. The prevention of large loop formation and large dislocation structures prevents the formation of and dislocation interaction with stacking faults and twins reducing the DIMT. A reduction in RIS and precipitation of Ni enriched phases prevents Ni depletion enhancing austenite stability.

ACKNOWLEDGMENTS

This research was financially supported by the U.S. Department of Energy, Office of Nuclear Energy through the NEET-NSUF (Nuclear Energy Enabling Technology - Nuclear Science User Facility) program (award number DE-NE0008524), and through the NSUF-RTE program (award number 17-865). Partial support for Andrew Hoffman came from the U.S. Nuclear Regulatory Commission Faculty Development Program (award number NRC 31310018M0044). RZV gratefully acknowledge the financial support from Saint Petersburg State University in the framework of Call 3 project (id 26130576). Nathan Curtis, Victor DeLibera, and Hans Pommerenke are thanked for their assistance in sample preparation. APT and PED work was performed at the Center for Advanced Energy Studies (CAES), and Dr. Yaqiao Wu is thanked for his assistance.

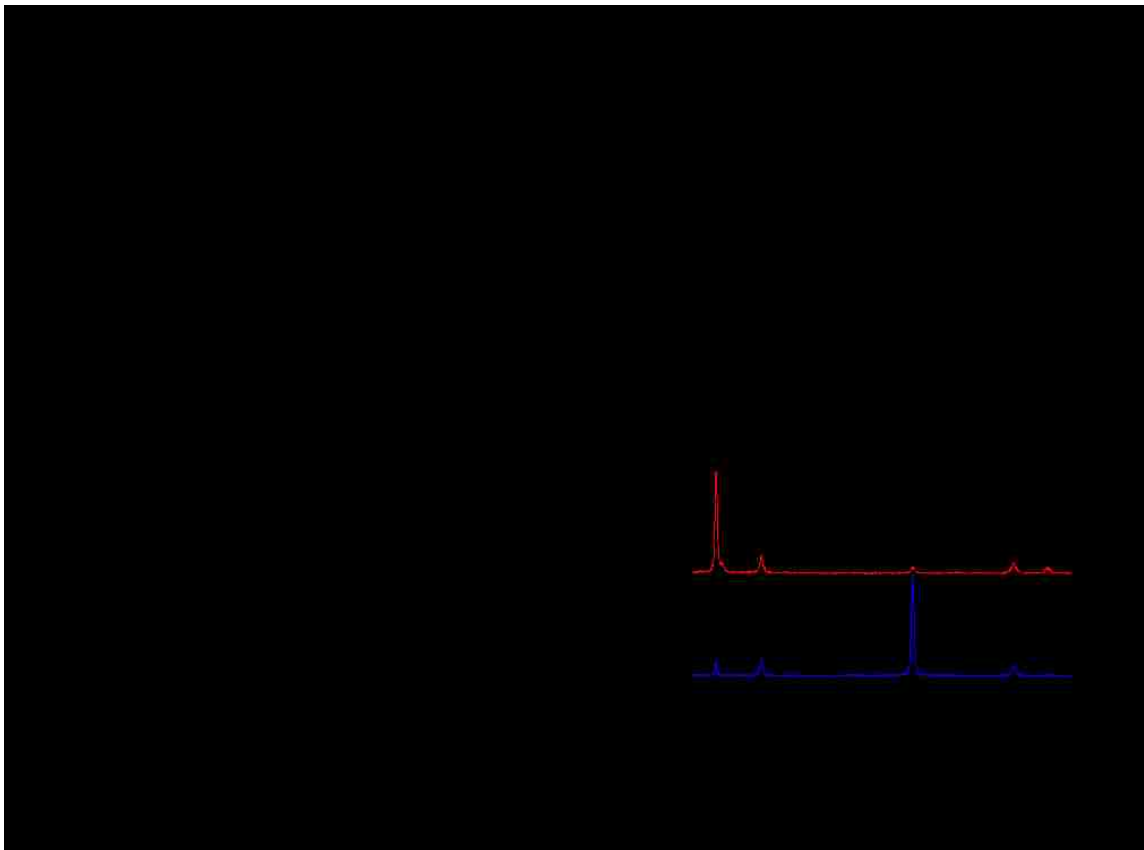


Figure 1. a-c) Low angle XRD and gonio scans showing the ion irradiated thin film region and non-irradiated bulk of the CG, ECAP, and HPT 304. A significant amount of α -ferrite is seen after irradiation in all samples as seen from the α -110 reflection. d) XRD of CG, ECAP, and HPT 304 after annealing at 500 °C for 24 hrs.

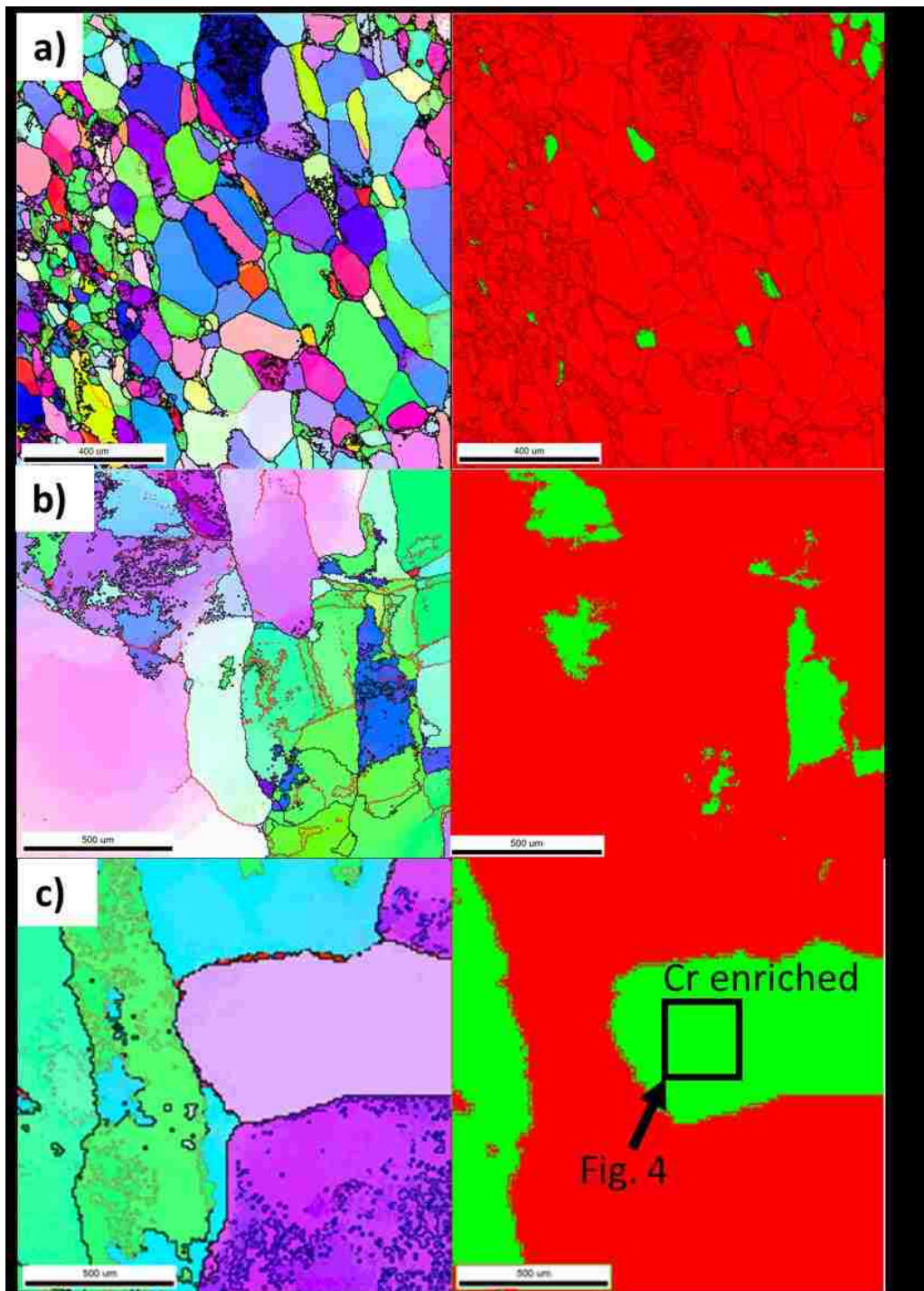


Figure 2. PED misorientation maps (left) and phase maps (right) showing γ -austenite (red) and α -ferrite (green) for a) HPT, b) ECAP, and c) CG 304 ion irradiated at 500 °C.

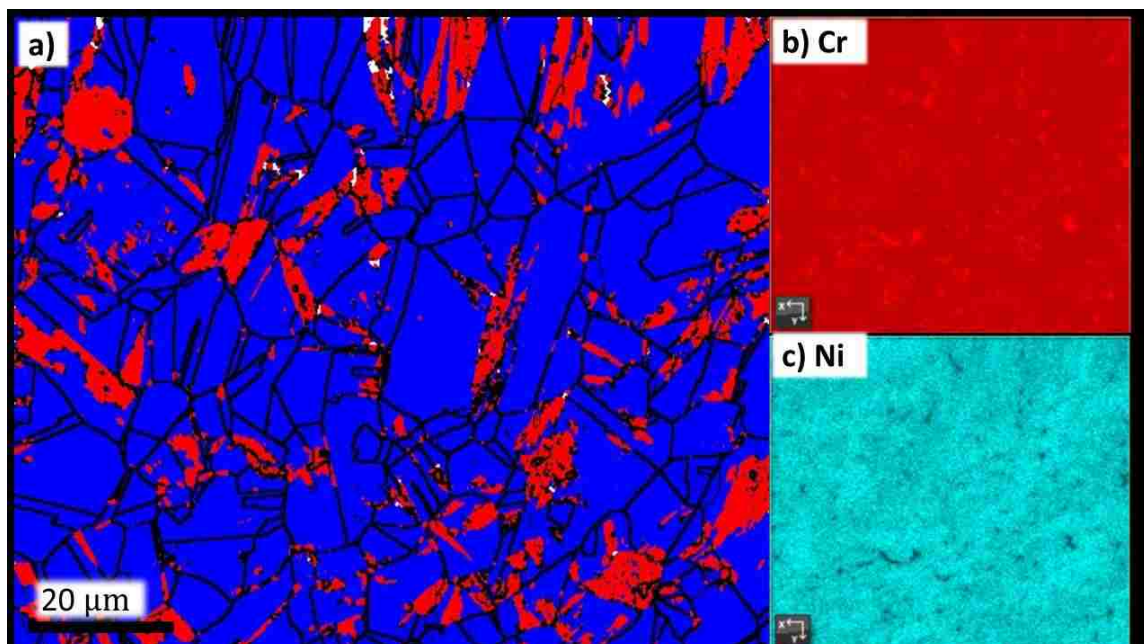


Figure 3. a) EBSD phase map showing austenite (blue) and ferrite (red). EDS chemical maps of the map in a) are shown for b) Cr and c) Ni. Not all ferritic regions are depleted in Ni and enriched in Cr.

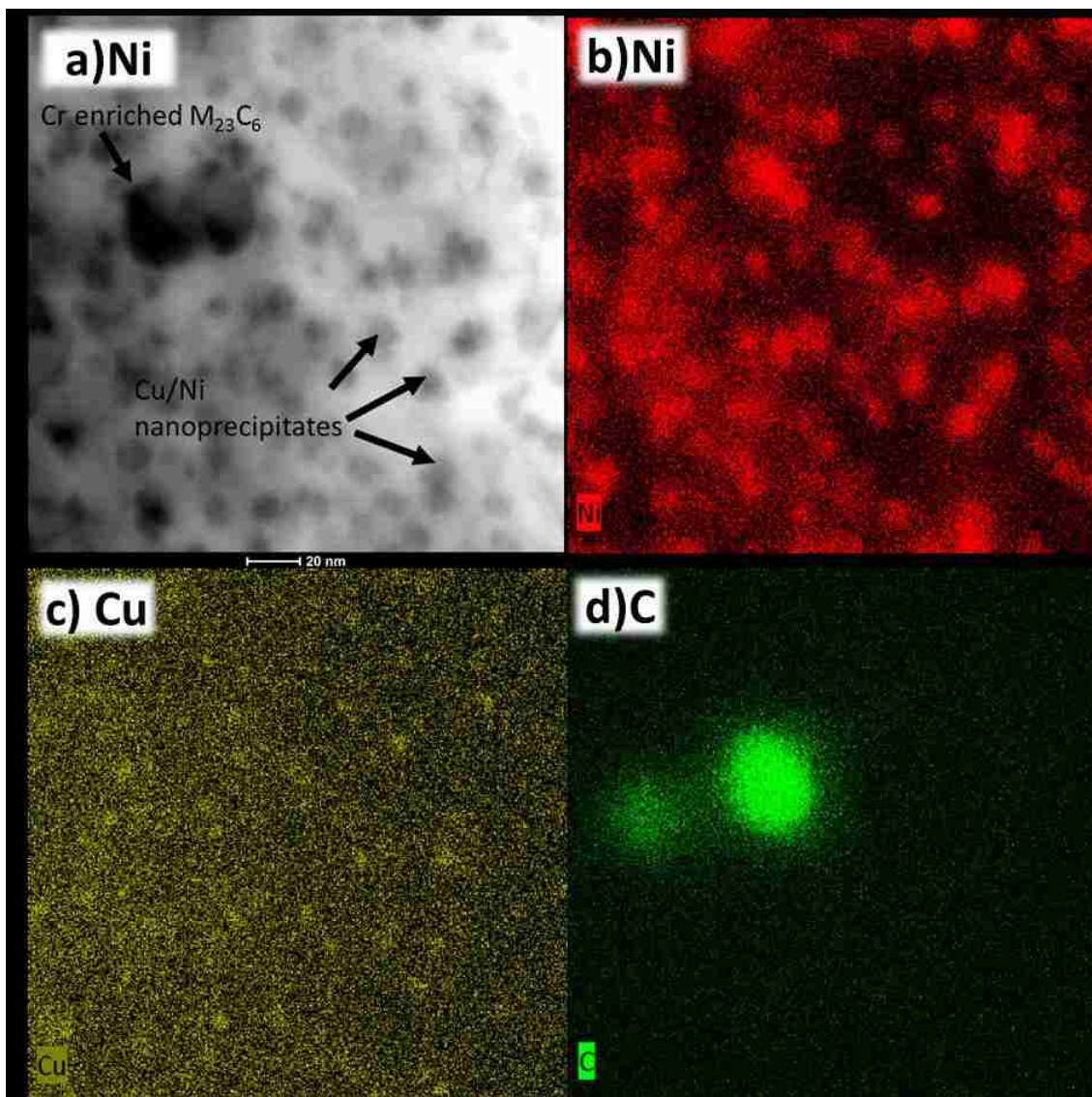


Figure 4. a) STEM BF and b)-d) associated EDS chemical maps of ion irradiated CG 304 showing Ni-Si enriched, Cu, and Cr enriched $M_{23}C_6$ precipitates.

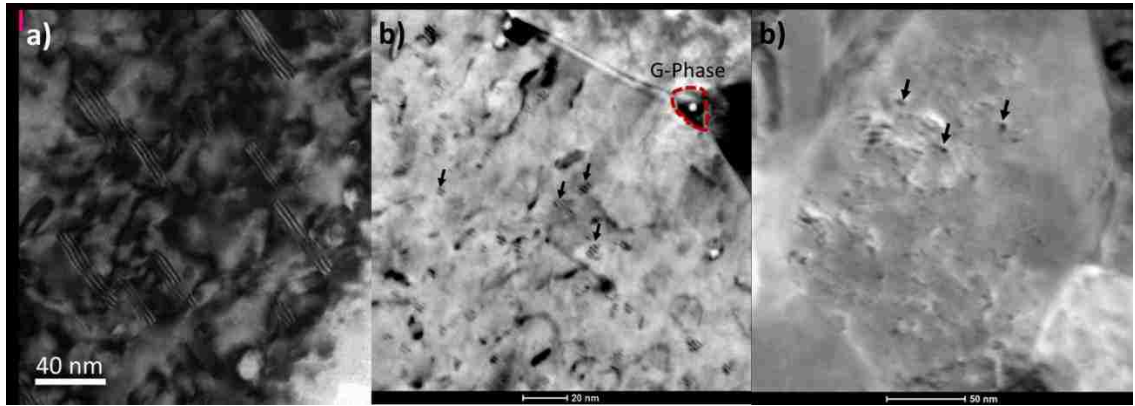


Figure 5. Micrographs of different grain sized 304 after ion irradiation. a) TEM BF of CG 304 showing large faulted loops. b) STEM BF of ECAP 304 showing many small faulted loops. c) STEM BF of HPT 304 showing many “black spot” defects indicating formation of defect clusters.

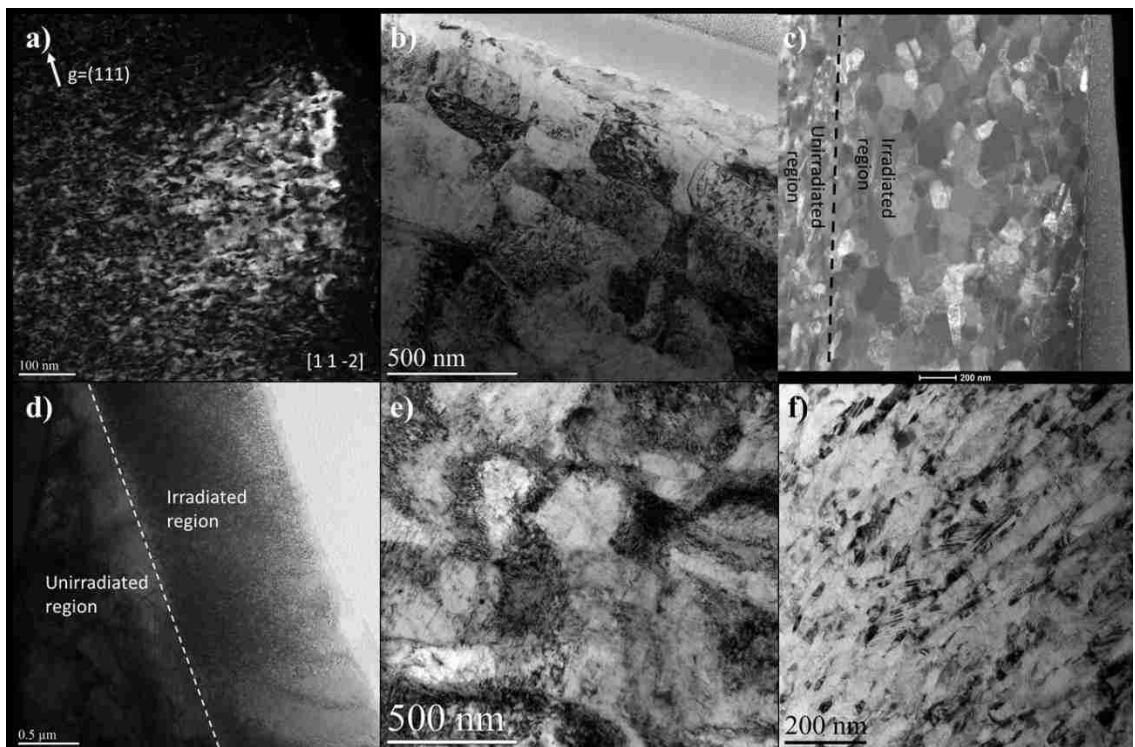


Figure 6. a) TEM DF and d) TEM BF of irradiated CG 304 showing the formation of large dislocation networks. b) TEM BF of irradiated and e) unirradiated ECAP 304 showing dislocation cells/tangles and little change in dislocation structures after irradiation. c) STEM DF of irradiated HPT 304 showing irradiation induced grain growth, but many defect free grains. f) TEM BF of HPT 304 annealed at 500 °C for 24 hrs showing no grain growth, and limited recovery.

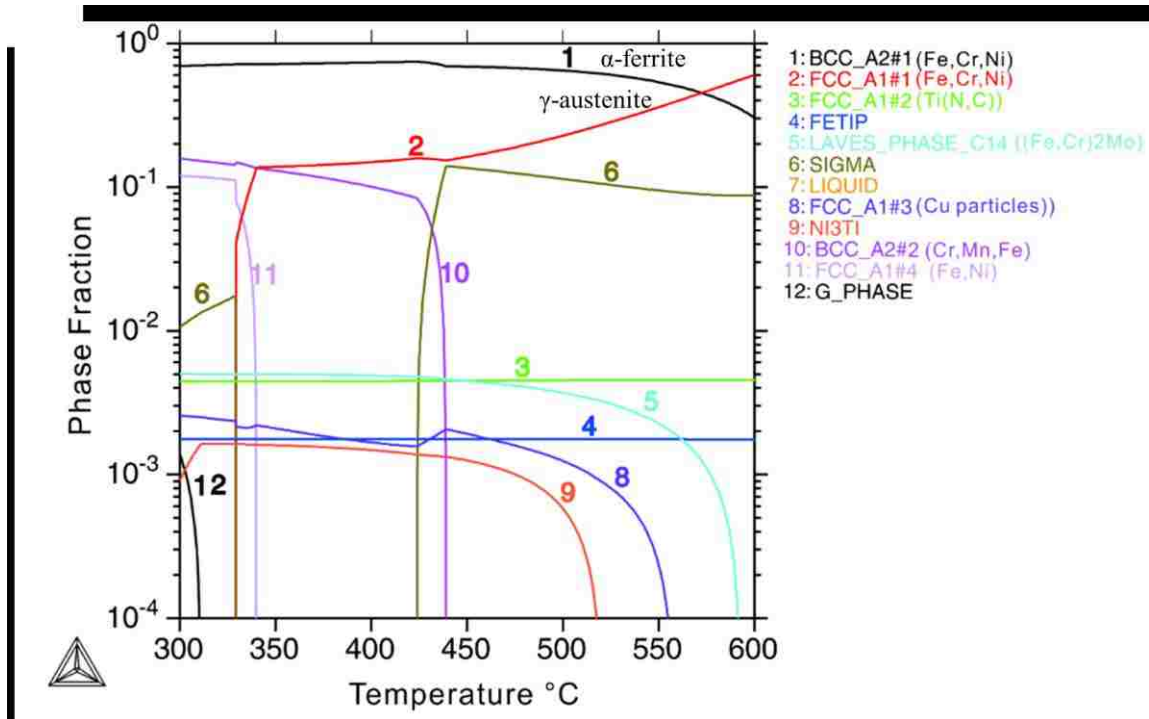


Figure 7. Phase fraction vs temperature of 304 steel composition in this study.

REFERENCES

- [1] A. Aitkaliyeva, L. He, H. Wen, B. Miller, X.M. Bai, T. Allen, Irradiation effects in Generation IV nuclear reactor materials, in: *Struct. Mater. Gener. IV Nucl. React.*, Elsevier, 2017: pp. 253–283. doi:10.1016/B978-0-08-100906-2.00007-0.
- [2] G.S. Was, *Fundamentals of radiation materials science: Metals and alloys*, second edition, 2016. doi:10.1007/978-1-4939-3438-6.
- [3] F.A. Garner, *Radiation damage in austenitic steels*, Elsevier Inc., 2012. doi:10.1016/B978-0-08-056033-5.00065-3.
- [4] G.S. Was, P.L. Andresen, Stress corrosion cracking behavior of alloys in aggressive nuclear reactor core environments, *Corrosion*. 63 (2007) 19–45. doi:10.5006/1.3278331.

- [5] D.L. Porter, E.L. Wood, In-reactor precipitation and ferritic transformation in neutron-irradiated stainless steels, *J. Nucl. Mater.* 83 (1979) 90–97. doi:10.1016/0022-3115(79)90595-6.
- [6] J.W. Liu, C.H. Tsai, J.J. Kai, Proton Irradiation Induced Phase Transformation in AISI 304L Stainless Steel, *Scr. Metallurgica Mater.* 30 (1994) 547–552.
- [7] B.K. Singh, V. Singh, Effect of fast neutron irradiation on tensile properties of AISI 304 stainless steel and alloy Ti-6Al-4V, *Mater. Sci. Eng. A.* 528 (2011) 5336–5340. doi:10.1016/j.msea.2011.03.066.
- [8] L. Jinlong, L. Hongyun, L. Tongxiang, G. Wenli, The effects of grain refinement and deformation on corrosion resistance of passive film formed on the surface of 304 stainless steels, *Mater. Res. Bull.* 70 (2015) 896–907. doi:10.1016/j.materresbull.2015.06.030.
- [9] T. Yang, S. Xia, S. Liu, C. Wang, S. Liu, Y. Fang, Y. Zhang, J. Xue, S. Yan, Y. Wang, Precipitation behavior of Al_xCoCrFeNi high entropy alloys under ion irradiation, *Sci. Rep.* 6 (2016) 1–8. doi:10.1038/srep32146.
- [10] T. Egami, W. Guo, P.D. Rack, T. Nagase, Irradiation resistance of multicomponent alloys, in: *Metall. Mater. Trans. A Phys. Metall. Mater. Sci.*, 2014: pp. 180–183. doi:10.1007/s11661-013-1994-2.
- [11] N.A.P.K. Kumar, C. Li, K.J. Leonard, H. Bei, S.J. Zinkle, Microstructural stability and mechanical behavior of FeNiMnCr high entropy alloy under ion irradiation, *Acta Mater.* 113 (2016) 230–244. doi:10.1016/j.actamat.2016.05.007.
- [12] W.Y. Chen, X. Liu, Y. Chen, J.W. Yeh, K.K. Tseng, K. Natesan, Irradiation effects in high entropy alloys and 316H stainless steel at 300 °C, *J. Nucl. Mater.* 510 (2018) 421–430. doi:10.1016/j.jnucmat.2018.08.031.
- [13] X. Zhang, K. Hattar, Y. Chen, L. Shao, J. Li, C. Sun, K. Yu, N. Li, M.L. Taheri, H. Wang, J. Wang, M. Nastasi, Radiation damage in nanostructured materials, *Prog. Mater. Sci.* 96 (2018) 217–321. doi:10.1016/j.pmatsci.2018.03.002.
- [14] S.J. Zinkle, *Advanced irradiation-resistant materials for Generation IV nuclear reactors*, Elsevier Ltd, 2016. doi:10.1016/B978-0-08-100906-2.00016-1.
- [15] G.R. Odette, M.J. Alinger, B.D. Wirth, Recent Developments in Irradiation-Resistant Steels, *Annu. Rev. Mater. Res.* 38 (2008) 471–503. doi:10.1146/annurev.matsci.38.060407.130315.
- [16] C.X. Huang, Y.L. Gao, G. Yang, S.D. Wu, G.Y. Li, S.X. Li, Bulk nanocrystalline stainless steel fabricated by equal channel angular pressing, *J. Mater. Res.* 21 (2006) 1687–1692. doi:10.1557/jmr.2006.0214.

- [17] C. Sun, M. Song, K.Y. Yu, Y. Chen, M. Kirk, M. Li, H. Wang, X. Zhang, In situ Evidence of defect cluster absorption by grain boundaries in Kr ion irradiated nanocrystalline ni, *Metall. Mater. Trans. A Phys. Metall. Mater. Sci.* 44 (2013) 1966–1974. doi:10.1007/s11661-013-1635-9.
- [18] T.D. Shen, Radiation tolerance in a nanostructure: Is smaller better?, *Nucl. Instruments Methods Phys. Res. Sect. B Beam Interact. with Mater. Atoms.* 266 (2008) 921–925. doi:10.1016/j.nimb.2008.01.039.
- [19] A.P. Zhilyaev, T.G. Langdon, Using high-pressure torsion for metal processing: Fundamentals and applications, *Prog. Mater. Sci.* 53 (2008) 893–979. doi:10.1016/j.pmatsci.2008.03.002.
- [20] M. Furukawa, Z. Horita, M. Nemoto, T.G. Langdon, Review: Processing of metals by equal-channel angular pressing, *J. Mater. Sci.* 36 (2001) 2835–2843. doi:10.1023/a:1017932417043.
- [21] R.Z. Valiev, R. Islamgaliev, I.V. Alexandrov, Bulk nanostructured materials from severe plastic deformation, *Prog. Mater. Sci.* 45 (2000) 103–189. doi:10.1016/S0079-6425(99)00007-9.
- [22] G.J. Raab, R.Z. Valiev, T.C. Lowe, Y.T. Zhu, Continuous processing of ultrafine grained Al by ECAP-Conform, *Mater. Sci. Eng. A.* 382 (2004) 30–34. doi:10.1016/j.msea.2004.04.021.
- [23] C. Sun, K.Y. Yu, J.H. Lee, Y. Liu, H. Wang, L. Shao, S.A. Maloy, K.T. Hartwig, X. Zhang, Enhanced radiation tolerance of ultrafine grained Fe-Cr-Ni alloy, *J. Nucl. Mater.* 420 (2012) 235–240. doi:10.1016/j.jnucmat.2011.10.001.
- [24] A. Alsabbagh, R.Z. Valiev, K.L. Murty, Influence of grain size on radiation effects in a low carbon steel, *J. Nucl. Mater.* 443 (2013) 302–310. doi:10.1016/j.jnucmat.2013.07.049.
- [25] M. Song, Y.D. Wu, D. Chen, X.M. Wang, C. Sun, K.Y. Yu, Y. Chen, L. Shao, Y. Yang, K.T. Hartwig, X. Zhang, Response of equal channel angular extrusion processed ultrafine-grained T91 steel subjected to high temperature heavy ion irradiation, *Acta Mater.* 74 (2014) 285–295. doi:10.1016/j.actamat.2014.04.034.
- [26] C. Sun, S. Zheng, C.C. Wei, Y. Wu, L. Shao, Y. Yang, K.T. Hartwig, S.A. Maloy, S.J. Zinkle, T.R. Allen, H. Wang, X. Zhang, Superior radiation-resistant nanoengineered austenitic 304L stainless steel for applications in extreme radiation environments, *Sci. Rep.* 5 (2015) 1–7. doi:10.1038/srep07801.

- [27] P.B.R. Rajan, I. Monnet, E. Hug, a Etienne, N. Enikeev, C. Keller, X. Sauvage, R. Valiev, B. Radiguet, Irradiation resistance of a nanostructured 316 austenitic stainless steel, *IOP Conf. Ser. Mater. Sci. Eng.* 63 (2014) 012121. doi:10.1088/1757-899X/63/1/012121.
- [28] E. Hug, R. Prasath Babu, I. Monnet, A. Etienne, F. Moisy, V. Pralong, N. Enikeev, M. Abramova, X. Sauvage, B. Radiguet, Impact of the nanostructuration on the corrosion resistance and hardness of irradiated 316 austenitic stainless steels, *Appl. Surf. Sci.* 392 (2017) 1026–1035. doi:10.1016/j.apsusc.2016.09.110.
- [29] A. Etienne, B. Radiguet, N.J. Cunningham, G.R. Odette, R. Valiev, P. Pareige, Ultramicroscopy Comparison of radiation-induced segregation in ultrafine-grained and conventional 316 austenitic stainless steels, *Ultramicroscopy*. 111 (2011) 659–663. doi:10.1016/j.ultramic.2010.12.026.
- [30] R.M. Boothby, T.M. Williams, The effects of silicon and titanium on void swelling and phase transformations in neutron irradiated 12Cr-15Ni steels, *J. Nucl. Mater.* 152 (1988) 123–138. doi:10.1016/0022-3115(88)90318-2.
- [31] M.N. Gussev, J.T. Busby, L. Tan, F.A. Garner, Magnetic phase formation in irradiated austenitic alloys, *J. Nucl. Mater.* 448 (2014) 294–300. doi:10.1016/j.jnucmat.2014.02.005.
- [32] A. Hoffman, H. Wen, R. Islamgaliev, R. Valiev, High-pressure torsion assisted segregation and precipitation in a Fe-18Cr-8Ni austenitic stainless steel, *Mater. Lett.* 243 (2019) 116–119. doi:10.1016/j.matlet.2019.02.030.
- [33] W. Mohamed, B. Miller, D. Porter, K. Murty, The role of grain size on neutron irradiation response of nanocrystalline copper, *Materials (Basel)*. 9 (2016) 1–23. doi:10.3390/ma9030144.
- [34] B. Radiguet, A. Etienne, P. Pareige, X. Sauvage, R. Valiev, Irradiation behavior of nanostructured 316 austenitic stainless steel, *J. Mater. Sci.* 43 (2008) 7338–7343. doi:10.1007/s10853-008-2875-8.
- [35] D.W. Keefer, A.G. Pabd, G.G. Rhodes, D. Kramer, Proton irradiation effects in type 321 stainless steel, *J. Nucl. Mater.* 39 (1971) 229–233. doi:10.1016/0022-3115(71)90031-6.
- [36] D.L. Porter, Ferrite formation in neutron-irradiated type 304L stainless steel, *J. Nucl. Mater.* 79 (1979) 406–411. doi:10.1016/0022-3115(79)90105-3.
- [37] S.T. Pisarik, D.C. Van Aken, Thermodynamic Driving Force of the $\gamma \rightarrow \epsilon$ Transformation and Resulting M S Temperature in High-Mn Steels, *Metall. Mater. Trans. A Phys. Metall. Mater. Sci.* 47 (2016) 1009–1018. doi:10.1007/s11661-015-3265-x.

- [38] M. Bayerlein, H.J. Christ, H. Mughrabi, Plasticity-induced martensitic transformation during cyclic deformation of AISI 304L stainless steel, *Mater. Sci. Eng. A*. 114 (1989). doi:10.1016/0921-5093(89)90871-X.
- [39] O.P. Maksimkin, Phase diffusionless $\gamma \leftrightarrow \alpha$ transformations and their effect on physical, mechanical and corrosion properties of austenitic stainless steels irradiated with neutrons and charged particles, *IOP Conf. Ser. Mater. Sci. Eng.* 130 (2016). doi:10.1088/1757-899X/130/1/012002.
- [40] R.E. Schramm, R.P. Reed, Stacking fault energies of seven commercial austenitic stainless steels, *Metall. Trans. A*. 6 (1975) 1345–1351. doi:10.1007/BF02641927.
- [41] C.G. Rhodes, A.W. Thompson, The composition dependence of stacking fault energy in austenitic stainless steels, *Metall. Trans. A*. 8 (1977) 1901–1906. doi:10.1007/bf02646563.
- [42] A. Das, Revisiting Stacking Fault Energy of Steels, *Metall. Mater. Trans. A Phys. Metall. Mater. Sci.* 47 (2016) 748–768. doi:10.1007/s11661-015-3266-9.
- [43] D.L. DOUGLASS, G. THOMAS, W.R. ROSER, Ordering, Stacking Faults and Stress Corrosion Cracking In Austenitic Alloys, *CORROSION*. 20 (1964) 15t-28t. doi:10.5006/0010-9312-20.1.15t.
- [44] H.J. Beattie, W.C. Hagel, Intermetallic compounds in titanium-hardened alloys, *Trans. AIME*. 209 (1957) 41. doi:https://doi.org/10.1007/BF03397940.
- [45] H. Ke, P. Wells, P.D. Edmondson, N. Almirall, L. Barnard, G.R. Odette, D. Morgan, Thermodynamic and kinetic modeling of Mn-Ni-Si precipitates in low-Cu reactor pressure vessel steels, *Acta Mater.* 138 (2017) 10–26. doi:10.1016/j.actamat.2017.07.021.
- [46] Z. Jiao, G.S. Was, Novel features of radiation-induced segregation and radiation-induced precipitation in austenitic stainless steels, *Acta Mater.* 59 (2011) 1220–1238. doi:10.1016/j.actamat.2010.10.055.
- [47] Z. Jiao, G.S. Was, Precipitate behavior in self-ion irradiated stainless steels at high doses, *J. Nucl. Mater.* 449 (2014) 200–206. doi:10.1016/j.jnucmat.2014.02.026.
- [48] L. Tan, J.T. Busby, Alloying effect of Ni and Cr on irradiated microstructural evolution of type 304 stainless steels, *J. Nucl. Mater.* 443 (2013) 351–358. doi:10.1016/j.jnucmat.2013.07.054.
- [49] Z. Jiao, J. Hesterberg, G.S. Was, Effect of post-irradiation annealing on the irradiated microstructure of neutron-irradiated 304L stainless steel, *J. Nucl. Mater.* 500 (2018) 220–234. doi:10.1016/j.jnucmat.2017.12.030.

- [50] T.R. Allen, G.S. Was, Modeling radiation-induced segregation in austenitic Fe-Cr-Ni alloys, *Acta Mater.* 46 (1998) 3679–3691. doi:10.1016/S1359-6454(98)00019-6.
- [51] T. Toyama, Y. Nozawa, W. Van Renterghem, Y. Matsukawa, M. Hatakeyama, Y. Nagai, A. Al Mazouzi, S. Van Dyck, Grain boundary segregation in neutron-irradiated 304 stainless steel studied by atom probe tomography, *J. Nucl. Mater.* 425 (2012) 71–75. doi:10.1016/j.jnucmat.2011.11.072.
- [52] M. Nastar, F. Soisson, *Radiation-Induced Segregation*, Elsevier Inc., 2012. doi:10.1016/B978-0-08-056033-5.00035-5.
- [53] C.S. Yoo, Y.M. Park, Y.S. Jung, Y.K. Lee, Effect of grain size on transformation-induced plasticity in an ultrafine-grained metastable austenitic steel, *Scr. Mater.* 59 (2008) 71–74. doi:10.1016/j.scriptamat.2008.02.024.
- [54] C.X. Huang, W.P. Hu, Q.Y. Wang, C. Wang, G. Yang, Y.T. Zhu, An ideal ultrafine-grained structure for high strength and high ductility, *Mater. Res. Lett.* 3 (2015) 88–94. doi:10.1080/21663831.2014.968680.
- [55] S. Turteltaub, A.S.J. Suiker, Grain size effects in multiphase steels assisted by transformation-induced plasticity, *Int. J. Solids Struct.* 43 (2006) 7322–7336. doi:10.1016/j.ijsolstr.2006.06.017.
- [56] Y.-K. Lee, C.-S. Choi, Effects of thermal cycling on the kinetics of the $\gamma \rightarrow \epsilon$ martensitic transformation in an Fe-17 wt pct Mn alloy, *Metall. Mater. Trans. A.* 31 (2000) 2735–2738. doi:10.1007/BF02830332.
- [57] A. Belyakov, K. Tsuzaki, Y. Kimura, Regularities of Deformation Microstructures in Ferritic Stainless Steels during Large Strain Cold Working, *ISIJ Int.* 48 (2008) 1071–1079. doi:10.2355/isijinternational.48.1071.
- [58] A. Belyakov, Y. Kimura, Y. Adachi, K. Tsuzaki, Microstructure Evolution in Ferritic Stainless Steels during Large Strain Deformation, *Mater. Trans.* 45 (2005) 2812–2821. doi:10.2320/matertrans.45.2812.
- [59] A. Belyakov, T. Sakai, H. Miura, K. Ts, Grain refinement in copper under large strain deformation, *Philos. Mag. A.* 81 (2001) 2629–2643. doi:10.1080/01418610110042876.
- [60] Y.F. Shen, X.X. Li, X. Sun, Y.D. Wang, L. Zuo, Twinning and martensite in a 304 austenitic stainless steel, *Mater. Sci. Eng. A.* 552 (2012) 514–522. doi:10.1016/j.msea.2012.05.080.
- [61] A.J. Ardell, P. Bellon, Radiation-induced solute segregation in metallic alloys, *Curr. Opin. Solid State Mater. Sci.* 20 (2016) 115–139. doi:10.1016/j.cossms.2015.11.001.

■ EFFECTS OF AL AND TI ADDITIONS ON THE IRRADIATION BEHAVIOR OF AN FE-MN-NI-CR MULTI-PRINCIPLE ELEMENT ALLOY

Andrew Hoffman¹, Li He², Matthew Luebbe³, Hans Pommerenke³, Jiaqi Duan³, Peipei Cao⁴, Kumar Sridharan², Zhaoping Lu^{4,*}, Haiming Wen^{1,3,*}

¹Department of Mining and Nuclear Engineering, Missouri University of Science and Technology, Rolla, MO 65409, USA

²Department of Materials Science and Engineering, Missouri University of Science and Technology, Rolla, MO 65409, USA

³Department of Engineering Physics, University of Wisconsin, Madison, WI 53706

⁴State Key Laboratory for Advanced Metals and Materials, University of Science and Technology Beijing, Beijing 100083, China

*Corresponding author: wenha@mst.edu; Tel.: +1-573-341-6167

ABSTRACT

Two Co-free multi-principal element alloys (MPEAs), a single-phase face-centered cubic (FCC) Fe₃₀Ni₃₀Mn₃₀Cr₁₀, and an (Fe₃₀Ni₃₀Mn₃₀Cr₁₀)₉₄Ti₂Al₄ (all in atomic percent) with FCC matrix containing a Ni-Ti-Al enriched L12 (ordered FCC) secondary phase (γ'), were developed and investigated in this study. The alloys were ion irradiated at 300°C and 500°C to a peak damage of 120 displacements per atom (dpa). As compared to the (Fe₃₀Ni₃₀Mn₃₀Cr₁₀)₉₄Ti₂Al₄ alloy, in the Fe₃₀Ni₃₀Mn₃₀Cr₁₀ alloy, the dislocation loops were smaller, with a higher number density. The difference in loop size between the two MPEAs was attributed to the addition of Ti in the matrix, which was anticipated to lower the stacking fault energy and stabilize the faulted Frank loops. The γ' phase showed good stability under irradiation, with no new γ' precipitation or growth in the existing precipitates. Both alloys showed similar irradiation-induced

hardening at 300°C, however, the (Fe₃₀Ni₃₀Mn₃₀Cr₁₀)₉₄Ti₂Al₄ alloy exhibited lower irradiation-induced hardening at 500°C as compared to the Fe₃₀Ni₃₀Mn₃₀Cr₁₀ alloy.

1. INTRODUCTION

Conventional steels and Ni-based alloys used in nuclear reactors suffer from a variety of degradation processes during irradiation, including void swelling, embrittlement, precipitation, and stress corrosion cracking [1]. To find a solution to these materials challenges in nuclear reactor systems, a variety of new radiation damage resistant materials' concepts have been proposed, including nanostructured steels and ceramics, ceramic composites, bulk metallic glasses, and MPEAs [alternatively called high-entropy alloys (HEAs)] [2]. MPEAs have generated interest in the last decade due to their favorable properties, which include good phase stability, high strength combined with good ductility, and superior corrosion resistance [3–6]. They are therefore promising candidate materials for nuclear reactor structural materials, where materials are subjected to both high temperatures and corrosive coolants during service.

In addition to the aforementioned advantages, select MPEAs have shown good resistance to radiation damage. Previous studies have shown that when compared to pure Fe, Ni, or conventional FeNiCr alloys, FeNi based MPEAs have reduced irradiation-induced void and dislocation loop sizes, swelling, and segregation [7–10]. The reductions in void and dislocation loop size were attributed to reduced defect mobility within a MPEA microstructures, an effect that has been verified through experiments and modeling comparing pure Ni to FeNi binary systems [10,11]. While these systems have

shown promise, many MPEA systems contain Co in significant concentrations, which is not desirable from the standpoints of neutron activation and waste management. Hence, a new MPEA system has been developed by replacing Co with Mn, and the resulting FeMnNiCr alloy was also shown to exhibit significant damage resistance to radiation [8]. Because studies of Co-free MPEAs have been limited, this study aimed to investigate and improve the understanding of such systems, especially in terms of their irradiation behavior.

Along with furthering research of the traditional single-phase FeMnNiCr alloy, this study also aimed to determine the effects of secondary phases in Co-free HEAs on irradiation behavior. The formation of a γ' secondary phase was promoted by the addition of Ti and Al to FeCoNiCr MPEA systems and shown to significantly improve mechanical properties, especially strength [12,13]. In particular, the γ' precipitates with an $L1_2$ (ordered FCC) structure in MPEAs can be compared to γ' precipitation strengthening in many Ni-based superalloys [14,15]. This secondary-phase strengthening mechanism is important to achieve good mechanical properties as previous studies showed that single-phase FCC HEAs showed poor strength at elevated temperatures [16–18]. The $(\text{Fe}_{30}\text{Ni}_{30}\text{Mn}_{30}\text{Cr}_{10})_{94}\text{Ti}_2\text{Al}_4$ investigated in this study was based on the $(\text{FeNiCoCr})_{94}\text{Ti}_2\text{Al}_4$ studied by He et. al [12], with the replacement of Co by Mn and a reduction in the Cr content to stabilize the FCC phase.

In addition to improving strength, it is anticipated that these precipitates can also enhance radiation damage resistance by creating phase interfaces that act as radiation induced defect sinks [2]. The study of multiphase MPEAs are limited, however, and more work needs to be performed in order to understand how secondary phases are affected by

irradiation. Previous irradiation studies by Yang, Xia and collaborators focused on $\text{Al}_x\text{CoCrFeNi}$ systems that formed B2 [ordered body-centered cubic (BCC)] precipitates. These studies have shown that the B2 phase is not stable, and will grow and form new precipitates during irradiation [19,20]. Kombaiah et. al showed that irradiation can induce precipitation of γ' in a single-phase $\text{Al}_{0.12}\text{CrNiFeCo}$ alloy [21]. There have been extremely limited studies, however, of the stability of γ' under irradiation in a MPEA system containing both Al and Ti. Therefore, this study served to evaluate the stability of the γ' phase under irradiation in order to aid in the design of MPEAs with stable phase compositions for nuclear reactor applications.

2. EXPERIMENTAL

Both $\text{Fe}_{30}\text{Ni}_{30}\text{Mn}_{30}\text{Cr}_{10}$ and $(\text{Fe}_{30}\text{Ni}_{30}\text{Mn}_{30}\text{Cr}_{10})_{94}\text{Ti}_2\text{Al}_4$ alloys were cast using arc-melting. The purity of each element was 99.995%, 99.995%, 99.9%, 99.95%, 99.99%, 99.99% for Fe, Ni, Mn, Cr, Ti, and Al, respectively. Following casting, samples were homogenized at 1200 °C for 10 hours. No further thermomechanical treatments were performed on the $\text{Fe}_{30}\text{Ni}_{30}\text{Mn}_{30}\text{Cr}_{10}$ alloy. Following homogenization, the $(\text{Fe}_{30}\text{Ni}_{30}\text{Mn}_{30}\text{Cr}_{10})_{94}\text{Ti}_2\text{Al}_4$ was cold rolled to a 30% reduction, solution treated at 1000°C for 2 hours, and then aged at 800°C for 18 hours. Scanning electron microscopy (SEM) and energy dispersive x-ray spectroscopy (EDS) were performed on the as-fabricated samples using a FEI Helios NanoLab SEM with an Oxford EDS system. Transmission electron microscopy (TEM) was carried out on a FEI F20 TEM. Atom Probe Tomography (APT) was conducted using a CAMECA LEAP 4000X HR atom

probe. APT experiments were performed at 44 K, in voltage mode, with a target pulse fraction of 0.2 and a detection rate of 0.005. APT data analysis was performed using CAMECA IVAS software.

The MPEA samples were irradiated using 3.7 MeV Fe^{2+} ions with a raster beam (horizontal and vertical rastering frequencies of 64 and 517 Hz, respectively) in a NEC 1.7 MV Tandem accelerator at the University of Wisconsin Ion Beam Laboratory, to a fluence of 9.9×10^{16} ion/cm² at a flux of 5.2×10^{12} ion/cm²/s at $300 \pm 5^\circ\text{C}$, or 6.9×10^{12} ion/cm²/s at $494 \pm 9^\circ\text{C}$. The sample temperature was averaged from two thermocouples attached to the opposite corners of the sample irradiation stage. The irradiations were performed in the base pressure range of $2.6 \times 10^{-6} - 7.6 \times 10^{-7}$ Torr. Figure 1 shows the simulated damage and implantation profiles of 3.7 MeV Fe^{2+} irradiation in $\text{Fe}_{30}\text{Ni}_{30}\text{Mn}_{30}\text{Cr}_{10}$, calculated using the Kinchin-Pease model with full cascade in the Stopping and Range of Ions in Matter (SRIM) software (Kinchin-Pease model is recommended for comparison of ion and neutron irradiation data while full cascade calculation is recommended with multicomponent target materials) [22–24]. SRIM software was used to calculate the damage and implantation profiles for the $(\text{Fe}_{30}\text{Ni}_{30}\text{Mn}_{30}\text{Cr}_{10})_{94}\text{Ti}_2\text{Al}_4$ samples. Results indicated that the profiles were similar to those for the $\text{Fe}_{30}\text{Ni}_{30}\text{Mn}_{30}\text{Cr}_{10}$ samples. Samples were partially masked to allow for comparison between irradiated regions and non-irradiated regions experiencing the same thermal history.

TEM lamellae were prepared from irradiated samples using a Zeiss Auriga focused ion beam (FIB). A 2 μm thick Pt protection layer was deposited on the irradiated samples, followed by 30 kV Ga^+ ion milling to produce lamellas of $\sim 15 \mu\text{m} \times 5 \mu\text{m} \times 2$

μm in size. The lamellae were lifted out and attached to a TEM grid (procured from Ted Pella Inc.) and then thinned down to electron transparency sequentially with 30, 8, and finally 2 kV Ga^+ ions. TEM characterization was conducted with a FEI TF30 instrument operated at 300 kV, while scanning transmission electron microscopy (STEM) was conducted using a FEI Titan S-Twin aberration-corrected STEM equipped with an EDS and operated at 200 kV with an electron beam semi-convergence angle of 24.5 mrad. The collection angle is 54-270 mrad for high-angle annular dark field images (HAADF), and 6 -13 mrad for annular bright field images (ABF). A rel-rod technique was used to image Frank loops, and information about the beam conditions for rel-rod imaging can be found in studies by Sencer et. al and Edwards et. al [25,26]. Nanoindentation was performed using a Hysitron TI-950 TriboIndenter and a cube-corner tip in the displacement control mode. Indentations were performed at three displacement depths: 0.1 μm , 0.15 μm , and 0.2 μm . These indentation depths are designed to be shallow enough that the full interaction volume is contained within the irradiated region [27]. At each depth ten indentations were performed.

3. RESULTS AND DISCUSSION

The $\text{Fe}_{30}\text{Ni}_{30}\text{Mn}_{30}\text{Cr}_{10}$ alloy formed a single solution FCC phase with a sporadic distribution of MnO inclusions, which were previously reported in a comparable $\text{Fe}_{27}\text{Ni}_{28}\text{Mn}_{27}\text{Cr}_{18}$ alloy [8]. Their number density is not high enough, however, to be considered relevant to the irradiation study performed. After homogenization, only a single solid-solution FCC phase was observed in the $(\text{Fe}_{30}\text{Ni}_{30}\text{Mn}_{30}\text{Cr}_{10})_{94}\text{Ti}_2\text{Al}_4$ alloy.

However, after cold rolling, solution treatment, and aging at 800°C, γ' $\text{Ni}_3(\text{Al,Ti})$ precipitates were formed. Figure 2a-g show an secondary electron image and EDS maps of the $(\text{Fe}_{30}\text{Ni}_{30}\text{Mn}_{30}\text{Cr}_{10})_{94}\text{Ti}_2\text{Al}_4$ alloy with many γ' precipitates. These precipitates form elongated structures with lengths on the order of 1 μm and widths on the order of 250 nm as seen in the TEM bright-field (BF) image in Figure 2h. Figure 3 shows an BF TEM image of a γ' precipitates with a selected area diffraction pattern (SAED) indicating a L1_2 (ordered FCC) structure that is typical of the γ' phase. Composition of the matrix and γ' precipitates in the $(\text{Fe}_{30}\text{Ni}_{30}\text{Mn}_{30}\text{Cr}_{10})_{94}\text{Ti}_2\text{Al}_4$ alloy, obtained from EDS or APT, are shown in Table 1. Each reported EDS measurement was averaged from 10 point or line scans. It is noted that APT experiments were only able to capture a reconstruction volume of one γ' precipitate and, therefore, no standard deviation of the composition could be obtained. It is also noted that in the $(\text{Fe}_{30}\text{Ni}_{30}\text{Mn}_{30}\text{Cr}_{10})_{94}\text{Ti}_2\text{Al}_4$ alloy, after casting the content of Ti was higher than anticipated.

Figure 4a and b show TEM BF images of small dislocation loops in the $\text{Fe}_{30}\text{Ni}_{30}\text{Mn}_{30}\text{Cr}_{10}$ MPEA after irradiation at 300°C. Most of these loops were less than 10 nm in diameter, although the largest loops had a diameter of ~ 35 nm. Figs. 4c and d show TEM BF image and the associated rel-rod image of the $\text{Fe}_{30}\text{Ni}_{30}\text{Mn}_{30}\text{Cr}_{10}$ MPEA after irradiation at 500°C. The rel-rod image shows the formation of some larger loops on the order of 100 nm, although the BF image shows that most of the dislocations caused by irradiation in this sample are either smaller loops or form dislocation networks.

Figure 5a and b display TEM BF and associated rel-rod images of $(\text{Fe}_{30}\text{Ni}_{30}\text{Mn}_{30}\text{Cr}_{10})_{94}\text{Ti}_2\text{Al}_4$ after irradiation at 300°C. Multiple smaller Frank loops with sizes on the order of 20 nm were observed. Figs. 5c and d show

$(\text{Fe}_{30}\text{Ni}_{30}\text{Mn}_{30}\text{Cr}_{10})_{94}\text{Ti}_2\text{Al}_4$ after irradiation at 500°C. At 500°C the alloy exhibited a small increase in the average loop size (from ~20 to ~30 nm), but larger loops on the order of 170 nm were also observed.

Under the irradiation conditions tested, no voids were detected in either MPEA. This may not be due to the intrinsic properties of the alloys, but rather due to the fact that the irradiation was performed with rastered beam rather than a defocused beam, which can reduce the void development and swelling during ion irradiation [28]. Thus, swelling was not evaluated in this study. Nevertheless, this study provided valuable insights through comparisons in the development of dislocation loops in FeNiMnCr based alloy systems.

Figure 6 shows histograms of the loop size distribution for the $\text{Fe}_{30}\text{Ni}_{30}\text{Mn}_{30}\text{Cr}_{10}$ and $(\text{Fe}_{30}\text{Ni}_{30}\text{Mn}_{30}\text{Cr}_{10})_{94}\text{Ti}_2\text{Al}_4$ irradiated at 300°C and 500°C, while Table 2 summarizes the average size and number density of dislocation loops in the two alloys. As expected, loop size increased with irradiation temperature, accompanied by a decrease in number density, as point defects and small dislocation loops diffused and combined. This behavior was previously observed in a $\text{Al}_{0.1}\text{CoCrFeNi}$ MPEA [29]. Moreover, the $\text{Fe}_{30}\text{Ni}_{30}\text{Mn}_{30}\text{Cr}_{10}$ and $(\text{Fe}_{30}\text{Ni}_{30}\text{Mn}_{30}\text{Cr}_{10})_{94}\text{Ti}_2\text{Al}_4$ alloys also differ in the observed loop size. In the $\text{Fe}_{30}\text{Ni}_{30}\text{Mn}_{30}\text{Cr}_{10}$ alloy, the loop sizes tended to be smaller with a much higher number density, which was anticipated from previous results of irradiated MPEAs [7,9]. In the $(\text{Fe}_{30}\text{Ni}_{30}\text{Mn}_{30}\text{Cr}_{10})_{94}\text{Ti}_2\text{Al}_4$ MPEA, however, there was an increase in the size of dislocation loops with the addition of Al and Ti. This same behavior of increased faulted loop size was also seen by Chen et. al in a helium irradiated $\text{FeCoNiCrTi}_{0.2}$ HEA, and this was attributed to a decrease in SFE from the addition of Ti to the system [30].

This increase in the average loop size can, consequently, be attributed to the alloying of Al and Ti in the $(\text{Fe}_{30}\text{Ni}_{30}\text{Mn}_{30}\text{Cr}_{10})_{94}\text{Ti}_2\text{Al}_4$ system. It is well known that Ti reduces the stacking fault energy in austenitic steels [31,32], and the addition of Ti to an $\text{Fe}_{30}\text{Ni}_{30}\text{Co}_{30}\text{Mn}_{10}$ MPEA increased the twin boundary density, which is directly related to a lowering of stacking fault energy [33]. Because Ti is a hexagonal close-packed (HCP) structure with an ABAB stacking, stacking faults in the FCC structure (which is ABCABC) can be viewed as single plane HCP structures since an FCC stacking fault leads to **ABABC** stacking. Al may also lower the SFE, as shown by Peijun et. al for Al additions to an FeNiCoCr HPEA where such lowering of SFE assisted in the formation of nanotwins [34]. Meanwhile, the precipitation of high SFE elements (Ni and Al) from the matrix is also anticipated to lower the SFE of the matrix.

Although the formation of γ' precipitates consumes a notable amount of Ti, a significant concentration of Ti remained within the matrix, as can be seen in Table 1. Loops enriched in Ti were also observed as can be seen in Figure 7. This enrichment in Ti may have been due to radiation-induced segregation to dislocation loops, and if so, this behavior would be unique. While Ti can enrich at defect sinks (such as dislocation loops), Ni also enriches at defect sinks in conventional FCC Fe-Cr-Ni austenitic steels under irradiation [35,36]. This Ni enrichment was not observed within the loops in this study. Ti enrichment within these faulted Frank loops would lower the stacking fault energy and allow for these loops to grow even further. Thus, the increased size of faulted loops in the $(\text{Fe}_{30}\text{Ni}_{30}\text{Mn}_{30}\text{Cr}_{10})_{94}\text{Ti}_2\text{Al}_4$ alloy could be directly attributed to the addition of Ti, which lowered the stacking fault energy.

Figure 8 shows TEM images of the $(\text{Fe}_{30}\text{Ni}_{30}\text{Mn}_{30}\text{Cr}_{10})_{94}\text{Ti}_2\text{Al}_4$ ion irradiated at 300 and 500°C, showing the γ' precipitates both within and outside the irradiated regions. The morphology and size of the precipitates did not appear to be affected by the irradiation. Such phenomenon in this system differs from the observation in previous studies of other FCC MPEAs where the addition of Al caused secondary phases to grow or new precipitates to form (or both) under irradiation. Yang et. al showed that, although single-phase $\text{Al}_{0.1}\text{CoCrFeNi}$ exhibited good phase stability, higher Al content in $\text{Al}_x\text{CoCrFeNi}$ in general caused the Ni-Al enriched B2 phase to both grow and precipitate further under irradiation [19,20]. This B2 phase consistently occurs in FCC FeNiCoCr based MPEAs with higher Al content (in the absence of Ti) [37]. However, Kombaiah et. al showed that in a single-phase FCC $\text{Al}_{0.12}\text{CrNiFeCo}$, irradiation at 500°C induced precipitation of $L1_2$ structured Ni_3Al , which was believed to have been caused by non-equilibrium radiation induced diffusion [21]. It is noted that even after long term annealing, Kombaiah et. al did not observe precipitation, indicating that the precipitation observed after irradiation was purely driven by the kinetics of irradiation. It is clear, therefore, that $\text{Al}_x\text{CoCrFeNi}$ based systems, no matter single FCC phase or BCC phases containing, exhibit poor phase stability under irradiation. In our $(\text{Fe}_{30}\text{Ni}_{30}\text{Mn}_{30}\text{Cr}_{10})_{94}\text{Ti}_2\text{Al}_4$ system, the additions of Ti and Al lead to the formation of $L1_2$ (ordered FCC) γ' $\text{Ni}_3(\text{Al},\text{Ti})$ precipitates, which was previously observed by both He et. al and Zhao et. al in a $(\text{FeNiCoCr})_{94}\text{Ti}_2\text{Al}_4$ system [12,38]. $\text{FeNiCoCrAl}_x\text{Ti}_y$ alloys containing the γ' phase were originally studied due to their desirable mechanical properties, however, the current study shows that $\text{Ni}_3(\text{Ti},\text{Al}) \gamma'$ may also have extraordinary phase stability under irradiation. This stability may be due, in part, from the

structural coherency of the L_{12} phase with the FCC matrix. The synergistic effects of Ti and Al may also have played a key role in stabilizing this secondary phase. Chen et. al showed that in FCC based MPEAs containing γ' , Ti is the primary L_{12} phase former with Al acting as a stabilizer, and that the Ti/Al ratio should be between 0.7 and 2 to stabilize the L_{12} phase [39]. Chen also showed that Cr and Fe can narrow the stability region of the L_{12} phase [39]. Thus, the phase stability of γ' in the $(Fe_{30}Ni_{30}Mn_{30}Cr_{10})_{94}Ti_2Al_4$ alloy in this study may be attributed to both the synergistic effects of Ti and Al, and the lowering of the Cr content in this alloy. While the Ti/Al ratio in the $(Fe_{30}Ni_{30}Mn_{30}Cr_{10})_{94}Ti_2Al_4$ alloy in this study is low (0.5), the stability region may be broadened due to the decrease in the Cr content. Stability of precipitates and solid solution under irradiation are key to preventing irradiation-induced changes and consequently the mechanical properties of structural materials. In future designs of FeNiCr based MPEAs where secondary phases are utilized for either enhanced strength or as defect sinks, it may be beneficial to design alloy compositions which promote Ni-Al-Ti enriched ordered FCC secondary phase rather than a Ni-Al rich ordered BCC secondary phase from the standpoint of stability under radiation.

Table 3 shows the results of nanoindentation for both MPEAs after ion irradiation at 300°C and 500°C. Results compare the differences in hardness between the irradiated regions and the masked unirradiated regions. At 300°C, both alloys demonstrated very similar irradiation-induced hardening. Although the $(Fe_{30}Ni_{30}Mn_{30}Cr_{10})_{94}Ti_2Al_4$ alloy showed larger loop size overall, number density of loops was much lower in this alloy. At 500°C the irradiation induced hardening of $(Fe_{30}Ni_{30}Mn_{30}Cr_{10})_{94}Ti_2Al_4$ was approximately half that of the $Fe_{30}Ni_{30}Mn_{30}Cr_{10}$ alloy suggesting that Ti and Al additions

are effective at reducing irradiation induced hardening for higher temperature irradiations. The $(\text{Fe}_{30}\text{Ni}_{30}\text{Mn}_{30}\text{Cr}_{10})_{94}\text{Ti}_2\text{Al}_4$ alloy irradiated at 500°C showed a larger average loop size and lower number density of loops compared to irradiated $\text{Fe}_{30}\text{Ni}_{30}\text{Mn}_{30}\text{Cr}_{10}$ alloy which is attributed to the resistance to irradiation induced hardening. Although the number density of γ' precipitates was low, they are assumed to have contributed to the irradiation resistance in the $(\text{Fe}_{30}\text{Ni}_{30}\text{Mn}_{30}\text{Cr}_{10})_{94}\text{Ti}_2\text{Al}_4$ alloy. Further work is being conducted to optimize heat treatments to increase number density and decrease the size of the γ' precipitates.

4. CONCLUSIONS

The radiation damage behavior of two Co-free MPEAs, namely a single-phase FCC $\text{Fe}_{30}\text{Ni}_{30}\text{Mn}_{30}\text{Cr}_{10}$, and an $(\text{Fe}_{30}\text{Ni}_{30}\text{Mn}_{30}\text{Cr}_{10})_{94}\text{Ti}_2\text{Al}_4$ in which the matrix was FCC structured single phase with an Ni-Ti-Al enriched $L1_2$ (ordered FCC) secondary phase, has been investigated. The study was performed by ion irradiation of the samples with Fe^{2+} ions up to 120 dpa at 300°C and 500°C . The following conclusions are made:

(1) Both $\text{Fe}_{30}\text{Ni}_{30}\text{Mn}_{30}\text{Cr}_{10}$ and $(\text{Fe}_{30}\text{Ni}_{30}\text{Mn}_{30}\text{Cr}_{10})_{94}\text{Ti}_2\text{Al}_4$ showed an increase in loop size at higher irradiation temperatures, due to the enhanced diffusion of defects and defect clusters.

(2) The $(\text{Fe}_{30}\text{Ni}_{30}\text{Mn}_{30}\text{Cr}_{10})_{94}\text{Ti}_2\text{Al}_4$ alloy formed larger loops with a smaller number density than those observed in the $\text{Fe}_{30}\text{Ni}_{30}\text{Mn}_{30}\text{Cr}_{10}$. This effect is attributed to the addition of Ti, which lowered the stacking fault energy of the FCC system and increased the stability of faulted Frank loops.

(3) The $L1_2 \gamma'$ phase was stable under ion irradiation with no observed irradiation-induced growth or further precipitation.

(4) Both the $Fe_{30}Ni_{30}Mn_{30}Cr_{10}$ and $(Fe_{30}Ni_{30}Mn_{30}Cr_{10})_{94}Ti_2Al_4$ alloys showed comparable radiation-induced hardening at 300°C. At 500°C the $(Fe_{30}Ni_{30}Mn_{30}Cr_{10})_{94}Ti_2Al_4$ alloy had significantly less radiation-induced hardening than the $Fe_{30}Ni_{30}Mn_{30}Cr_{10}$ alloy, due to a lower number density of dislocation loops.

ACKNOWLEDGEMENTS

This research was financially supported by the U.S. Department of Energy, Office of Nuclear Energy through the Nuclear Science User Facilities (NSUF) – Rapid Turnabout Experiment (RTE) Program (award number 17-865). Partial support for Andrew Hoffman, Hans Pommerenke and Haiming Wen came from the U.S. Nuclear Regulatory Commission (NRC) Faculty Development Program (award number NRC 31310018M0044). Nathan Curtis and Victor DeLibera are thanked for their assistance in sample preparation.

Table 1. Composition of matrix and γ' precipitates in $(Fe_{30}Ni_{30}Mn_{30}Cr_{10})_{94}Ti_2Al_4$ MPEA.

	Nominal Composition	Matrix (EDS)	Matrix (APT)	γ' (EDS)	γ' (APT)
At.% Al	4	1.16 ± 0.42	1.87 ± 0.43	7.36 ± 2.24	12.9
At.% Ti	2	1.43 ± 0.53	2.48 ± 0.35	4.79 ± 1.4	6.12
At.% Cr	9.4	8.21 ± 1.56	7.62 ± 0.73	1.42 ± 3	0.5
At.% Mn	28.2	31.72 ± 2.68	30.08 ± 1.58	30 ± 2.65	29.43
At.% Fe	28.2	25.94 ± 4.56	26.43 ± 4.71	7.03 ± 9.15	3.53
At.% Ni	28.2	31.5 ± 3.31	31.48 ± 3.15	49.37 ± 7.97	47.52

Table 2. Summary of dislocation loop size and number density in $\text{Fe}_{30}\text{Ni}_{30}\text{Mn}_{30}\text{Cr}_{10}$ and $(\text{Fe}_{30}\text{Ni}_{30}\text{Mn}_{30}\text{Cr}_{10})_{94}\text{Ti}_2\text{Al}_4$ MPEAs ion irradiated nominally to 100 dpa

Alloy	Temperature	Average Loop Size	Loop Density
$\text{Fe}_{30}\text{Ni}_{30}\text{Mn}_{30}\text{Cr}_{10}$	300 °C	6.42 ± 6.4 nm	$1.1 \times 10^{22} \text{ m}^{-3}$
$\text{Fe}_{30}\text{Ni}_{30}\text{Mn}_{30}\text{Cr}_{10}$	500 °C	30.94 ± 37.8 nm	$5.63 \times 10^{21} \text{ m}^{-3}$
$(\text{Fe}_{30}\text{Ni}_{30}\text{Mn}_{30}\text{Cr}_{10})_{94}\text{Ti}_2\text{Al}_4$	300 °C	22.6 ± 10.3 nm	$4.11 \times 10^{21} \text{ m}^{-3}$
$(\text{Fe}_{30}\text{Ni}_{30}\text{Mn}_{30}\text{Cr}_{10})_{94}\text{Ti}_2\text{Al}_4$	500 °C	47.8 ± 36.6 nm	$3.49 \times 10^{21} \text{ m}^{-3}$

Table 3. Summary of irradiation induced hardening from nanoindentation.

Alloy	Temperature	% Irradiation Hardening (
$\text{Fe}_{30}\text{Ni}_{30}\text{Mn}_{30}\text{Cr}_{10}$	300°C	87 ± 2 %
$\text{Fe}_{30}\text{Ni}_{30}\text{Mn}_{30}\text{Cr}_{10}$	500°C	37 ± 2 %
$(\text{Fe}_{30}\text{Ni}_{30}\text{Mn}_{30}\text{Cr}_{10})_{94}\text{Ti}_2\text{Al}_4$	300°C	76 ± 2 %
$(\text{Fe}_{30}\text{Ni}_{30}\text{Mn}_{30}\text{Cr}_{10})_{94}\text{Ti}_2\text{Al}_4$	500°C	15 ± 4 %

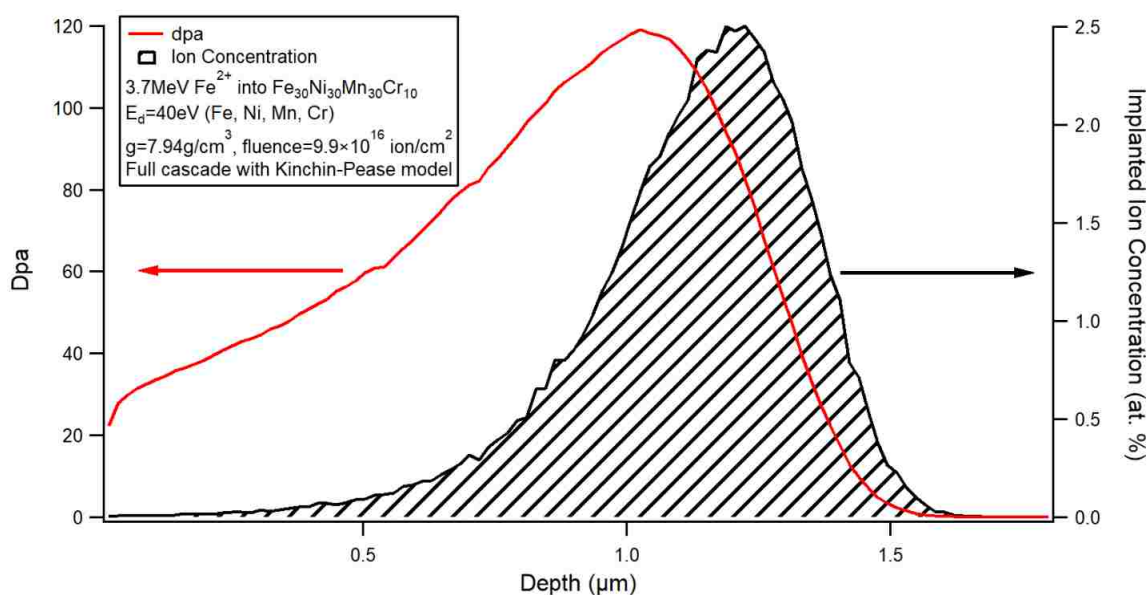


Figure 1. 3.7 MeV Fe^{2+} induced damage and implantation profiles in $\text{Fe}_{30}\text{Ni}_{30}\text{Mn}_{30}\text{Cr}_{10}$. E_d is atom displacement energy.

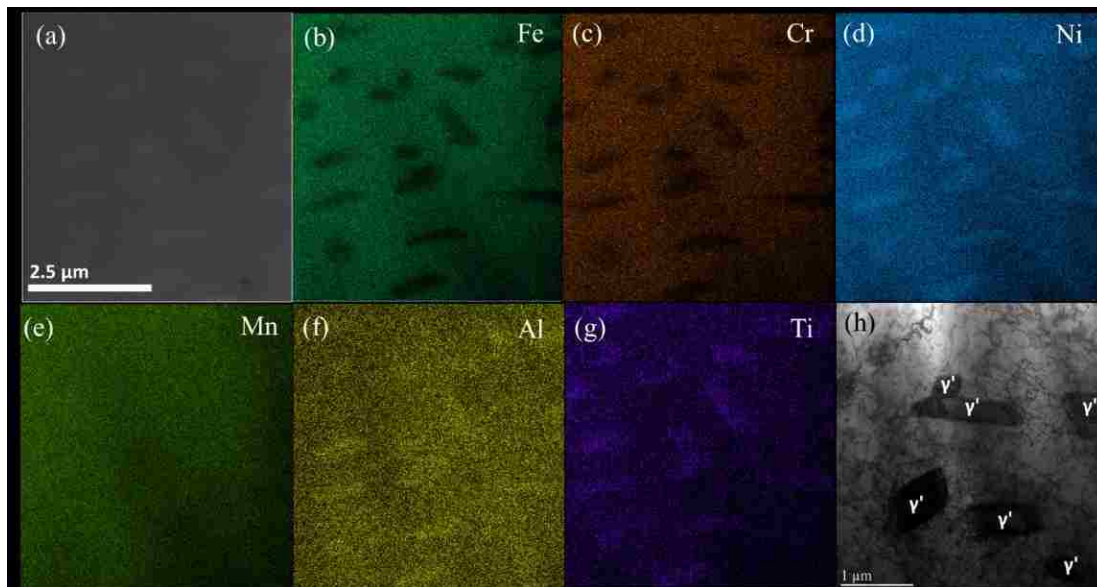


Figure 2. a) SEM secondary electron image and b)-g) corresponding EDS maps of $(\text{Fe}_{30}\text{Ni}_{30}\text{Mn}_{30}\text{Cr}_{10})_{94}\text{Ti}_2\text{Al}_4$ after cold rolling and annealing, showing the Ni, Ti, and Al enriched γ' phase. h) TEM bright field of γ' precipitates.

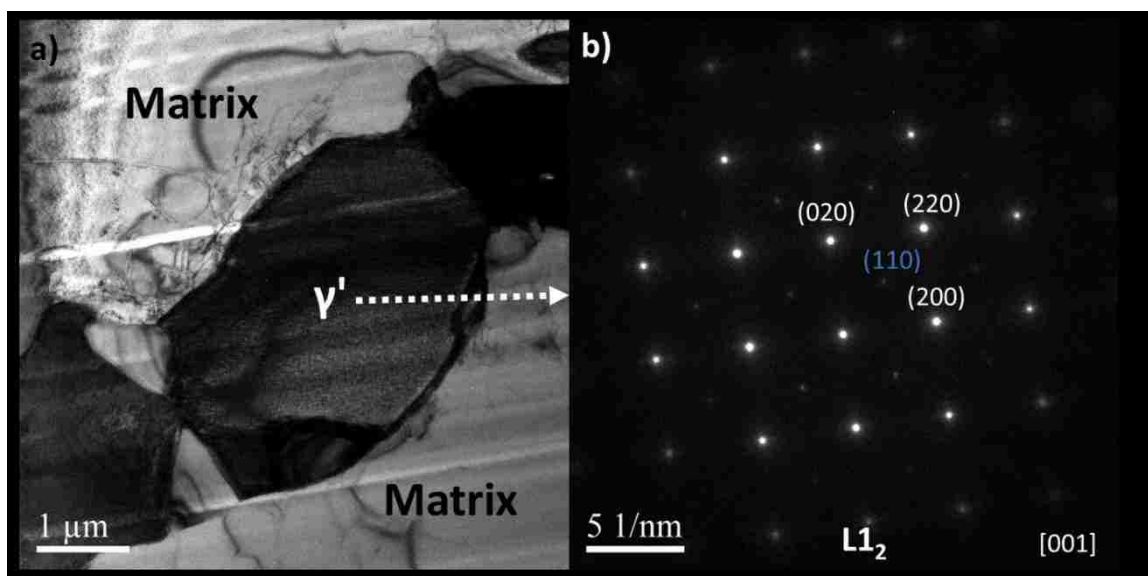


Figure 3. a) TEM bright field and b) selected area electron diffraction (SAED) pattern showing the structure of γ' phase in the $(\text{Fe}_{30}\text{Ni}_{30}\text{Mn}_{30}\text{Cr}_{10})_{94}\text{Ti}_2\text{Al}_4$ HEA to be $L1_2$ (ordered FCC).

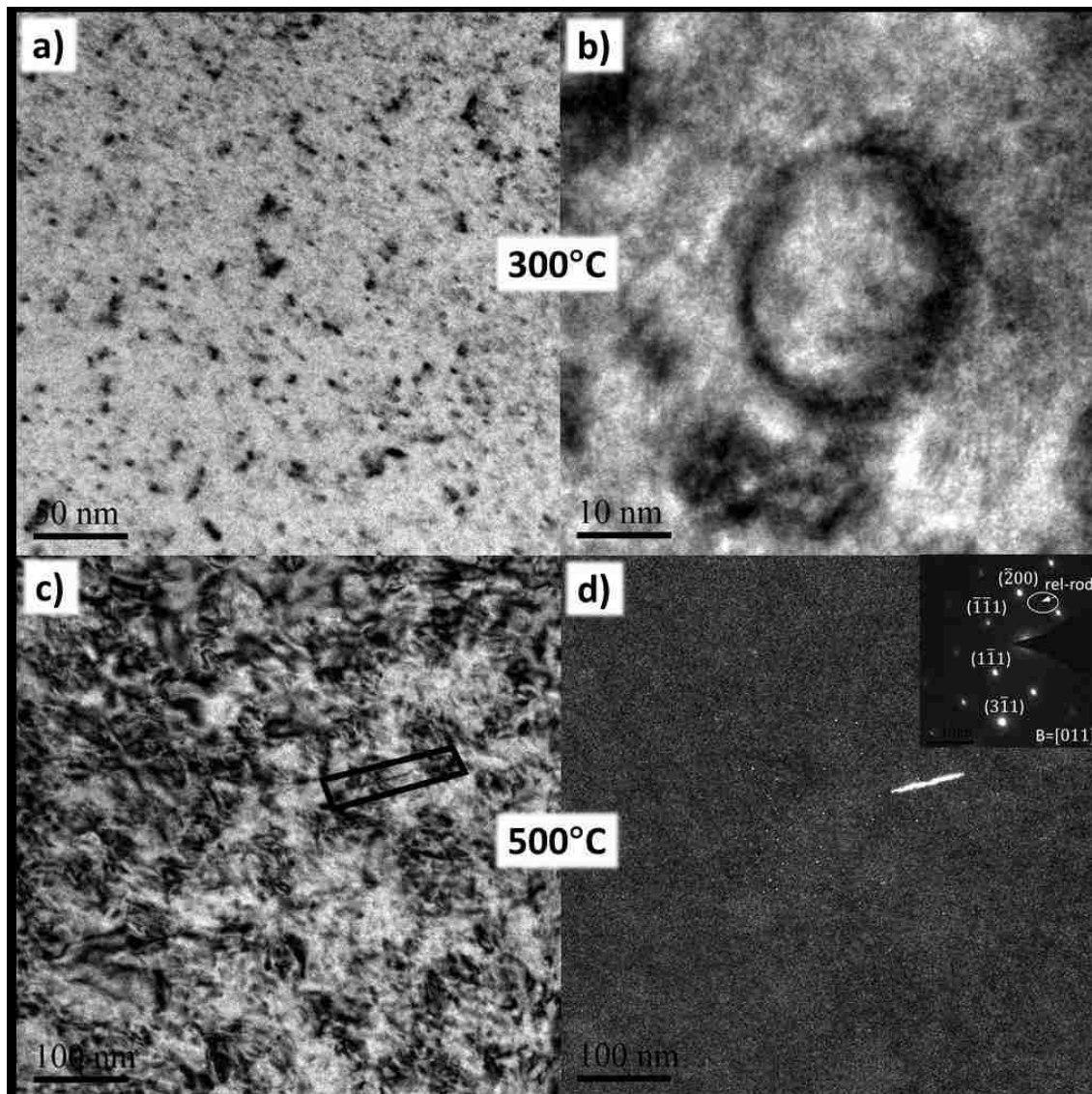


Figure 4. TEM results of $\text{Fe}_{30}\text{Ni}_{30}\text{Mn}_{30}\text{Cr}_{10}$ ion irradiated up to 120 dpa. a) and b) bright field of dislocation loops in the 300 °C irradiated sample. c) bright field and d) rel-rod image with SAED pattern (inset) of the 500 °C irradiated sample.

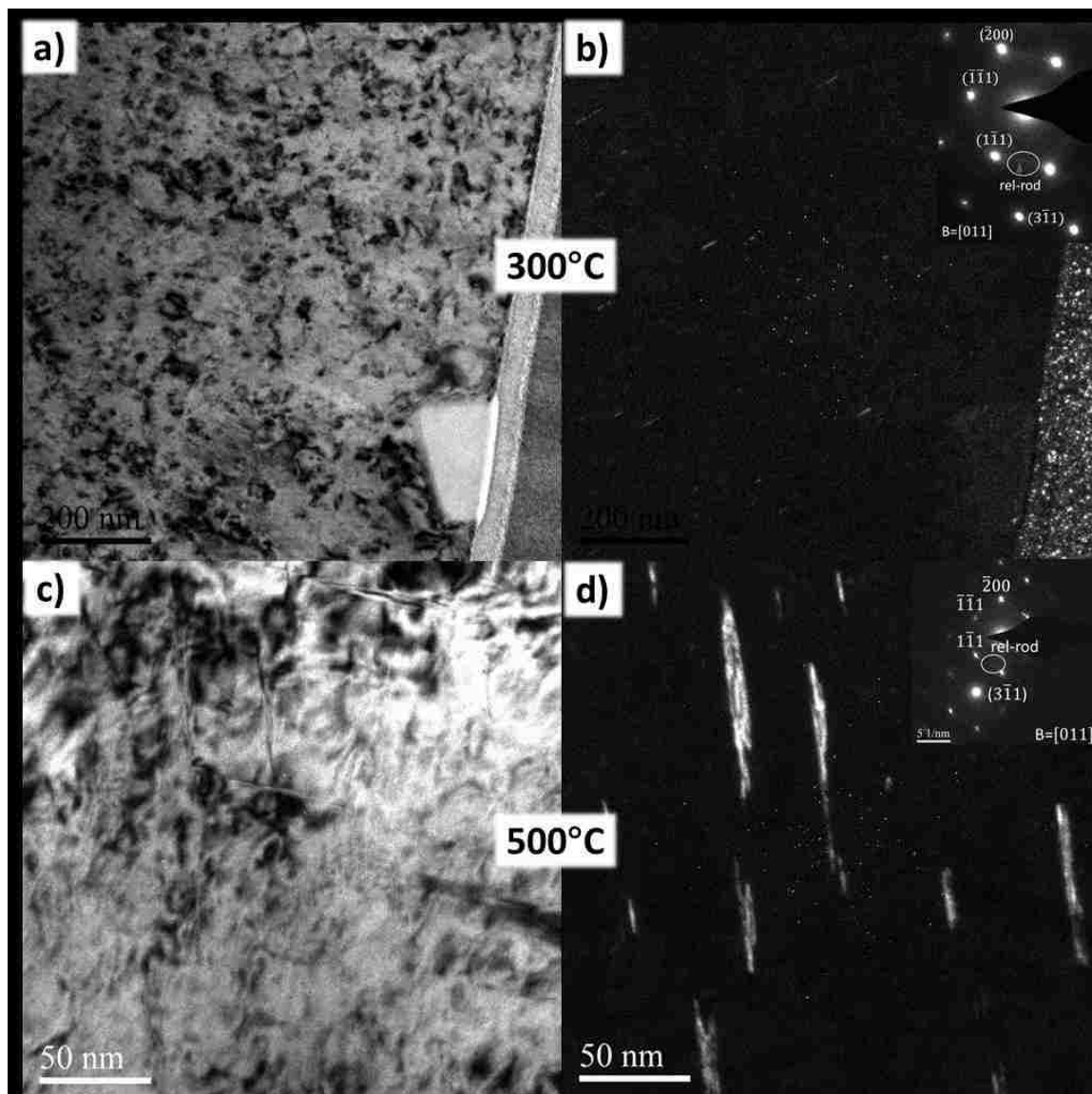


Figure 5. TEM results of $(\text{Fe}_{30}\text{Ni}_{30}\text{Mn}_{30}\text{Cr}_{10})_{94}\text{Ti}_2\text{Al}_4$ ion irradiated up to 120 dpa. a) bright field and b) rel-rod image with SAED pattern (inset) of the 300 °C irradiated sample. Beam conditions for a) and b) were $g=222$ with a $11\bar{2}$ zone axis. c) bright field and d) rel-rod image with SAED pattern (inset) of the 500 °C irradiated sample.

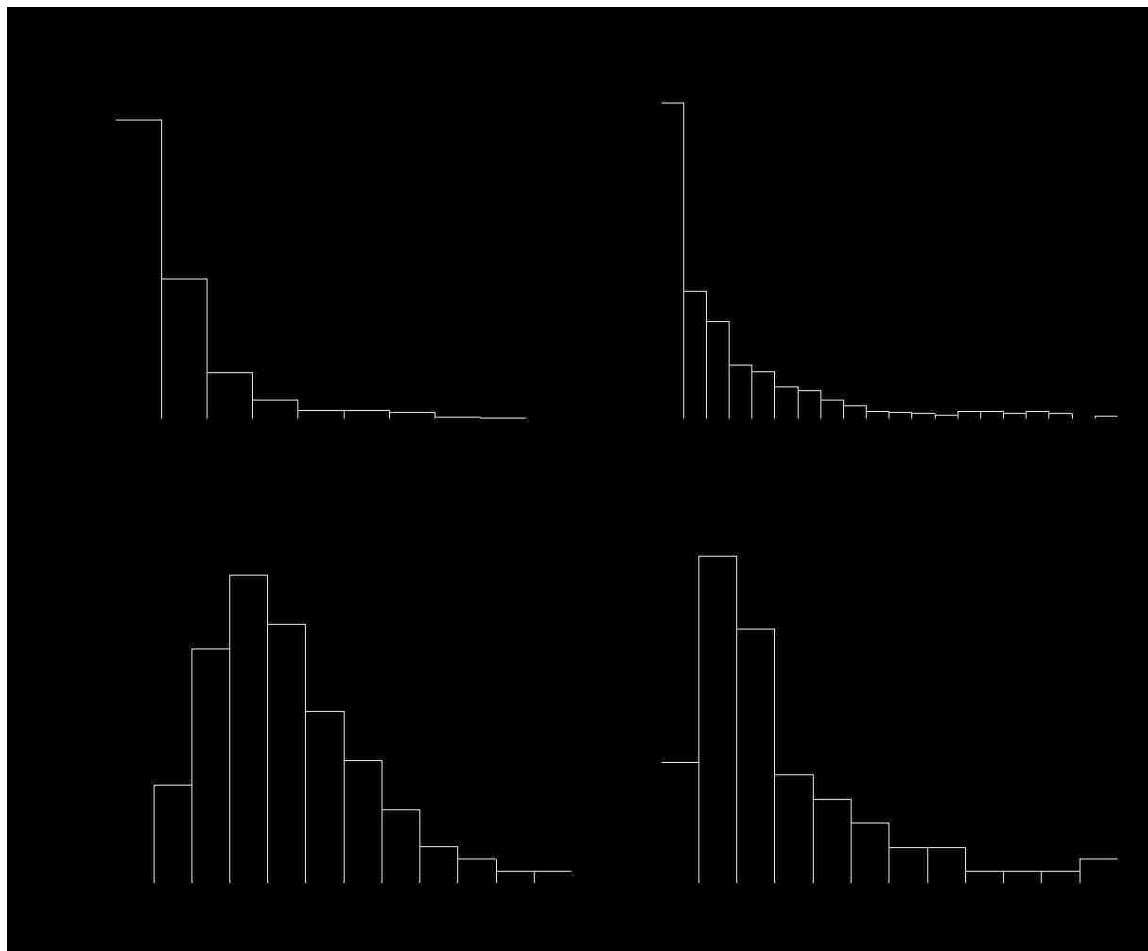


Figure 6. Loop size distribution for $\text{Fe}_{30}\text{Ni}_{30}\text{Mn}_{30}\text{Cr}_{10}$ ion irradiated at a) 300 °C and b) 500 °C and $(\text{Fe}_{30}\text{Ni}_{30}\text{Mn}_{30}\text{Cr}_{10})_{94}\text{Ti}_2\text{Al}_4$ ion irradiated at c) 300 °C and d) 500 °C.

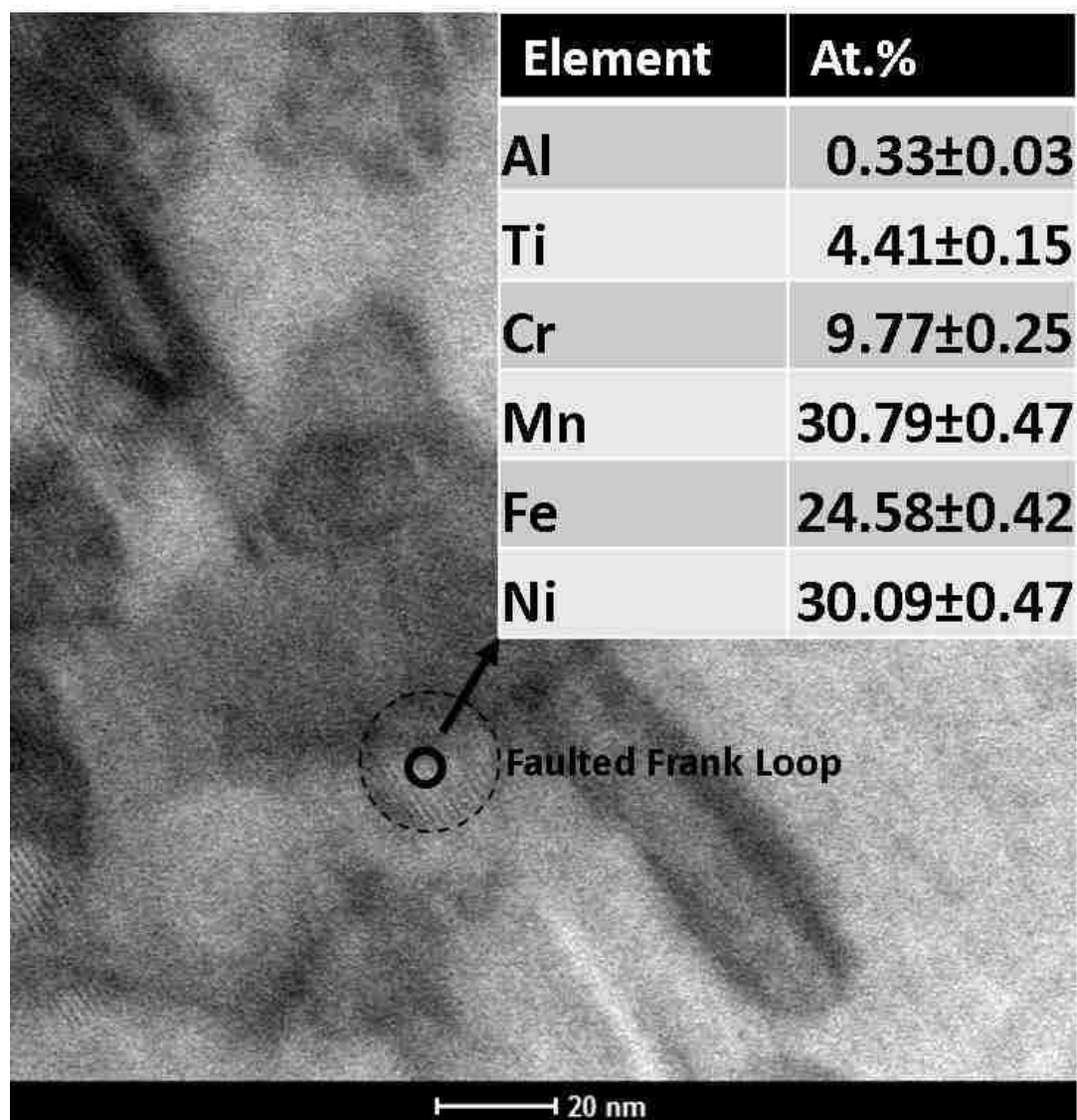


Figure 7. STEM bright field image of a faulted dislocation loop and associated EDS point scans showing an enrichment of Ti.

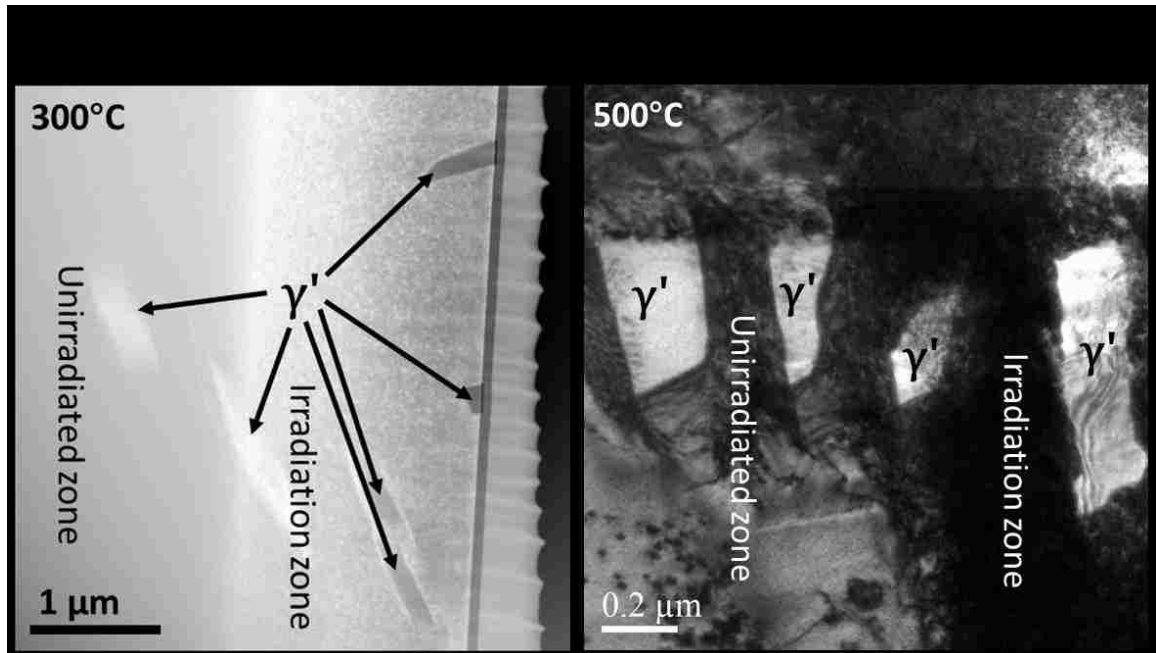


Figure 8. STEM dark-field image of 300 °C irradiated $(\text{Fe}_{30}\text{Ni}_{30}\text{Mn}_{30}\text{Cr}_{10})_{94}\text{Ti}_2\text{Al}_4$ (left) and TEM bright-field image of 500 °C irradiated $(\text{Fe}_{30}\text{Ni}_{30}\text{Mn}_{30}\text{Cr}_{10})_{94}\text{Ti}_2\text{Al}_4$ (right) showing the morphology of γ' precipitates in the irradiated and unirradiated regions.

REFERENCES

1. S. J. Zinkle and G. S. Was, *Acta Mater.* **61**, 735 (2013).
2. S. J. Zinkle, *Advanced Irradiation-Resistant Materials for Generation IV Nuclear Reactors* (Elsevier Ltd, 2016).
3. M. H. Tsai and J. W. Yeh, *Mater. Res. Lett.* **2**, 107 (2014).
4. D. B. Miracle and O. N. Senkov, *Acta Mater.* **122**, 448 (2017).
5. Y. Shi, B. Yang, and P. Liaw, *Metals (Basel)*. **7**, 43 (2017).
6. Y. Zhang, T. T. Zuo, Z. Tang, M. C. Gao, K. A. Dahmen, P. K. Liaw, and Z. P. Lu, *Prog. Mater. Sci.* **61**, 1 (2014).
7. M. R. He, S. Wang, K. Jin, H. Bei, K. Yasuda, S. Matsumura, K. Higashida, and I. M. Robertson, *Scr. Mater.* **125**, 5 (2016).

8. N. A. P. K. Kumar, C. Li, K. J. Leonard, H. Bei, and S. J. Zinkle, *Acta Mater.* **113**, 230 (2016).
9. W. Y. Chen, X. Liu, Y. Chen, J. W. Yeh, K. K. Tseng, and K. Natesan, *J. Nucl. Mater.* **510**, 421 (2018).
10. F. Granberg, K. Nordlund, M. W. Ullah, K. Jin, C. Lu, H. Bei, L. M. Wang, F. Djurabekova, W. J. Weber, and Y. Zhang, *Phys. Rev. Lett.* **116**, 1 (2016).
11. D. S. Aidhy, C. Lu, K. Jin, H. Bei, Y. Zhang, L. Wang, and W. J. Weber, *Acta Mater.* **99**, 69 (2015).
12. J. Y. He, H. Wang, H. L. Huang, X. D. Xu, M. W. Chen, Y. Wu, X. J. Liu, T. G. Nieh, K. An, and Z. P. Lu, *Acta Mater.* **102**, 187 (2016).
13. Z. Fu, L. Jiang, J. L. Wardini, B. E. MacDonald, H. Wen, W. Xiong, D. Zhang, Y. Zhou, T. J. Rupert, W. Chen, and E. J. Lavernia, *Sci. Adv.* **4**, eaat8712 (2018).
14. T. Murakumo, T. Kobayashi, Y. Koizumi, and H. Harada, *Acta Mater.* **52**, 3737 (2004).
15. Y. Q. Chen, E. Francis, J. Robson, M. Preuss, and S. J. Haigh, *Acta Mater.* **85**, 199 (2015).
16. Y. Wu, W. H. Liu, X. L. Wang, D. Ma, A. D. Stoica, T. G. Nieh, Z. B. He, and Z. P. Lu, *Appl. Phys. Lett.* **104**, (2014).
17. F. Otto, A. Dlouhý, C. Somsen, H. Bei, G. Eggeler, and E. P. George, *Acta Mater.* **61**, 5743 (2013).
18. B. Gludovatz, A. Hohenwarter, D. Catoor, E. H. Chang, E. P. George, and R. O. Ritchie, *Science* (80-.). **345**, 1153 (2014).
19. T. Yang, S. Xia, S. Liu, C. Wang, S. Liu, Y. Fang, Y. Zhang, J. Xue, S. Yan, and Y. Wang, *Sci. Rep.* **6**, 1 (2016).
20. S. Q. Xia, X. Yang, T. F. Yang, S. Liu, and Y. Zhang, *JOM* **67**, 2340 (2015).
21. B. Kombaiah, K. Jin, H. Bei, P. D. Edmondson, and Y. Zhang, *Mater. Des.* **160**, 1208 (2018).
22. J. F. Ziegler, M. D. Ziegler, and J. P. Biersack, *Nucl. Instruments Methods Phys. Res. Sect. B Beam Interact. with Mater. Atoms* **268**, 1818 (2010).
23. R. E. Stoller, M. B. Toloczko, G. S. Was, A. G. Certain, S. Dwaraknath, and F. A. Garner, *Nucl. Instruments Methods Phys. Res. Sect. B Beam Interact. with Mater. Atoms* **310**, 75 (2013).

24. W. J. Weber and Y. Zhang, *Curr. Opin. Solid State Mater. Sci.* 0 (2019).
25. D. J. Edwards, E. P. Simonen, and S. M. Bruemmer, *J. Nucl. Mater.* **317**, 13 (2003).
26. B. H. Sencer, G. S. Was, M. Sagisaka, Y. Isobe, G. M. Bond, and F. A. Garner, *J. Nucl. Mater.* **323**, 18 (2003).
27. P. Hosemann, D. Kiener, Y. Wang, and S. A. Maloy, *J. Nucl. Mater.* **425**, 136 (2012).
28. J. G. Gigax, E. Aydogan, T. Chen, D. Chen, L. Shao, Y. Wu, W. Y. Lo, Y. Yang, and F. A. Garner, *J. Nucl. Mater.* **465**, 343 (2015).
29. T. Yang, S. Xia, W. Guo, R. Hu, J. D. Poplawsky, G. Sha, Y. Fang, Z. Yan, C. Wang, C. Li, Y. Zhang, S. J. Zinkle, and Y. Wang, *Scr. Mater.* **144**, 31 (2018).
30. D. Chen, Y. Tong, J. Wang, B. Han, Y. L. Zhao, F. He, and J. J. Kai, *J. Nucl. Mater.* **510**, 187 (2018).
31. D. L. DOUGLASS, G. THOMAS, and W. R. ROSER, *CORROSION* **20**, 15t (1964).
32. A. Das, *Metall. Mater. Trans. A Phys. Metall. Mater. Sci.* **47**, 748 (2016).
33. B. Wu, W. Chen, Z. Jiang, Z. Chen, and Z. Fu, *Mater. Sci. Eng. A* **676**, 492 (2016).
34. P. Yu, Y. Zhuang, J.-P. Chou, J. Wei, Y.-C. Lo, and A. Hu, *Sci. Rep.* **9**, 10940 (2019).
35. T. Toyama, Y. Nozawa, W. Van Renterghem, Y. Matsukawa, M. Hatakeyama, Y. Nagai, A. Al Mazouzi, and S. Van Dyck, *J. Nucl. Mater.* **425**, 71 (2012).
36. M. Nastar and F. Soisson, *Radiation-Induced Segregation* (Elsevier Inc., 2012).
37. Y. Ma, B. Jiang, C. Li, Q. Wang, C. Dong, P. K. Liaw, F. Xu, and L. Sun, *Metals (Basel)*. **7**, (2017).
38. Y. Y. Zhao, H. W. Chen, Z. P. Lu, and T. G. Nieh, *Acta Mater.* **147**, 184 (2018).
39. D. Chen, F. He, B. Han, Q. Wu, Y. Tong, Y. Zhao, Z. Wang, J. Wang, and J. jung Kai, *Intermetallics* **110**, 106476 (2019).

SECTION

2. CONCLUSIONS AND FUTURE WORK

2.1. CONCLUSIONS

We have evaluated two different classes of radiation resistant materials: nanostructured steels and high entropy alloys. During manufacturing of nanostructured 304 steel, segregation and precipitation occurred similar to that observed in irradiated 304. This was understood as being a kinetically driven segregation and precipitation due to the flux of deformation induced defects towards grain boundaries [43]. It was shown that these features can be removed through annealing at 500°C.

After ion irradiation of nanostructured 304 at 500°C, it was observed that RIS was significantly reduced as a function of grain size. In some of the nanocrystalline grain boundaries, segregation behavior was similar to that of grain boundaries during annealing. This can be understood by the reduction of defects which accumulate within the material due to the annihilation of defects at grain boundaries. This reduces the vacancy flux towards grain boundaries which drives RIS. In the case of small grain boundaries, this allows for thermodynamically driven segregation to compete with and overcome the kinetically driven RIS.

Nanostructured 304 steel also showed enhanced phase stability during ion irradiation at 500°C. When compared to the coarse grained 304 steel, nanostructured 304 shows significantly reduced radiation induced ferrite transformation and precipitation. This enhanced austenite stability of nanostructured 304 is attributed to both a reduction in

irradiation induced strain which inhibits the deformation induced martensite transformation as well as a reduction in RIS allowing for Ni (an austenite stabilizer) to remain in the matrix.

Two Co-free HEA compositions were also ion irradiated at 500°C.

$\text{Fe}_{30}\text{Ni}_{30}\text{Mn}_{30}\text{Cr}_{10}$ has a single phase FCC microstructure and $(\text{Fe}_{30}\text{Ni}_{30}\text{Mn}_{30}\text{Cr}_{10})_{94}\text{Ti}_2\text{Al}_4$ has a primary FCC phase with ordered FCC $L1_2$ γ' precipitates. The $(\text{Fe}_{30}\text{Ni}_{30}\text{Mn}_{30}\text{Cr}_{10})_{94}\text{Ti}_2\text{Al}_4$ alloy developed much larger dislocation loops under irradiation than the $\text{Fe}_{30}\text{Ni}_{30}\text{Mn}_{30}\text{Cr}_{10}$ alloy. This was attributed to the addition of Ti which is presumed to have lowered the stacking fault energy and increased the stability of faulted Frank loops. The stability of γ' was also evaluated and it was shown that γ' is stable under irradiation, and irradiation does not cause the precipitation of new γ' particles.

In summary, both nanostructured 304 steel and two Co-free HEAs were evaluated for their radiation tolerance. Both showed good radiation resistance, and the development of both nanostructured steels and HEAs will likely lead to enhanced performance and increased lifetimes of nuclear reactor structural materials.

2.2. FUTURE WORK

While it has been shown that nanostructured steels exhibit good radiation resistance, there are still many aspects of these steels that need to be explored. This includes studying the thermal stability of these materials and how to stabilize the grain size under high temperatures and irradiation conditions. The mechanical properties of these materials also need to be evaluated including their possible resistance to stress

corrosion cracking. Nanostructured steels may also suffer from poor creep resistance due to grain boundary slipping, however the effects of RIS on the prevention of grain boundary slipping has still yet to be evaluated. This work is part of a larger project funded by the U.S. Department of Energy Nuclear Energy Enabling Technologies (NEET)-Nuclear Science User Facilities (NSUF) programs, and these aspects will be further explored within this project.

The work performed on HEAs was also insightful in that the γ' phase in FCC HEAs has shown to be stable under irradiation. The precipitates studied, however, did not have the desired size or number density to properly act as effective radiation induced defect sinks. Further work is now being carried out on how to optimize these microstructures through thermomechanical treatments.

BIBLIOGRAPHY

- [1] G.Z. Voyiadjis, Handbook of damage mechanics: Nano to macro scale for materials and structures, 2015.
- [2] G.S. Was, Fundamentals of radiation materials science: Metals and alloys, second edition, 2016. doi:10.1007/978-1-4939-3438-6.
- [3] S.J. Zinkle, G.S. Was, Materials challenges in nuclear energy, *Acta Mater.* 61 (2013) 735–758. doi:10.1016/j.actamat.2012.11.004.
- [4] F.A. Garner, Radiation damage in austenitic steels, Elsevier Inc., 2012. doi:10.1016/B978-0-08-056033-5.00065-3.
- [5] M. Nastar, F. Soisson, Radiation-Induced Segregation, Elsevier Inc., 2012. doi:10.1016/B978-0-08-056033-5.00035-5.
- [6] C.C. Goodwin, R.G. Faulkner, S.B. Fisher, The Modeling of Combined Radiation-Induced and Thermal Non-Equilibrium Segregation of Chromium in Neutron-Irradiated Austenitic Stainless Steels, in: *Eff. Radiat. Mater. 18th Int. Symp.*, 1999: pp. 634–645.
- [7] A.J. Ardell, P. Bellon, Radiation-induced solute segregation in metallic alloys, *Curr. Opin. Solid State Mater. Sci.* 20 (2016) 115–139. doi:10.1016/j.cossms.2015.11.001.
- [8] T. Toyama, Y. Nozawa, W. Van Renterghem, Y. Matsukawa, M. Hatakeyama, Y. Nagai, A. Al Mazouzi, S. Van Dyck, Grain boundary segregation in neutron-irradiated 304 stainless steel studied by atom probe tomography, *J. Nucl. Mater.* 425 (2012) 71–75. doi:10.1016/j.jnucmat.2011.11.072.
- [9] Z. Jiao, G.S. Was, Novel features of radiation-induced segregation and radiation-induced precipitation in austenitic stainless steels, *Acta Mater.* 59 (2011) 1220–1238. doi:10.1016/j.actamat.2010.10.055.
- [10] Z. Jiao, G.S. Was, Precipitate behavior in self-ion irradiated stainless steels at high doses, *J. Nucl. Mater.* 449 (2014) 200–206. doi:10.1016/j.jnucmat.2014.02.026.
- [11] L. Tan, J.T. Busby, Alloying effect of Ni and Cr on irradiated microstructural evolution of type 304 stainless steels, *J. Nucl. Mater.* 443 (2013) 351–358. doi:10.1016/j.jnucmat.2013.07.054.

- [12] Z. Jiao, J. Hesterberg, G.S. Was, Effect of post-irradiation annealing on the irradiated microstructure of neutron-irradiated 304L stainless steel, *J. Nucl. Mater.* 500 (2018) 220–234. doi:10.1016/j.jnucmat.2017.12.030.
- [13] P.J. Maziasz, Formation and Stability of Radiation-Induced Phases In Neutron-Irradiated Austenitic and Ferritic Steels, *J. Nucl. Mater.* 169 (1989) 95–115. doi:10.1016/0022-3115(89)90525-4.
- [14] K. Lindgren, M. Boåsen, K. Stiller, P. Efsing, M. Thuvander, Evolution of precipitation in reactor pressure vessel steel welds under neutron irradiation, *J. Nucl. Mater.* 488 (2017) 222–230. doi:10.1016/j.jnucmat.2017.03.019.
- [15] G.S. Was, P.L. Andresen, Stress corrosion cracking behavior of alloys in aggressive nuclear reactor core environments, *Corrosion.* 63 (2007) 19–45. doi:10.5006/1.3278331.
- [16] A. Aitkaliyeva, L. He, H. Wen, B. Miller, X.M. Bai, T. Allen, Irradiation effects in Generation IV nuclear reactor materials, in: *Struct. Mater. Gener. IV Nucl. React.*, Elsevier, 2017: pp. 253–283. doi:10.1016/B978-0-08-100906-2.00007-0.
- [17] S.J. Zinkle, *Advanced irradiation-resistant materials for Generation IV nuclear reactors*, Elsevier Ltd, 2016. doi:10.1016/B978-0-08-100906-2.00016-1.
- [18] C. Sun, M. Song, K.Y. Yu, Y. Chen, M. Kirk, M. Li, H. Wang, X. Zhang, In situ Evidence of defect cluster absorption by grain boundaries in Kr ion irradiated nanocrystalline ni, *Metall. Mater. Trans. A Phys. Metall. Mater. Sci.* 44 (2013) 1966–1974. doi:10.1007/s11661-013-1635-9.
- [19] A. Alsabbagh, A. Sarkar, B. Miller, J. Burns, L. Squires, D. Porter, J.I. Cole, K.L. Murty, Microstructure and mechanical behavior of neutron irradiated ultrafine grained ferritic steel, *Mater. Sci. Eng. A.* 615 (2014) 128–138. doi:10.1016/j.msea.2014.07.070.
- [20] X. Zhang, K. Hattar, Y. Chen, L. Shao, J. Li, C. Sun, K. Yu, N. Li, M.L. Taheri, H. Wang, J. Wang, M. Nastasi, Radiation damage in nanostructured materials, *Prog. Mater. Sci.* 96 (2018) 217–321. doi:10.1016/j.pmatsci.2018.03.002.
- [21] X. Mao, K.H. Oh, J. Jang, Evolution of ultrafine grained microstructure and nano-sized semi-coherent oxide particles in austenitic oxide dispersion strengthened steel, *Mater. Character.* 117 (2016) 91–98. doi:10.1016/j.matchar.2016.04.022.
- [22] M.W. Barsoum, The MN+1AXN phases: A new class of solids, *Prog. Solid State Chem.* 28 (2000) 201–281. doi:10.1016/S0079-6786(00)00006-6.

- [23] A. Etienne, B. Radiguet, N.J. Cunningham, G.R. Odette, R. Valiev, P. Pareige, Ultramicroscopy Comparison of radiation-induced segregation in ultrafine-grained and conventional 316 austenitic stainless steels, *Ultramicroscopy*. 111 (2011) 659–663. doi:10.1016/j.ultramic.2010.12.026.
- [24] P.B.R. Rajan, I. Monnet, E. Hug, a Etienne, N. Enikeev, C. Keller, X. Sauvage, R. Valiev, B. Radiguet, Irradiation resistance of a nanostructured 316 austenitic stainless steel, *IOP Conf. Ser. Mater. Sci. Eng.* 63 (2014) 012121. doi:10.1088/1757-899X/63/1/012121.
- [25] K. Jin, C. Lu, L.M. Wang, J. Qu, W.J. Weber, Y. Zhang, H. Bei, Effects of compositional complexity on the ion-irradiation induced swelling and hardening in Ni-containing equiatomic alloys, *Scr. Mater.* 119 (2016) 65–70. doi:10.1016/j.scriptamat.2016.03.030.
- [26] M.H. Tsai, J.W. Yeh, High-entropy alloys: A critical review, *Mater. Res. Lett.* 2 (2014) 107–123. doi:10.1080/21663831.2014.912690.
- [27] D.B. Miracle, O.N. Senkov, A critical review of high entropy alloys and related concepts, *Acta Mater.* 122 (2017) 448–511. doi:10.1016/j.actamat.2016.08.081.
- [28] Y. Zhang, T.T. Zuo, Z. Tang, M.C. Gao, K.A. Dahmen, P.K. Liaw, Z.P. Lu, Microstructures and properties of high-entropy alloys, *Prog. Mater. Sci.* 61 (2014) 1–93. doi:10.1016/j.pmatsci.2013.10.001.
- [29] Y. Shi, B. Yang, P. Liaw, Corrosion-Resistant High-Entropy Alloys: A Review, *Metals (Basel)*. 7 (2017) 43. doi:10.3390/met7020043.
- [30] M.R. He, S. Wang, K. Jin, H. Bei, K. Yasuda, S. Matsumura, K. Higashida, I.M. Robertson, Enhanced damage resistance and novel defect structure of CrFeCoNi under in situ electron irradiation, *Scr. Mater.* 125 (2016) 5–9. doi:10.1016/j.scriptamat.2016.07.023.
- [31] N.A.P.K. Kumar, C. Li, K.J. Leonard, H. Bei, S.J. Zinkle, Microstructural stability and mechanical behavior of FeNiMnCr high entropy alloy under ion irradiation, *Acta Mater.* 113 (2016) 230–244. doi:10.1016/j.actamat.2016.05.007.
- [32] W.Y. Chen, X. Liu, Y. Chen, J.W. Yeh, K.K. Tseng, K. Natesan, Irradiation effects in high entropy alloys and 316H stainless steel at 300 °C, *J. Nucl. Mater.* 510 (2018) 421–430. doi:10.1016/j.jnucmat.2018.08.031.
- [33] F. Granberg, K. Nordlund, M.W. Ullah, K. Jin, C. Lu, H. Bei, L.M. Wang, F. Djurabekova, W.J. Weber, Y. Zhang, Mechanism of Radiation Damage Reduction in Equiatomic Multicomponent Single Phase Alloys, *Phys. Rev. Lett.* 116 (2016) 1–8. doi:10.1103/PhysRevLett.116.135504.

- [34] H. Wen, T.D. Topping, D. Isheim, D.N. Seidman, E.J. Lavernia, Strengthening mechanisms in a high-strength bulk nanostructured Cu-Zn-Al alloy processed via cryomilling and spark plasma sintering, *Acta Mater.* 61 (2013) 2769–2782. doi:10.1016/j.actamat.2012.09.036.
- [35] P.F. Yu, H. Cheng, L.J. Zhang, H. Zhang, Q. Jing, M.Z. Ma, P.K. Liaw, G. Li, R.P. Liu, Effects of high pressure torsion on microstructures and properties of an Al_{0.1}CoCrFeNi high-entropy alloy, *Mater. Sci. Eng. A.* 655 (2016) 283–291. doi:10.1016/j.msea.2015.12.085.
- [36] R. Orrù, R. Licheri, A.M. Locci, A. Cincotti, G. Cao, Consolidation/synthesis of materials by electric current activated/assisted sintering, *Mater. Sci. Eng. R Reports.* 63 (2009) 127–287. doi:10.1016/j.mser.2008.09.003.
- [37] M. Wang, N.Q. Vo, M. Campion, T.D. Nguyen, D. Setman, S. Dillon, P. Bellon, R.S. Averback, Forced atomic mixing during severe plastic deformation: Chemical interactions and kinetically driven segregation, *Acta Mater.* 66 (2014) 1–11. doi:10.1016/j.actamat.2013.11.066.
- [38] J. Yin, J. Lu, H. Ma, P. Zhang, Nanostructural formation of fine grained aluminum alloy by severe plastic deformation at cryogenic temperature, *J. Mater. Sci.* 39 (2004) 2851–2854. doi:10.1023/B:JMSC.0000021463.83899.b3.
- [39] R.Z. Valiev, R. Islamgaliev, I.V. Alexandrov, Bulk nanostructured materials from severe plastic deformation, *Prog. Mater. Sci.* 45 (2000) 103–189. doi:10.1016/S0079-6425(99)00007-9.
- [40] R.Z. Valiev, I.V. Alexandrov, Nanostructured materials from severe plastic deformation, *Nanostructured Mater.* 12 (2002) 35–40. doi:10.1016/s0965-9773(99)00061-6.
- [41] R.Z. Valiev, T.G. Langdon, Principles of equal-channel angular pressing as a processing tool for grain refinement, *Prog. Mater. Sci.* 51 (2006) 881–981. doi:10.1016/j.pmatsci.2006.02.003.
- [42] G.J. Raab, R.Z. Valiev, T.C. Lowe, Y.T. Zhu, Continuous processing of ultrafine grained Al by ECAP-Conform, *Mater. Sci. Eng. A.* 382 (2004) 30–34. doi:10.1016/j.msea.2004.04.021.
- [43] A. Hoffman, H. Wen, R. Islamgaliev, R. Valiev, High-pressure torsion assisted segregation and precipitation in a Fe-18Cr-8Ni austenitic stainless steel, *Mater. Lett.* 243 (2019) 116–119. doi:10.1016/j.matlet.2019.02.030.

VITA

Andrew Kalevi Hoffman was born in Riyadh, Saudi Arabia in 1989, but grew up in Charlottesville, VA. He attended undergraduate at Brigham Young University (BYU) in Provo, UT from 2005-2012 where he earned his B.S. in physics in August 2012.

Andrew took a break during his undergraduate studies to perform volunteer missionary work in northern Brazil from 2008-2010. His research experience started at BYU where he worked as an undergraduate research assistant on the development of neutron detectors to replace He-3 detectors for homeland security applications. He started graduate school at Idaho State University in Pocatello, ID in August 2012, and earned his M.S. in physics in May 2016. His physics research included the study of plasma properties through imaging of exploding wires and the development of an exotic quasi mono-energetic x-ray source using laser Compton scattering. Though he started his PhD in Nuclear Science & Engineering in August 2014 at Idaho State University, Andrew transferred to Missouri University of Science and Technology in August 2017. His research expertise focuses on advanced microstructural characterization of materials. He received his PhD in Nuclear Engineering from Missouri University of Science and Technology in December 2019 under the direction of Dr. Haiming Wen.